

University of
Strathclyde
Engineering

HTS Armature Study for Electrified Aviation Propulsion Motors

Zhishu Qiu

Department of Electronic and Electrical Engineering

University of Strathclyde

A thesis submitted for the degree of

Doctor of Philosophy

December, 2024

Supervisor: Prof Min Zhang

Declaration

This thesis is the result of the author's original research. It has been composed by the author and has not been previously submitted for any examination which has led to the award of a degree.

The copyright of this thesis belongs to the author under the terms of the United Kingdom Copyright Acts as qualified by University of Strathclyde Regulation 3.50. Due acknowledgement must always be made of the use of any material contained in, or derived from, this thesis.

Signed:

Date: Monday, Dec 2nd, 2024

Acknowledgement

First and foremost, I would like to express my sincere gratitude to my supervisors, Professor Min Zhang and Professor Weijia Yuan, for their valuable guidance, endless support, and insightful feedback throughout my research. The completion of this research would not be possible without their expertise and professional technique guidance. I am deeply grateful to them for encouraging and supporting me to participate in various academic activities, giving me the opportunity to connect with peers from all over the world. These invaluable experiences have broadened my perspectives, allowing me to reflect on my own research work quickly and effectively, and have helped me maintain a lasting passion for scientific research. I really appreciate the opportunity they have provided me to conduct research at the University of Strathclyde.

I would also like to thank my colleagues and friends in the Applied Superconductivity Group at the University of Strathclyde for not only academic collaboration but also friendship and support. Special thanks are due to Dr Aleksandr Shchukin, Dr Hengpei Liao, Dr Ercan Ertekin, Dr Yudi Xiao, Mr Oriol Fernández Serracanta, and Mr Muhammad Bin Younas for their inspired discussions, and to all the group members for mental support and encouragement.

I would also like to extend my thanks to my peers Dr Rémi Dorget, Mr Yunfei Gao, Mr Calvin C. T. Chow, and Mr Casper Clop who provided me with valuable positive feedback and kindness.

Lastly, I would like to appreciate my family and my friends, especially my parents. With their love, companionship, and mental and financial support, especially during the tough COVID-19 period, I will successfully complete this precious journey.

Thank you to all who contributed to this journey. This thesis is the result of your support as well as my own hard work.

Publications

Paper accepted:

1. **Z. Qiu**, A. Shchukin, M. B. Younas, H. Liao, W. Yuan and M. Zhang, "The Radial Flux HTS Synchronous Motor Stator Windings Comparison for Electrified Aircraft Applications," in *IEEE Transactions on Applied Superconductivity*, doi: 10.1109/TASC.2025.3545412.

Paper under review:

1. A. Shchukin, **Z. Qiu**, M. Younas, E. Ertekin, H. Liao, W. Yuan, A. Colle, R. Abdouh, L. Ybanez, F. Eastham, and M. Zhang, "Developing a 100 kW fully superconducting aviation motor: the superconducting armature," *Superconductor Science and Technology*

Abstract

The continued expansion of global air traffic has highlighted the urgent need to reduce the global warming impact of the aviation industry. Traditional aircraft systems rely heavily on fossil fuels and contribute significantly to CO₂ and NO_x emissions. To accomplish the goal of zero-emissions aviation, the proposal of More Electric Aircraft (MEA) or All Electric Aircraft (AEA) propulsion systems stands as a potential solution. Since conventional electric motors are too heavy for aviation, efficient multi-megawatt motors with high power density are needed, and cryogenic superconducting motors are a promising solution thanks to their high current capacity. However, high-temperature superconducting (HTS) coils cannot be widely used as motor armature windings until the cryogenic AC loss is reduced to an acceptable limit regarding motor power density and efficiency requirements.

This thesis presents original research of the design and optimization of HTS armature coils focusing on the AC loss evaluation and reduction. With the help of experimental measurements and numerical simulations analysis, the standard 2G (second generation) HTS insulated coils are found to be competitive to copper/aluminium Litz wires for a megawatt (MW) level cryogenic motor working at a temperature around 40 K. In addition, the AC loss can be reduced by narrowing the tape width or adding a thin layer of stator back iron. This thesis also introduces a novel multi-stack coil structure to improve the HTS stator electrical loading while maintaining the mechanical and thermal stability. The transport current loss of this novel coil is investigated, and the AC loss can be minimized by balancing the inductance between the parallel stacks.

Table of Contents

Declaration	ii
Acknowledgement.....	iii
Publications	iv
Abstract	v
Table of Contents	vi
List of Figures	x
List of Tables	xv
Abbreviations	xvi
Chapter 1 Introduction	1
1.1 Background: Why develop electric propulsion systems?.....	1
1.2 Overview of electric propulsion.....	2
1.3 Superconducting motor for electric propulsion.....	5
1.3.1 HTS electric propulsion	6
1.3.2 Existing HTS motor topologies for electric propulsion	25
1.3.3 HTS motor thermal management	7
1.3.4 HTS motor challenges	8
1.4 Aim of the study	9
1.5 Thesis structure.....	10
Chapter 2 Superconductivity background.....	12
2.1 Introduction to superconductivity	12
2.1.1 Low temperature and high temperature superconductors	13
2.1.2 Type I superconductors and type II superconductors.....	15
2.1.3 Structure of 2G HTS tape using YBCO HTS material	18
2.2 Critical state model of type II superconductors	19
2.2.1 Flux pinning	19

2.2.2 Flux creep, flux flow and E-J power law	20
2.2.3 Bean's critical state model.....	21
2.2.4 Kim-Anderson Model	22
2.3 AC loss in 2G HTS tape	22
2.3.1 AC loss mechanisms.....	22
2.3.2 Hysteresis loss	24
2.3.3 Other types of AC loss	25
2.4 Technical importance of AC loss to HTS propulsion motors.....	29
2.5 Conclusion.....	30
Chapter 3 AC loss evaluation of HTS	32
3.1 Introduction	32
3.2 Analytical analysis of AC loss calculations.....	32
3.3 Numerical modelling methodology.....	34
3.3.1 General numerical modelling for HTS materials	34
3.3.2 Improved numerical modelling adapted to large scale HTS	37
3.3.3 Implementation of critical current dependency in numerical modelling	42
3.4 Experiment methodology for modelling validation	44
3.4.1 Electrical methodology	44
3.4.2 Magnetic methodology.....	46
3.4.3 Calorimetric methodology.....	47
3.5 Numerical model validations by experiments.....	52
3.5.1 Test coil preparation and critical current determination.....	52
3.5.2 AC loss measurement	53
3.5.3 Coil model methodologies	54
3.5.4 Coil self-field critical current calibration	58
3.5.5 AC loss validation	59

3.6 Conclusion.....	61
Chapter 4 The radial flux HTS synchronous motor topology comparison for electrified aircraft applications.....	63
4.1 Introduction	63
4.2 Radial flux motor in electrified aviation	64
4.2.1 Two power level motor benchmarks	64
4.3 Motor topology determinations	65
4.3.1 Slotless stator design.....	65
4.3.2 Stator winding comparison.....	66
4.3.3 Winding performance comparison	67
4.4 Conclusion.....	70
Chapter 5 Impact to AC loss of standard HTS coil.....	72
5.1 Introduction	72
5.2 Applied current impact	73
5.3 Coil working temperature impact.....	73
5.4 Applied current harmonics impacts.....	75
5.5 Conclusion.....	81
Chapter 6 HTS armature AC loss analysis under radial flux HTS motor environment.....	83
6.1 Introduction	83
6.2 Radial flux partially HTS motor.....	84
6.2.1 Design methodology	85
6.2.2 Structure of the machine	86
6.2.3 Modelling methodology	88
6.3 Radial flux fully HTS motor	93
6.3.1 Design methodology	94

6.3.2 HTS rotor design and optimization	95
6.3.3 HTS stator design and optimization	99
6.3.4 Shielding considerations: back iron impact	101
6.4 Conclusion.....	103
Chapter 7 Transport current AC loss analysis of multi-stack HTS coil	106
7.1 Introduction	106
7.2 Novelty of the stack coil design	107
7.3 Stack coil geometry	108
7.4 Coil measurement setups.....	109
7.4.1 Coil critical current, I_c determination	109
7.4.2 Current distribution measurement setups	110
7.4.3 Inductance difference setups	111
7.4.4 AC loss measurement setups	113
7.5 Measurement results and analysis	114
7.5.1 Proof of coupling.....	114
7.5.2 Coil AC loss Analysis.....	117
7.6 Coil AC loss simulations	125
7.6.1 Simulation methodologies.....	125
7.6.2 Coil AC loss results	126
7.6.3 Coil magnetic energy analysis.....	127
7.7 Conclusion.....	129
Chapter 8 Conclusion	132
8.1 Thesis summary.....	132
8.2 Future work	133
Reference.....	135

List of Figures

Figure 1.1 a) Conventional turbofan propulsion; and b) electric propulsion [17]	3
Figure 1.2 Electric propulsion architectures [15].....	4
Figure 2.1 Meissner effect of superconductors [46].....	12
Figure 2.2 Schematic diagram of the critical surface of a superconductor (critical temperature T_C , critical current density J_C , and upper critical magnetic field H_{C2}) [47]	13
Figure 2.3 Discovery of major superconductors (DoITPoMS, University of Cambridge).....	15
Figure 2.4 The dependence of H_c on temperature for type I superconductors.....	16
Figure 2.5 The dependence of H_c on temperature for type I superconductors.....	17
Figure 2.6 Part of the lattice structure of YBCO (CC BY-SA 3.0)	18
Figure 2.7 Architecture of a standard SuperPower 2G HTS tape using REBCO HTS material	19
Figure 2.8 Diagram of a vortex [67]	20
Figure 2.9 An example of flux creep and E-J power law to determine critical current density	21
Figure 2.10 a) Slab of type II superconductor under an external field[70]; b) critical current density J_{cx} corresponding to H_{sx}	21
Figure 2.11 Cross-section of a superconductor under a time-varying external magnetic field	23
Figure 2.12 Schematic of the different loss contributions in technical HTSs 1) Hysteresis losses in the superconductor; 2) eddy current losses in the normal metal stabilizer; 3) coupling losses between filaments (e.g., through conducting paths due to imperfections of the striation process); and 4) ferromagnetic losses in the substrate. [69]	24
Figure 1.3 The structure of PSCM with cryostat [20].....	26
Figure 1.4 Design options for superconducting stator and rotor in radial motors. Stator types: a) b) Concentrated and distributed windings with iron teeth; c) d) Concentrated and distributed windings with no iron teeth. Rotor types: e) Salient pole version; and f) surface-mounted superconducting magnets or coils. [85].....	28
Figure 1.5 Schematic diagram of thin (left) and thick (right) flux diverter position around the stator superconducting coils [28]	29
Figure 3.1 2D HTS machine modelling geometry example using T-A formulation [118]	38
Figure 3.2 Coil structure in 2D view [74] a) uncoupled insulated tape case; b) partially coupled case; and c) fully coupled case	39

Figure 3.3 Coil (stack) structure in 3D view a) insulated tape case; b) partially coupled case; and c) fully coupled case [119]	39
Figure 3.4 Racetrack coil 4 turns structure a) all connected in series; and b) connected in parallel as 2 branches [120].....	41
Figure 3.5 T-A coupled electrical circuit [120]	41
Figure 3.6 HTS tape critical current dependence on external magnetic field	42
Figure 3.7 An example of the critical current characteristic of SuperOx tape a) temperature dependency; and b) angle dependency at 77 K.....	42
Figure 3.8 An example of the critical current field dependency of SuperOx tape a) field perpendicular to tape wider surface; and b) field parallel to tape wider surface	44
Figure 3.9 An example of the 3D critical current characteristic of SuperOx tape at 77 K	44
Figure 3.10 AC loss measurement setup for the electrical method.....	46
Figure 3.11 Measurement system using the magnetic method a) Layout of different coils; and b) setup equivalent circuit [124].....	47
Figure 3.12 AC loss measurement setup for the calorimetric method [73].....	49
Figure 3.13 Calorimetric boil-off measurement setups in the laboratory	50
Figure 3.14 The tested insulated double pancake coil sample and its measurement setups	53
Figure 3.15 Coil self-field critical current measurement	53
Figure 3.16 Transport current AC loss measurement under different working frequencies	54
Figure 3.17 Coil model geometry in COMSOL Multiphysics.....	55
Figure 3.18 Explanation of T-A formulation.....	57
Figure 3.19 The 3D plot of the $J_{cB}(\theta, B)$ mapping data for this specific insulated coil	58
Figure 3.20 The tested insulated coil self-field critical current calibration in COMSOL Multiphysics	59
Figure 3.21 Transport current AC loss H-formulation simulation validation	60
Figure 3.22 Transport current AC loss T-A simulation validation	60
Figure 4.1 AC loss comparison for 450 kW benchmark at 77 K.....	68
Figure 4.2 Power density comparison for 450 kW benchmark at 77 K.....	69
Figure 4.3 AC loss comparison for 1 MW benchmark at 40 K.....	69
Figure 4.4 Power density comparison for 1 MW benchmark at 40 K.....	70
Figure 5.1 Transport current loss of the coil with different working frequencies at 77 K.....	73
Figure 5.2 Transport current loss of the coil at 40 K and 65 K, respectively.....	74

Figure 5.3 Transport current loss comparison at different working temperatures	74
Figure 5.4 Transport current loss considering current harmonics at 100 Hz: a) 5 th harmonic components; b) 7 th harmonic components; and c) 5 th and 7 th harmonic components	77
Figure 5.5 Transport current loss considering current harmonic components a) at 40 K; and b) at 65 K.....	78
Figure 5.6 Transport current loss with 5 th current harmonic frequency dependency at 40 K a) harmonic components in portion of 5%, 10% and 15%, respectively; and b) 5% of harmonic component	79
Figure 5.7 Transport current loss with 5 th current harmonic frequency dependency at 65 K a) harmonic components in portion of 5%, 10% and 15%, respectively; and b) 5% of harmonic component	80
Figure 6.1 An example structure of radial flux partially HTS motor: PM rotor and HTS Stator	85
Figure 6.2 Machine equivalent circuit diagram	86
Figure 6.3 The analytical modelling process flow chart	86
Figure 6.4 A simplified one pole structure of a slotless partially HTS motor with permanent magnet rotor	87
Figure 6.5 Inner rotor PM machine cross section scheme [7].....	88
Figure 6.6 PM rotor no-load magnetic flux density distribution.....	90
Figure 6.7 Analytical modelling validation for rotor radial flux density	90
Figure 6.8 Stator winding distribution	91
Figure 6.9 One-twelfth machine model built in COMSOL	92
Figure 6.10 HTS armature performance results of a) ac loss; and b) equivalent ac resistance	93
Figure 6.11 Diagram of machine cross section [151]	95
Figure 6.12 Rotor coil distribution along machine electrical angles.....	96
Figure 6.13 Analytical method validation for rotor field flux density	97
Figure 6.14 Field winding current penetration.....	97
Figure 6.15 Current wave as a result of superposition of multi current leads.....	98
Figure 6.16 Two current leads applied to rotor HTS coil with one third of inner tapes having higher current	98
Figure 6.17 Radial flux density comparison between one current lead and two current leads	99

Figure 6.18 The current penetration for different tape widths a) 4 mm; b) 2 mm; c) 1 mm; and d) 0.5 mm	100
Figure 6.19 The machine structure with 4 mm back iron	102
Figure 6.20 Radial flux density with and without shielding	102
Figure 6.21 Shielding impact on stator winding current penetration a) without shielding; and b) with shielding.....	103
Figure 7.1 The stack coil structure	108
Figure 7.2 Coil structure scheme, with the HTS layer in grey, the metallic soldering in brown, and the insulation in green. The yellow solid box and blue dashed box mark the two stack turn.	109
Figure 7.3 Real stack coil for testing.....	110
Figure 7.4 Coil critical current, I_c measurement conducted from two stacks, respectively ...	110
Figure 7.5 Current transducers for coil current distribution measurement	111
Figure 7.6 The possible positions of current transducers shown in coloured boxes	111
Figure 7.7 Coil with bigger inductance differences between stacks	112
Figure 7.8 AC loss measurement setup	113
Figure 7.9 Coil coupling investigation tape current distribution circuits a) reference scenario 0: all tapes connected to the circuit; b) scenario 1: one stack connected to the circuit; c) scenario 2: one tape in each stack connected to the circuit 2; and d) scenario 3: one tape in each stack connected to terminal 1 and all stacks connected to terminal 2	115
Figure 7.10 Coil coupling investigation tape current distribution results at 50 Hz with applied current of 30 A_{rms} a) reference scenario 0; b) scenario 1; c) scenario 2; and d) scenario 3 ...	116
Figure 7.11 Transport current AC loss measurements comparison with compensation coil connected to inner and outer stack respectively at a) 50 Hz; and b) 100 Hz	118
Figure 7.12 Current distribution of two stacks at 50 Hz, 30 A_{rms} a) inner stack compensation case; and b) outer stack compensation case	119
Figure 7.13 Current amplitude in each stack comparison with compensation coil connected to inner and outer stack respectively a) at 50 Hz; and b) 100 Hz.....	120
Figure 7.14 Current phase shift measurement comparison between two stacks at 50 Hz and 100 Hz with compensation coil connected to inner and outer stack, respectively.....	121
Figure 7.15 Transport current AC loss comparison between original coil and coil with bigger ΔL at a) 50 Hz; and b) 100 Hz.....	122

Figure 7.16 Current distribution of two stacks at 100 Hz, 30 A_{rms} a) original coil case; and b) bigger ΔL coil case 124

Figure 7.17 Normalized stack current with respect to half I_{app} (A_{rms}) a) original coil; and b) bigger ΔL case considering out-of-phase current impact..... 125

Figure 7.18 Double stack coil geometry in 2d axis-symmetrical model..... 126

Figure 7.19 AC loss comparison between simulation and electric measurements of bigger ΔL case 126

Figure 7.20 Hysteresis I-H loop of a) overall big and small ΔL cases; b) two stacks of small ΔL case; and c) two stacks of big ΔL case 128

Figure 7.21 Transient magnetic energy comparison between small and big ΔL cases 129

List of Tables

Table 1.1 Present projects of HTS motor design for electric propulsion systems 7

Table 3.1 Different formulae used to solve Maxwell’s equations and numerical models for HTS electromagnetic behaviour simulations [99]..... 35

Table 3.2 Lift factor parameters for critical current calculation at different working temperatures with respect to 77 K..... 43

Table 3.3 Comparison between two AC loss measurement methods [129] 52

Table 3.4 Insulated double pancake coil parameters..... 52

Table 4.1 Motor benchmark parameters..... 65

Table 4.2 Coefficients for the resistivity of copper and aluminium at cryogenic temperature 66

Table 6.1 Design dimension parameters of the slotless radial flux PM-HTS motor..... 87

Table 6.2 Design electrical parameters of the slotless PM-HTS motor 88

Table 6.3 Inductance modelling case study results 91

Table 6.4 Design parameters of the slotless radial flux fully HTS motor 95

Table 6.5 Stator design parameters..... 99

Table 6.6 AC losses for different tape widths 100

Table 6.7 AC loss results comparison for different tape widths considering I_c degradation.. 101

Table 6.8 2.3 MW motor stator optimization results considering AC loss performance 104

Table 7.1 Stack coil parameters..... 109

Table 7.2 Two cases of inductance difference between stacks..... 112

Table 7.3 Average stack current phase shift 123

Abbreviations

Abbreviation	Definition
1G	First Generation
2G	Second Generation
AC	alternating current
AEA	All Electric Aircraft
BSCCO	Bismuth Strontium Calcium Copper Oxide
CL	current lead
DAQ	data acquisition system
DC	direct current
DOF	degree of freedom
E0	characteristic electric field
EMF	electromotive force
FEM	Finite Element Method
H _c	critical magnetic field
HTS	high-temperature superconducting
HTSM	high temperature synchronous machine
J _c	critical current density
kW	kilowatt
LH ₂	liquid hydrogen
LN ₂	liquid nitrogen
LTS	low-temperature superconducting
MEA	More Electric Aircraft
MRI	Magnetic Resonance Imaging
MW	megawatt
PM	permanent magnet
PMSM	permanent magnet synchronous machine
PTW	power-to-weight ratio
REBCO	Rare-Earth Barium Copper Oxide
T _c	critical temperature
YBCO	Yttrium Barium Copper Oxide

Chapter 1 Introduction

1.1 Background: Why develop electric propulsion systems?

Commercial aerospace plays an important role in the evolution and development of society. The global air passenger traffic has grown at an average annual rate of 9% since 1960, and it is expected to grow continuously at a rate of 5% to 7% in the future[1]. As the aerospace industry is booming, the aviation sector is responsible for approximately 2.5% of global CO₂ emissions. However, in addition to the direct greenhouse gas emissions, non-CO₂ effects have an effect on the overall aircraft radiative forcing. The main non-CO₂ components are NO_x emissions[2-5]. Regarding[3, 6], non-CO₂ forcings account for two thirds of the warming impact, and resulting in around 4% of global warming to date. Among this warming impact, around 90% of emissions are from engines, and these figures are expected to rise as air travel increases[3, 7, 8]. This underscores the urgent need for more sustainable aviation technologies. To improve the performance of future aircraft in terms of safety, air pollution, noise and climate change, governments have set different long-term goals for emissions regulations: the ACARE (Advisory Council for Aeronautic Research in Europe) has agreed on environmental regulations aiming for emissions (CO₂, 75%; NO_x, 90%) and noise (65%) reduction with reference to 2000 levels (Flight path 2050); the ICAO (International Civil Aviation Organization) is targeting a neutral growth of emissions since 2020; and the ATAG (Air Transport Action Group) is aiming for a 50% reduction in CO₂ emissions between 2005 and 2050.

Regarding increasing attention to the impact of aircraft emissions, together with the rising price of fuel unlikely to remain stable in the coming years[9], airlines are under pressure from governments who are concerned to develop more efficient and cleaner aircraft systems. Traditional aircraft systems, with limited power generation, rely heavily on fossil fuels and contribute significantly to the emissions[1, 6, 10]. New disruptive technologies, therefore, need to be proposed to achieve this ambitious target.

Before electrical propulsion was proposed, research on alternative fuels has been conducted for decades, but none of them have achieved the energy density requirement for aviation since minimizing the gross weight of an aircraft is critical for efficient operation. Some synthetic fuels have been developed for aircraft and are proposed as an alternative. However, these

alternatives to fossil fuels are more practical with other forms of transportation since they usually consume more energy than regular jet fuel in the production process. Therefore, the aviation industry must focus on efficiency improvement[11].

Compared to traditional aviation systems which require appropriate redundancy for complicated hydraulic and pneumatic systems, the proposed More Electric Aircraft (MEA)/ All Electric Aircraft (AEA) concept involves transitioning to electrical systems to improve the system reliability and efficiency[12, 13]. This evolution from secondary electrical power systems towards a primary electrical power system, results in a huge change in the electrical power required for aircraft[11]: high power machines with high power density in both volume and weight scales.

1.2 Overview of electric propulsion

More-electric aircraft (MEA) is one potential solution available for the development of more efficient and environmentally friendly aircraft. Thanks to the development of power electronics, electric machines and advanced control technologies, in MEA, many functions previously driven by hydraulic, pneumatic and mechanical power are undergoing a replacement by electrical subsystems[14-16]. Unlike conventional aircraft, the MEA has the advantage of lower cost due to simpler systems with fewer components, and moreover, it also reduces the overall cost of operation and ownership as it consumes less fuel thus increasing the overall aircraft performance and energy usage.

Unlike traditional propulsion systems, electric propulsion systems avoid the coupling issue between the turbofan and the low pressure (LP) shaft. As illustrated in Figure 1.1b, each generator is connected to a shaft mechanically, while an electrical connection between the propulsor (the fan) and the generators is achieved through an “electrical gearbox”[17]. Hence, the generator can tolerate much higher speeds than the fan, and the engine LP shaft can run much faster. As a result, in fewer stages, the weight of the machine could be reduced and machine efficiency will be increased[17].

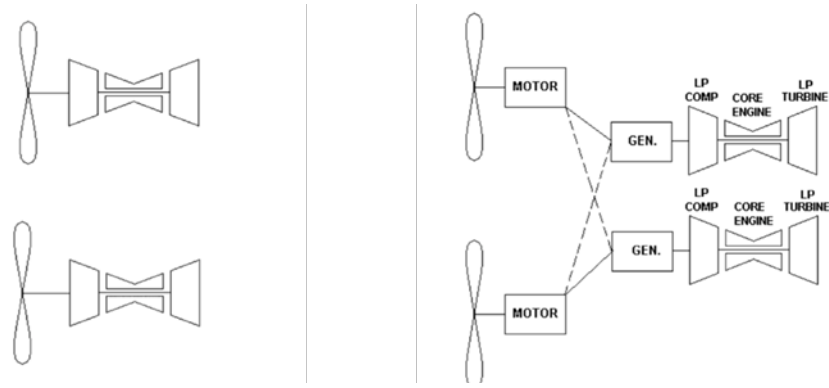


Figure 1.1 a) Conventional turbopropulsion; and b) electric propulsion [17]

In a word, MEA could provide aviation performance benefits by achieving the aviation power density requirement as well as environmental benefits of offsetting CO₂ emissions by the source of electricity used to charge their batteries. However, these could only be accomplished if new technologies attain the specific power, weight, and reliability required for a successful commercial fleet[15].

To make a roadmap for electric propulsion systems, we need to set targets of the weights of each component in the system to enable technology development. In the electrical machines industry, the design would need to meet power density targets [18]:

- Short term (10 years): 10 kW/kg
- Mid Term (15 years): 20 kW/kg
- Long Term (25 years): 50 kW/kg

It should be noted that these targets must include all the relevant equipment including any cooling or special environmental conditions. Therefore, superconducting motors must include a portion of the required cryogenic systems in power density calculations in order to compare technologies fairly. Both permanent magnet machines and superconducting machines are candidates for this application. Though the results from [19] and [20] show that high-temperature superconductor (HTS) based superconducting machines could achieve 2–3 times the power density reached by permanent magnet synchronous machines (PMSMs) under similar requirements and constraints, PMSMs still have their advantage of easy manufacturing. In summary, short- and medium-term goals for motors can be achieved with traditional machine design techniques, while long-term goals will depend on new technologies.

Electric propulsion architecture could be divided into three types and six different electric propulsion architectures regarding different electric power technologies (batteries, electric motors, generators, etc.). As shown in Figure 1.2 they are one all-electric, three hybrid electric, and two turboelectric architectures[15, 18]:

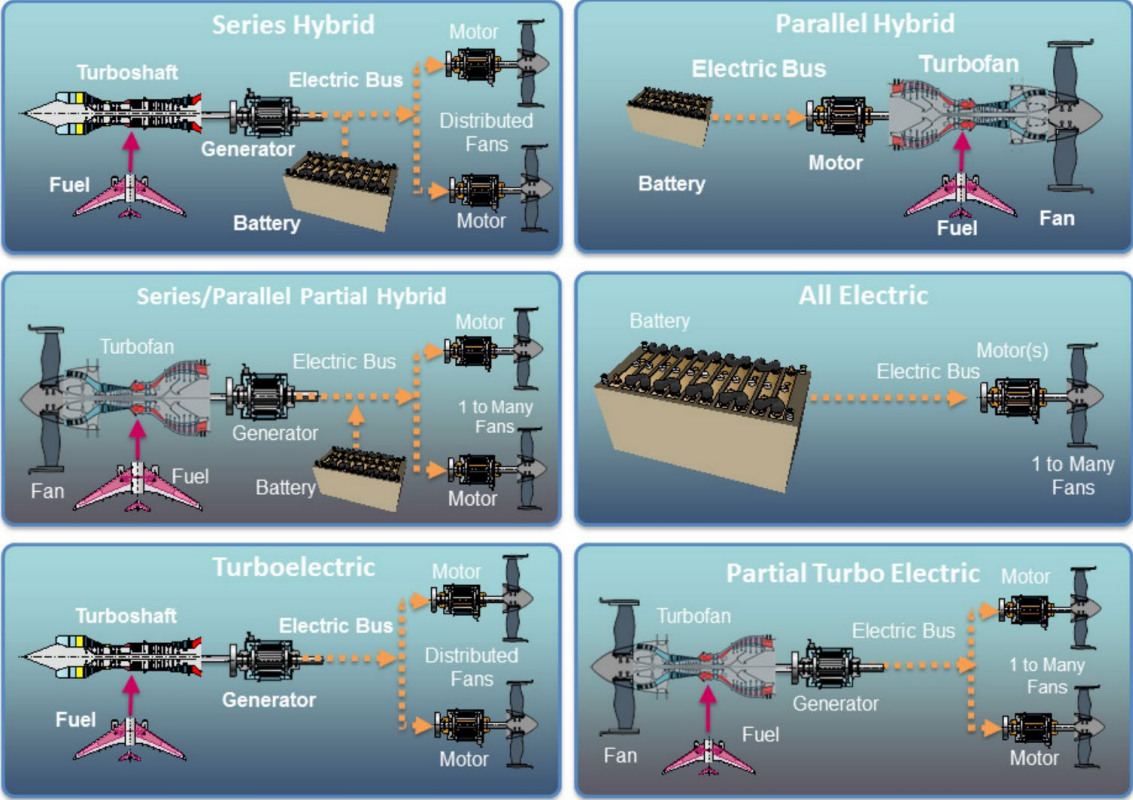


Figure 1.2 Electric propulsion architectures [15]

The CO₂ reduction levels of different architectures depend on the configuration, component performance, and mission. These different architectures are summarized as follows.

Batteries are the only power source for all electric systems while both fuel and batteries are the power source for hybrid electric systems. The turboelectric architecture does not rely on batteries for propulsion energy during any phase of flight. Regarding the analysis in[15], turboelectric propulsion research is identified as one of the high-priority approaches for commercial propulsion and energy system technologies during the next 10 to 30 years to reduce CO₂ emissions. The reason is that the electrical components for a partial turboelectric system can be developed with smaller advances beyond the state of the art than are required for other electric systems; while on the other hand, current battery technologies are not sufficient to the requirement of the power capacity and specific power for commercial aircraft, and it is

predicted unlikely to be mature enough to satisfy the requirements in 30 years. It is also mentioned that the same situation applies to technologies related to superconducting machines, and fuel cells, as well as cryogenic fuels. All-electric battery-powered airplane configurations will be limited to small aircraft in the next 10–30 years[21].

According to research in[11], to achieve midsize electrical commercial air transport, for instance, multi MW electrical machines with power density no less than 20 kW/kg and very high efficiency no less than 96% are required. Traditional electric motor design is no longer sufficient to meet these targets. Permanent magnet synchronous motors (PMSMs) [22-24]are proposed to be a promising candidate due to their advantages of high power density, high output torque, and simple operation, while their manufacturing technologies are mature. Compared to PMSMs, superconducting machines (i.e. machines using superconducting materials) [25-27]are more attractive to achieve the requirements because of their high power density and high efficiency[27]. The main reason is that superconducting materials can help dramatically increase electric loading and magnetic loading and therefore significantly reduce machine weight [7] thanks to their ability to carry very high current density with small resistance.

1.3 Superconducting motor for electric propulsion

The aerospace industry is undergoing a transfer towards electric propulsion systems, as it seeks to reduce its environmental impact and increase efficiency. Traditional aircraft systems relying heavily on fossil fuels have a significant impact on global warming. The transfer towards MEA and AEA addresses these challenges by moving from traditional mechanical and hydraulic systems to primarily electric systems, ensuring greater reliability and efficiency. This change requires the development of high-power density motors to meet the strict power and weight requirements of efficient commercial aviation. This level of performance can only be achieved by using technologies that provide high power density and efficiency, such as superconducting materials.

The high current carrying capacity and minimal electrical resistance of HTS materials can significantly reduce motor weight, enabling more efficient and powerful aircraft propulsion systems. Therefore, HTS motors are promising candidates for electric propulsion due to their excellent power density and efficiency. Ideally, HTS motors outperform traditional permanent magnet motors with power densities of 30 kW/kg and efficiencies of up to 99%[25, 28]. These

properties make HTS motors particularly suited to the demanding requirements of the aerospace industry, where weight and efficiency are of vital importance.

1.3.1 HTS electric propulsion

A major challenge of scaling up electric propulsion to larger aircraft is the power-to-weight ratio (PTW). Present electrical systems could not satisfy the necessary power requirements without adding excess weight to the aircraft. Hence with their higher current capacity, HTS technologies are proposed as a promising solution to this technical challenge.

Regarding superconductors and their applications in motors, superconducting rotor part magnet coils could provide up to several Tesla and superconducting stator part armatures could achieve electrical loading up to 200 kA/m[29, 30]. High Temperature Superconducting Motors (HTSMs), capable of achieving power densities up to 30 kW/kg and efficiencies near 99%[25, 28], offer significant advantages over traditional motors, which typically achieve only about 5 kW/kg and 90–95% efficiency[31, 32]. This improvement is crucial for aviation, where even minor reductions in weight and efficiency can lead to significant operational savings. Although still in the experimental phase, superconducting motors are being actively developed, with prototypes showing considerable promise. Projects such as NASA's high-efficiency motor research aim to implement motors with 1.4 MW output power and 99% efficiency by 2040, demonstrating the potential of superconducting technologies to meet future aviation demands. By 2023, the project developed by Airbus UpNext, named Advanced Superconducting and Cryogenic Experimental powertrain Demonstrator (ASCEND) successfully explored the impact of cryogenic superconductivity on the electrical infrastructure and powered-on a 500 kW powertrain of the next generation of low-carbon aircraft.

Countries all over the world are investing a lot in the development of HTS propulsion systems for aviation applications. While each country has its own focus and level of development, the global trend is towards using HTS technology to meet the increasing power demands of future propulsion systems. Some present projects of HTS propulsion system design are summarized in the table below. It is noticed that the magnetic loading is set on average 4–5 T and the working temperature at 30–40 K is desired to achieve MW level motor requirements of electric propulsion systems.

Table 1.1 Present projects of HTS motor design for electric propulsion systems

Country	Projects	Propulsion power (MW)	Motor information	Efficiency	Operating temperature (K)	Power density (kW.kg)
US	NASA (EAP) [33]; ARPA-E's program [34]	1–3	NASA (EAP): HTS rotor; slotless stator 12 poles, 9 phases ARPA-E's program: HTS rotor, conventional stator	>98%	20–40	>30
Europe	Advanced Superconducting Motor Experimental Demonstrator (ASuMED) project [35]	1	PM rotor, HTS stator, 8 poles	>97%	20–40	>20
Australia	Magni Alpha superconducting motor (Magni 500) [36]	0.56	N/A	>93%	N/A	N/A
Japan	Massive Electric Generation for Aircraft and Wake Adaptive Thruster Technologies (MEGAWATT) Project [37]	1–20	HTS rotor HTS stator	>97%	20–40	>20
Russia	Hybrid-Electric Propulsion Research at the Skolkovo [38]	0.5–1.5	N/A	>95%	N/A	N/A
France	Advanced Superconducting and Cryogenic Experimental powertrain Demonstrator (AS CEND) [39]	>0.5	PM rotor; HTS stator; 12 poles	>97%	20	12–30

In a word, superconducting motors have the potential to transform aircraft propulsion systems, delivering the highest power density and efficiency, and offering advantages in terms of reduced environmental impact and lower operating costs.

1.3.2 HTS motor thermal management

Though there are many studies working on analysis of superconducting machines, few have considered superconducting cooling system issues. Since superconducting materials have to work under specific low temperatures, thermal design is very important.

Feasible superconducting machine cooling concepts should be identified. The cooling capability of the cryogenics is determined by the amount of AC loss which means that electrical and thermal behaviour are interdependent. An electro-thermal model is presented in [25] where the cooling mechanism is described by empirical equations.

Another idea to figure out cooling design considerations is to use both experiments and computational fluid dynamics modelling (CFD models)[19]. The heat transfer coefficient used in CFD modelling is identified through experiments. Finally, validation of the thermal design is ensured.

A direct calculation method to evaluate the power consumed for cooling [40] is using the coefficient of performance (COP) to calculate power consumed at room temperature to cool 1 W at operating temperature (assume 1400 at 4.2 K, 93 at 20 K, 39 at 40 K, and 14 at 77 K) and then finding the total cryogenic cooling load.

1.3.3 HTS motor challenges

Cryogenic superconducting machines for power generation in electric aircraft applications have been studied for several decades [41]. Although much progress has been made, it is not attractive to be used for aerospace applications yet. One of the main challenges for cryogenic electrical power generation is the lack of superconducting materials having good performance under AC conditions. To meet machines size targets for aircraft application, a 1000–1500 Hz [21] compatible superconductor is essential for a full cryogenic machine. However, without high-frequency AC superconductors available, the AC loss under cryogenic temperature, as mentioned in the previous section, requires high extra energy to be consumed. Voltage regulation is another challenge with superconductors: conventional approaches to voltage regulation will not work with a superconductor machine where the conductors have nearly zero electrical resistance.

The operating temperature of the cryogenic system is another important consideration. Although HTS materials developed today can operate stably at 77 K (easily achieved using LN₂), additional cryogenic coolers are always required. Hence extra weight and space for the cryogenic system are required. These cryocoolers used on aircraft will have to be very robust, with redundant capability on board, to meet safety requirements in the event of a cryogenic component failure[21]. The design of a cryogenic system is complex and the unavoidable extra weight of cryogenic components greatly reduces the specific power. Therefore, it is challenging for HTS power systems to be ready for aircraft applications in 10–30 years.

Therefore, it is important to set good research targets to meet the design requirements. According to the report in[15], the research targets that need to be considered are cost, thermal management and reliability. It also suggests that a system power range of 1–5 MW is

appropriate with an initial focus on 1 MW systems design. In addition, there are many studies considering LH₂ as an HTS machine cryogen[17, 42-44]. According to[17], it is possible to store LH₂ in the flight and use it as fuel after cooling the superconductor cooling. In this idea, there will be no carbon emissions, and in addition, the mass of the flight will be reduced. However, for the same chemical energy, LH₂ has a larger volume compared to conventional kerosene. For this reason, new storage technologies are needed in future[44].

In a word, superconducting motors have the potential to transform aircraft propulsion systems, delivering the highest power density and efficiency and offering advantages in terms of reduced environmental impact and lower operating costs. However, superconducting machines will not be widely used until the two main following issues are solved. The primary challenge in adopting superconducting technologies in aviation includes managing the cryogenic temperatures required for superconductivity, which adds significant complexity and weight to aircraft design. Moreover, integrating these advanced systems within the confined spaces of an aircraft while ensuring reliability across various flight conditions remains a significant engineering challenge. Another challenge is to reduce the very high AC (alternative current) losses[42], especially those produced by HTS materials under cryogenic temperature. The second challenge of understanding and reducing AC loss thus providing more reliable HTS stator design becomes the main research in this study.

1.4 Aim of the study

This thesis focuses on the design and optimisation of HTS armature coils for superconducting motors used in electric propulsion applications which will provide the high power density requirement for future electric aircraft. HTS motors have been developed for decades, however, the strengths of them under different power levels is still unclear. The AC loss evaluation of HTS coils is studied at first with the help of the software COMSOL Multiphysics to simulate the HTS coil performance. In the following section, the strengths of using HTS armature compared to different conventional stator windings, especially Litz wire structure using copper and aluminium, according to different power levels are stated with the help of analytical methodology. The coil performance under different superconducting motor environments (especially under different magnetic loadings) are then investigated, in order to optimise the HTS armature coils design focusing on AC loss reduction thus achieving the desired machine power density. Finally, a new stack structure coil of multiple tapes soldered together is proposed

to increase HTS stator electric loading while maintaining the thermal and mechanical stability. The experiments are always conducted to help validate the simulations.

1.5 Thesis structure

Chapter 1 explains the reason for electric propulsion development, provides an overview of electric propulsion, and introduces the potential use of superconductivity for achieving MEAs/AEAs. This is followed by an introduction to the existing HTS motor topologies for electric aircraft and currently design challenges, including the strengths and weaknesses of using HTS materials in motor design.

Chapter 2 provides a review of superconductivity from the discovery, history and definition of superconductors to categories of superconductors. It reviews the electromagnetic properties behind superconductivity and introduces its potential applications especially in electric aircraft motor design. It also describes the AC loss definition and mechanism of HTS materials, including the details of different types of loss. Finally, it discusses the technical importance of AC loss to HTS propulsion motors.

Chapter 3 reviews the general methodologies used for the AC loss evaluation of HTS. The analytical evaluation methods are introduced first. Then the numerical modelling using a finite element method (FEM) such as the H-formulation is introduced including the existing commonly used FEM methodologies along with their advantages and limitations, and the up-to-date improved simulation methods for large scale HTS. Then the three commonly used AC loss measurement methods, electrical method, magnetic method and calorimetric method which are adopted in this research, are introduced in detail. Finally, a 2G HTS insulated coil is proposed as a testing coil, and validation is conducted for the numerical modelling methods used in this research work.

Chapter 4 proposes a study to compare different radial flux HTS motor topologies for electrified aircraft applications, focusing on the stator core structure and the stator winding choices. Two motor benchmarks of 450 kW and 1 MW are proposed, the iron impact on stator structure is analysed, and various stator windings, including copper/aluminium Litz wires and HTS coils, are compared regarding stator AC loss as well as machine power-to-weight ratio (PTW). This chapter highlights the potentials of using HTS armature windings.

Chapter 5 investigates the transport current AC loss evaluation of standard 2G HTS insulated coils as the electrical loading is vitally important to the HTS stator coil. The 2D H-formula under cylindrical coordinate is used to evaluate the loss, using the same testing coil as for the previous model validation. The transport current AC loss is calculated regarding different conditions related to electric motor design in electric propulsion systems: different applied current and its harmonics, the cryogenic working temperatures and the working frequencies.

Chapter 6 investigates the AC loss of normal 2G HTS armature coils wound with insulated tapes under the real condition of rotating electrical motors. First, the methodology of developing the electrical design of the radial flux machine, in particular the HTS machine, is developed. The performance of the coils is then analysed under different machine environments, specifically different magnetic load levels for partial and full HTS machines.

Chapter 7 studies coil structures considering multi-filament tape coupled together. A new 2G HTS stack coil structure, with two tapes soldered together to increase coil current capacity while improving the coil thermal and mechanical stability, is proposed for the HTS stator design. The coil is wound with two parallel stacks to achieve required the electrical loading. The coil winding layout is described in detail. Then the prepared coil is tested under LN₂ temperature (77K), and measurements taken of the current distribution in each tape or stack, and of the coil transport current AC loss. The properties that impact the loss such as the coil inductance are also analysed. Finally, a 2D axis symmetrical model is developed to help understand the coil losses under AC conditions.

Chapter 8 provides the summary of this thesis and lists the potential related future work.

Chapter 2 Superconductivity background

2.1 Introduction to superconductivity

Superconductivity is a quantum mechanical phenomenon where certain materials can conduct electric current with zero resistance when cooled below a characteristic critical temperature. The theoretical understanding of this phenomenon has evolved significantly since its discovery.

It was Heike Kamerlingh Onnes who discovered superconductivity in 1911 as he investigated electrical conductivity at low temperatures[45]. Over years, superconductors were found to exhibit zero electrical resistance below specific temperatures, which are known as their critical temperatures, by proving a persistent current existing in superconductor rings.

People treated superconductors as ideal conductors until 1933, when Walter Meissner and Robert Ochsenfeld discovered diamagnetic superconductors, which is also known as the Meissner effect. As shown in the figure below, the magnetic field is excluded from the interior of a superconductor if cooled down below the critical temperature, T_c . Thus superconductors have both characteristics of perfect conductivity and perfect diamagnetism. However, this will only happen when the external field is below a certain critical field, H_c .

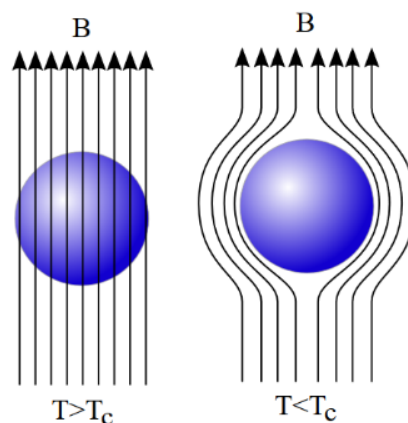


Figure 2.1 Meissner effect of superconductors [46]

Meanwhile, beyond the critical temperature, T_c , and critical field, H_c , there is also a current limit for superconductors, known as the critical current density, J_c . When the current exceeds the limit, the superconducting state is lost and the material reverts to a normal state.

These three quantities are linked together, and the boundary between the superconducting state and the normal conducting state can be described through the critical surface as shown in Figure 2.2. The superconducting state is limited through this surface.

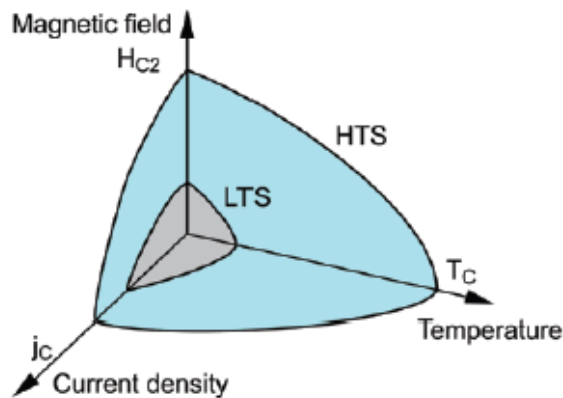


Figure 2.2 Schematic diagram of the critical surface of a superconductor (critical temperature T_c , critical current density J_c , and upper critical magnetic field H_{c2}) [47]

2.1.1 Low temperature and high temperature superconductors

Superconductors can be classified according to their critical temperature. They can be defined as low temperature superconductors (LTS) if their critical temperature, T_c , is below 30 K (Kelvin), or they can be high temperature superconductors (HTS) when T_c goes above 30 K. According to the discovery history of superconducting materials, their T_c ranges from 1.6 K to over 120 K. Figure 2.3 illustrates this discovery history.

LTSs are usually those metals, alloys and some compounds while HTSs are superconducting oxides such as Ba-La-Cu-O and Y-Ba-Cu-O. The discovery of superconducting copper oxides with T_c above 77 K gives a chance to use superconductors in large-scale industrial applications[48]. These copper oxides include lanthanum-strontium-copper-oxide (LSCO), bismuth-strontium-calcium-copper-oxide (BSCCO), and rare-earth-barium-copper-oxide (REBCO, where rare-earth-barium includes yttrium, gadolinium, europium, or neodymium). The BSCCO material has a critical temperature above 100 K and YBCO material (in REBCCO) has the critical temperature at 77 K, which is the boiling point of liquid nitrogen. Therefore, HTS is more attractive because it can be cooled by liquid nitrogen, which is much cheaper than liquid helium. It is noticed that YBCO tapes are commonly used in HTS coils and can be used for armature windings in motor designs.

Low-temperature superconductors (LTS) such as niobium, tin and niobium titanium, which remain superconducting at low temperatures, are often used in high-field magnet applications. These applications include magnetic resonance imaging (MRI) scanners and systems for particle physics experiments such as CERN's Large Hadron Collider, where they help generate the strong magnetic fields needed to guide and accelerate subatomic particles[49-51].

High-temperature superconductors (HTS) such as YBCO or BSCCO have improved our understanding of superconductivity. They become superconducting at temperatures above the boiling point of liquid nitrogen, which means they can be used more easily and cheaply. HTS enables the use of superconductors in power cables, fault current limiters, and even grid-scale superconducting magnetic energy storage systems, thereby improving the efficiency and reliability of power transmission networks[52, 53].

HTSs can be subdivided into first and second generation. First generation (1G) HTS such as BSCCO, are used in applications that can operate at higher temperatures to reduce cooling costs. However, while 1G HTS materials are useful, they are brittle and difficult to form into wires or ribbons, limiting their use in dynamic or mechanical applications[54, 55].

Second generation (2G) HTS are primarily YBCO-based second generation HTS which have much better mechanical properties and higher critical current densities. These are then coated onto textured flexible substrates so that they may be used in applications with higher mechanical requirements, such as motors, generators, and maglev trains. The improved mechanical properties and higher critical current density of 2G HTS make them ideal for applications that require strong, reliable, and efficient superconductors[56-58].

The scope of LTS and HTS applications continues to expand as researchers explore the potential of these materials in renewable energy technologies, digital electronics, and transportation systems. HTS materials are at the forefront of transformative innovations in clean energy technologies, such as wind turbines and electric aircraft, which require efficient and high-capacity power systems[59-62].

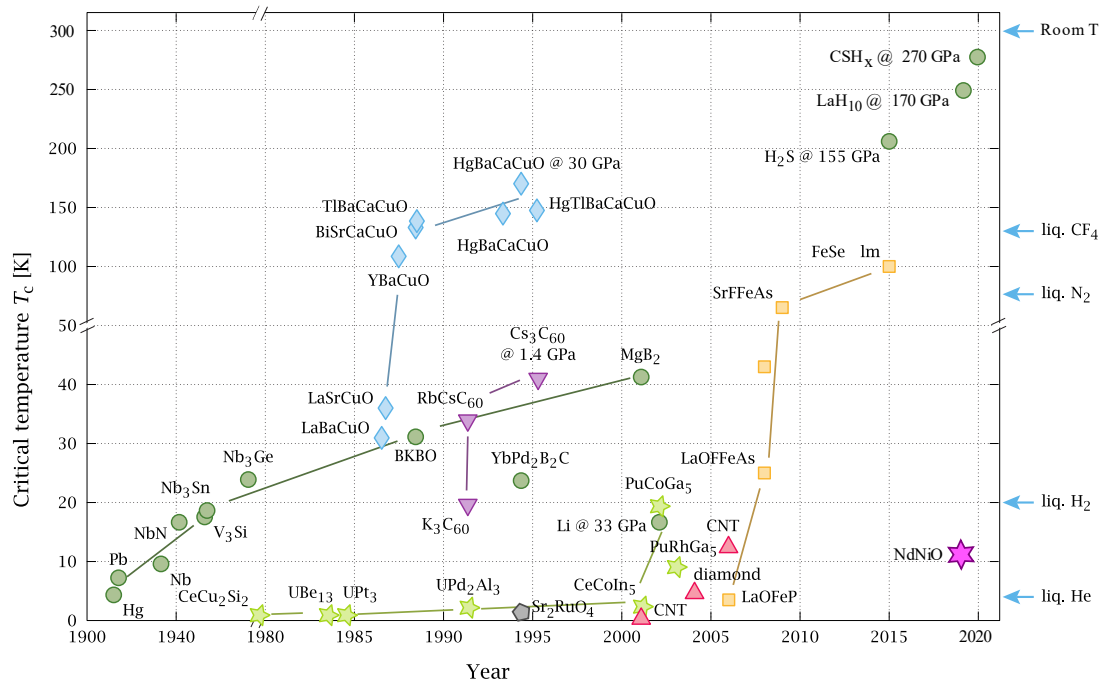


Figure 2.3 Discovery of major superconductors (DoITPoMS, University of Cambridge)

2.1.2 Type I superconductors and type II superconductors

Superconductors can also be categorized by their magnetization properties. Superconductors are named as type I superconductors if they go directly to a normal state as the field increases, and they are called type II superconductors if they enter a mixed state before becoming normal. The details of these two types of superconductors are reviewed in the following sections.

In physics, type I superconductors are referred to as ‘classical superconductors’. These types of superconductors are typically pure elemental metals like tin, lead, or mercury. They have a critical magnetic field at or below which they become superconductive when cooled below their critical temperature and exhibit zero electrical resistance. Under such temperature, magnetic fields are completely expelled from them, showing what is known as the Meissner effect. However, type I superconductors find only limited uses due to their low critical temperatures and magnetic fields. Notably, they are important for magnetic shielding as well as highly sensitive magnetic field detectors. The critical field, H_c , is an important characteristic of a superconductor. If cooled down below T_c in a field $H < H_c$, type I superconductors will expel the field[63]. As the field exceeds H_c , superconductors will transit from the superconducting state to normal state. The temperature dependence of H_c is illustrated in the figure here.

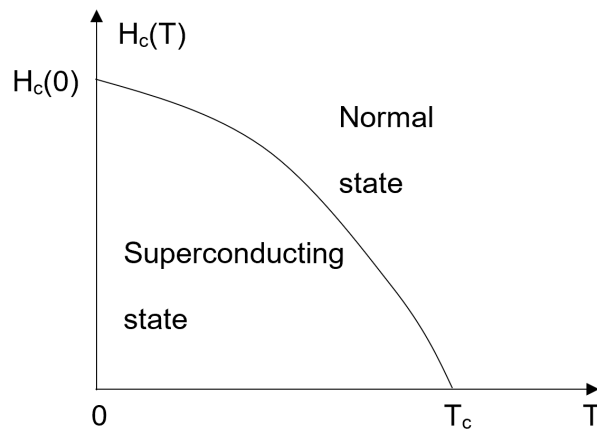


Figure 2.4 The dependence of H_c on temperature for type I superconductors

Shubnikov first found the nature of type II superconductivity through his experiments in 1937. Unlike type I superconductors, type II superconductors are usually made of alloys or intermetallic compounds, which make them more complex. They have two critical fields that are essential to their magnetism. This property allows them to remain superconducting even in very strong magnetic fields by entering a mixed state that allows magnetic vortices to pass through them without destroying the superconductivity. As a result, type II superconductors are used in industry where high magnetic fields are required, such as when building electromagnets for MRI machines or particle accelerator equipment[64, 65]. The dependence of H_c on T_c of a type II superconductor is schematically explained in Figure 2.5. There are two critical fields. For a weak field $H < H_{c1}$, it performs perfect diamagnetism; for field $H > H_{c2}$, it enters normal state; and for a field that lies between two critical fields ($H_{c1} < H < H_{c2}$), the superconductor reaches a state named mixed state. In such a mixed state, type II superconductors have finite resistance, and are able to carry a large current[63]. This characteristic enables type II superconductors be used in large-scale applications.

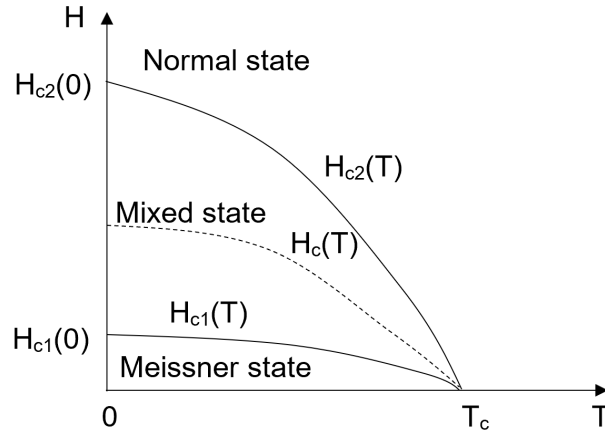


Figure 2.5 The dependence of H_c on temperature for type I superconductors

Type I and type II superconductors have different applications [13][14][15][16]. Type I superconductors are needed for ultrasensitive magnetic sensing, such as scientific instruments that measure magnetic fields at the nanoscale. Type II superconductors are used in extremely severe environments that require high durability and stability. For example, in the aerospace and defence industries, they are used for everything from satellite communication systems to advanced radar technology.

Type I and type II superconductors can be quantified through the Ginzburg-Landau (GL) theory proposed by V. L. Ginzburg and L. D. Landau in 1937. It explains the superconductivity phase transition and helps quantify the distinction between type I and type II superconductors. The GL theory aims to minimize the free energy of a superconductor through finding two functions: a wavefunction and a magnetic vector potential function in a spatial coordinate. Two length scales are also introduced for the purpose of superconductor classification[63, 66]. The coherence length, ξ , is a distance near the boundary of the superconducting and normal states where the density of a cooper pair reaches a constant density. The penetration depth, λ , is a length for external field decay exponentially to zero in a superconductor. The important dimensionless GL parameter is defined here,

$$\kappa = \frac{\lambda}{\xi} \quad (2.1)$$

A superconductor belongs to type I if $\kappa < \frac{1}{\sqrt{2}}$, otherwise it is a type II superconductor.

2.1.3 Structure of 2G HTS tape using YBCO HTS material

Reasons for the widespread use of YBCO is its unique crystal structure which includes yttrium atoms located between CuO_4 planes and barium atoms located between CuO_2 ribbons and CuO_4 planes (Figure 2.6). This structure leads to significant differences in superconducting and non-superconducting properties because the resistivity within the CuO_4 planes is lower compared to the CuO_2 ribbons. The smaller ionic radius of yttrium (Y) compared to other rare earth elements such as gadolinium (Gd) or europium (Eu) leads to a higher charge carrier density in the superconducting CuO_4 planes. In addition, YBCO shows lower electronic anisotropy and higher irreversibility field compared to GdBCO and EuBCO, making it a favourable choice for the production of commercial HTS coated conductors. The increasing popularity of YBCO has made it useful in large high-field magnets and high current coils. The armature windings in this research are also made of YBCO tapes.

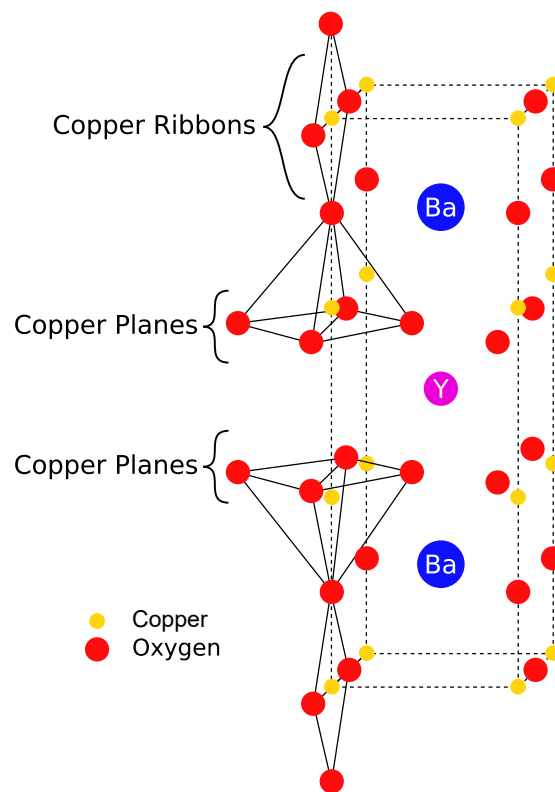


Figure 2.6 Part of the lattice structure of YBCO (CC BY-SA 3.0)

The REBCO tape structure is displayed in Figure 2.7. Taking YBCO tape we introduced as an example: The YBCO (Yttrium Barium Copper Oxide) tape structure comprises multiple layers,

each with specific materials and dimensions designed to optimize superconducting properties. The base is a substrate layer made of Hastelloy or stainless steel, typically with the thickness of 50 to 100 μm , providing mechanical support and flexibility. Above the substrate are buffer layers (usually 5 layers and 50–200 nm each) of materials like cerium oxide, yttria-stabilized zirconia, and lanthanum aluminate, which facilitate the epitaxial growth of the YBCO layer and prevent interdiffusion. The superconducting YBCO layer, usually only 1–2 μm thick, is the core of the tape, responsible for its superconducting properties. Stabilization layers of silver (1–2 μm) and copper (20–50 μm) provide thermal and electrical stability, while protective silver layers (1–2 μm) guard against environmental degradation and mechanical damage. Each layer's material and thickness are cautiously chosen to ensure the tape's optimal performance and durability.

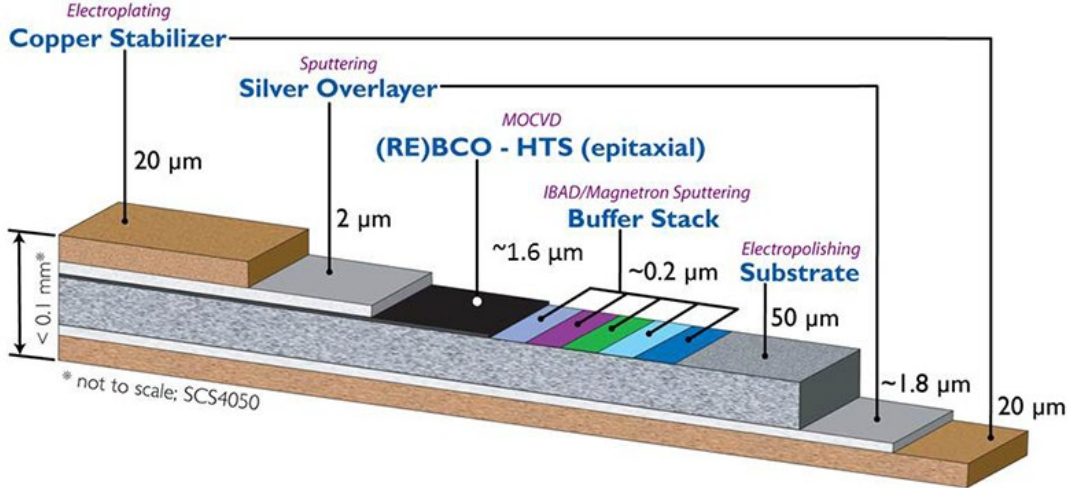


Figure 2.7 Architecture of a standard SuperPower 2G HTS tape using REBCO HTS material

2.2 Critical state model of type II superconductors

2.2.1 Flux pinning

As a magnetic field penetrates into a type II superconductor in the mixed state, the flux inside superconductors performs as tubes, which are named as vortices[66]. Components of a vortex are shown in Figure 2.8. The flux goes through a core with radius of the coherence distance, ξ , and screen currents flow around that core with a radius of the penetration depth, λ , and decrease exponentially.

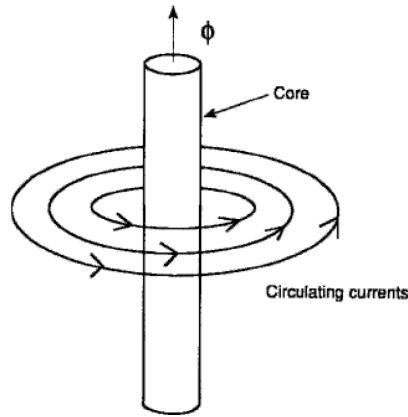


Figure 2.8 Diagram of a vortex [67]

When two vortices are close to each other, a repulsive Lorentz force exists between one vortex's screening current and the other's magnetic flux.

If transport current is applied to a type II superconductor in the mixed state, there will be a Lorentz force between transport current and vortices. As the transport current is fixed by the superconductor boundaries, vortices will move perpendicular to the current direction thus generating an electric field along the direction of the transport current. The V-I characteristic performs as a resistance, as a result, a loss is generated in a type II superconductor. Flux pinning is introduced to help type II superconductors carry large transport current with no loss. It fixes vortices by adding impurities which require less energy to form vortices in these positions (known as pinning centres). The critical current density, J_c , is defined where the average pinning force is equal to the Lorentz force.

2.2.2 Flux creep, flux flow and E-J power law

Ideally, there is no loss in a superconductor with DC transport current or field when the current density is less than the critical current density. However, in a real situation, when the temperature is above zero, vortices may "creep" out of the pinning centres as a result of thermal fluctuations. This flux creep matters because vortex motion will induce an electric field thus power dissipation in the superconductor. When current density, J , exceeds J_c , the pinning force is no longer greater than the Lorentz force, hence the vortices start to flow. This is the flux flow state. E-J power law [68] describes these two characteristics:

$$E = E_0 \left(\frac{|J|}{J_c} \right)^n \frac{J}{J_c} \quad (2.2)$$

where n is a constant depending on materials and temperature, and E_0 is 10^{-4} V/m.

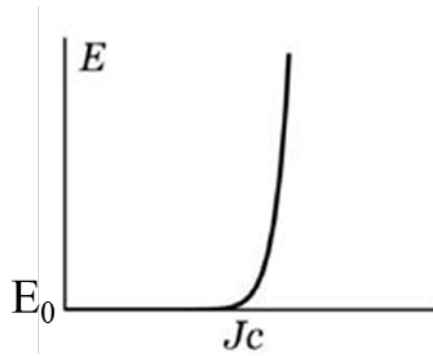


Figure 2.9 An example of flux creep and E-J power law to determine critical current density

2.2.3 Bean's critical state model

The model was proposed by Bean in 1962. The critical state model (CSM) is a macroscopic scale model [69] which replaces detailing individual vortices by an average taken over a large number of vortices. This model provides a fundamental understanding of the dynamics of magnetic flux penetration and distribution in type II superconductors. In Bean's model [70], when an external field is applied to a type II superconductor, the magnetic field will not penetrate the material uniformly and is equal to the superconductor's volumetric average of $\mu_0 H_s$, where H_s is the magnetic field within the superconductor. Figure 2.10a shows a type II superconducting slab infinitely high (along the y-direction) and deep (along the z-direction), and $2a$ wide (along the x-direction). When an external field H_e is applied parallel to a slab, a magnetic field $H_s(x)$ within the slab is produced. Regarding Ampere's law, this field satisfies:

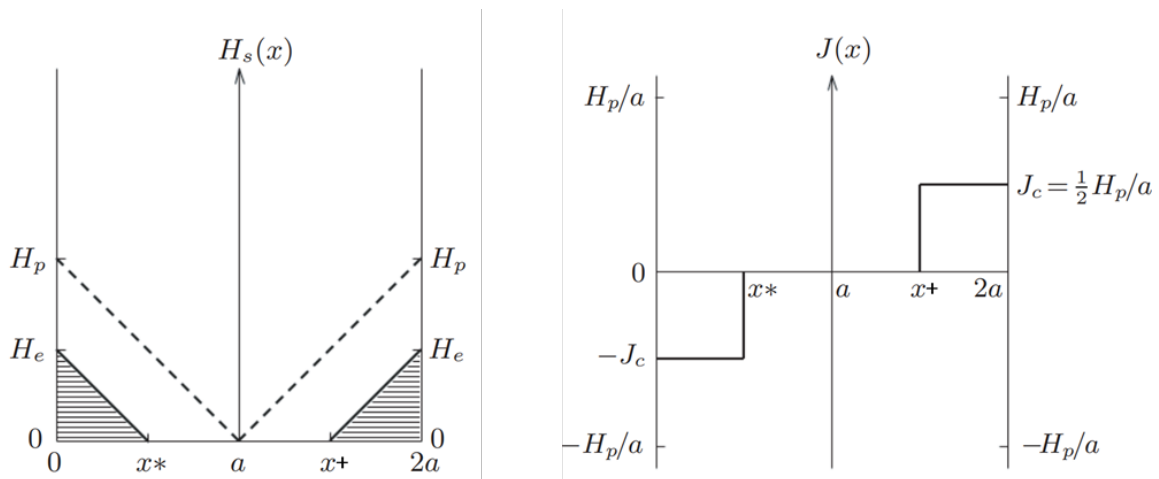


Figure 2.10 a) Slab of type II superconductor under an external field [70]; b) critical current density $J_c(x)$ corresponding to $H_s(x)$

$$H_s(x) = \begin{cases} 0 & (x^* \leq x \leq x^+) \\ H_e - J_c x & (0 \leq x \leq x^*) \\ H_e + J_c(x - 2a) & (x^+ \leq x \leq 2a) \end{cases} \quad (2.3)$$

It also proposes that, microscopically, the electrical current density in any part of a hard superconductor is either zero or is equal to the critical current density, J_c . After considering the fact that the change in magnetic field is related to the existence of the electrical field, E , he provided a formulation to describe current density in a hard superconductor[69]:

$$|J| = \begin{cases} 0, & \text{where } E = 0 \text{ in all history} \\ J_c, & \text{elseswhre} \end{cases} \quad (2.4)$$

2.2.4 Kim-Anderson Model

Compare to Bean's model, the Kim-Anderson model provides a more detailed and dynamic picture of how magnetic flux behaves in type II superconductors. It considers the impact of magnetic field on the critical current density, and can be expressed as[66]:

$$J_c(B) = \frac{J_{c0}}{1 + B/B_0} \quad (2.5)$$

where J_{c0} is the critical current with no external field, and B_0 is a constant.

The model helps in analysing the AC losses in type II superconductors, which are important for the design of superconducting cables and other devices operating in alternating current environments.

2.3 AC loss in 2G HTS tape

2.3.1 AC loss mechanisms

Generally under direct current (DC) conditions, superconductors have zero electrical resistance, i.e. there is no power dissipation when carrying a DC. However, there will be energy loss under alternating current (AC) conditions. The energy loss can be treated as the result of the voltage induced in the conductor. This energy loss is called AC loss of superconductors. The production of AC loss could be explained with the help of the superconductor magnetization process: as indicated in Figure 2.11[71], a superconductor is placed in a time-varying external magnetic field. As the field increases along the y-axis positive direction, it gradually penetrates the superconductor in the form of magnetic vortices (flux lines) pinned to the superconductor material. The internal magnetic field changes as the applied magnetic field changes. Regarding

Faraday’s law, $\nabla \times \mathbf{E} = -\frac{\partial \mathbf{B}}{\partial t}$, the magnetic field variation inside the superconductor induces an electric field, \mathbf{E} . As a result, there will be screening currents in the material due to this electric field, \mathbf{E} . The screening currents circulating the superconductor are shown in Figure 2.11a. The screening currents (white) shield the interior (grey) from the magnetic field. According to Ampere’s law, $\nabla \times \mathbf{B} = \mu_0 \mathbf{J}$, the screening currents determine the magnetic field distribution in the superconductor. With this induced electric field, \mathbf{E} , as well as the current flowing in the material, there will be an energy dissipation given by $\mathbf{E} \times \mathbf{J}$. This energy is required for depinning the flux lines or leading to the movement of the vortices inside the material. The energy provided by the magnet generating the field, in the end, is converted into heat dissipation. Considering the HTS working environment requires cryogenic temperature, this heat dissipation has to be removed by the cooling system. Therefore, AC loss is an undesirable phenomenon and needs to be reduced as much as possible[71, 72].

In reality, the screening currents could be induced by the variation of either the current flowing inside the superconductor materials or the applied external magnetic field in the mode of AC cycle. Therefore, AC loss is vitally important for applications where the superconductors have to experience time-varying (AC) currents or are under an external time-varying magnetic field, such as the HTS electrical machines studied in this research.

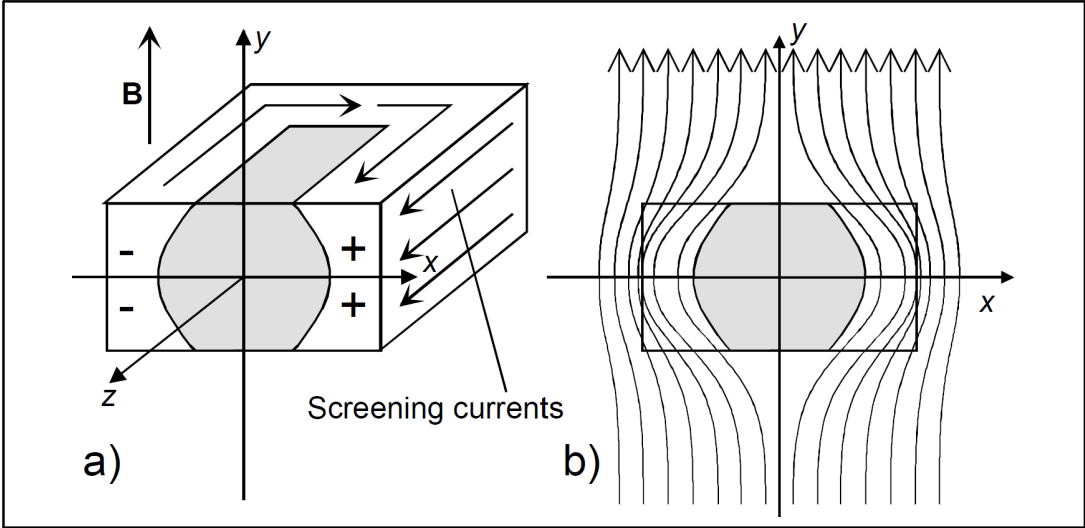


Figure 2.11 Cross-section of a superconductor under a time-varying external magnetic field

As for the source of the AC loss in an HTS tape, all layers have been taken into account, which means the loss occurs in different positions in a tape. Recalling the structure of 2G HTS tape, i.e. one HTS layer, two copper stabilizers, one silver overlayer, as well as one substrate. Total

losses include not only superconducting hysteresis losses in the superconducting layer but also eddy-current losses in metal parts, coupling losses caused by interactions between coupled superconducting filament currents, and ferromagnetic losses related to magnetic materials. The explanations of different AC loss are given in this section.

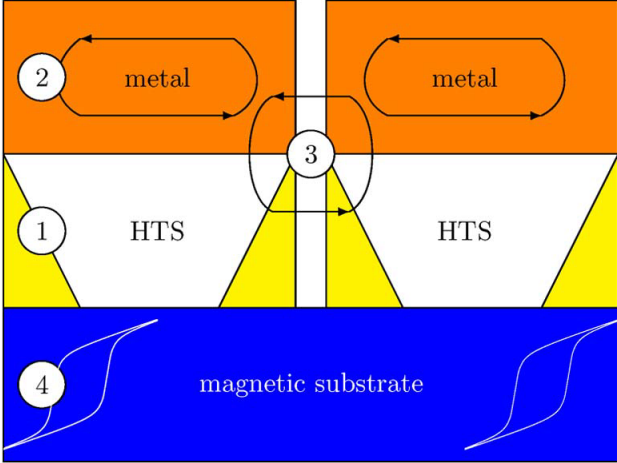


Figure 2.12 Schematic of the different loss contributions in technical HTSs 1) Hysteresis losses in the superconductor; 2) eddy current losses in the normal metal stabilizer; 3) coupling losses between filaments (e.g., through conducting paths due to imperfections of the striation process); and 4) ferromagnetic losses in the substrate. [69]

2.3.2 Hysteresis loss

Hard superconductors are those whose flux tubes are strongly pinned to preferred positions. Under DC conditions, whether transporting a DC current or under a DC magnetic field, a superconductor could have zero resistance[63, 66]. However, under AC conditions, the vortices must move due to the change of the penetrating magnetic field[69]: The pinning force performs as an obstacle, and it is an irreversible process to supersede it. The accompanied dissipation is the hysteresis loss in hard superconductors. In many superconducting applications, the prospected AC loss value is too high to make the application attractive on the market[69].

Hysteresis loss occurs due to the movement of magnetic vortices within the superconducting material[72]. These vortices are pinned by defects and impurities, and their movement generates energy dissipation. The hysteresis loss is directly proportional to the area of the hysteresis loop in the magnetization curve of the superconductor. This type of loss is significant in type-II superconductors like YBCO, where flux pinning is a dominant mechanism.

Beyond hysteresis loss in the HTS material itself, for technical superconductors consisting of a superconductor as well as metal, substrates and magnetic materials, there are other types of loss.

2.3.3 Other types of AC loss

Eddy-current loss arises from the induced currents in the superconducting material or its stabilizing metal layers when exposed to time-varying magnetic fields. These currents flow in loops within the material, causing joule heating and energy dissipation. The magnitude of eddy-current loss depends on the frequency of the applied magnetic field and the electrical conductivity of the material. In HTS, eddy-current loss is particularly relevant in metallic stabilizers and the superconducting matrix[73].

Coupling loss occurs in multifilamentary superconductors due to the interaction between different filaments through the matrix material. When an external magnetic field changes, it induces currents that couple between the filaments, causing energy dissipation. This loss is influenced by the twisting and transposition of the filaments, as well as the resistivity of the matrix. Coupling loss can be a major contributor to AC losses in superconducting cables and wires[74].

Ferromagnetic loss is observed in superconducting composites where ferromagnetic materials are used as stabilizers or substrates. The time-varying magnetic field induces magnetization changes in the ferromagnetic material, leading to hysteresis and eddy-current losses within the ferromagnetic components. This loss is significant in HTS tapes and wires with ferromagnetic substrates[69].

Therefore, the total losses occurring in HTS tapes include not only superconducting hysteresis losses but also eddy-current losses in metal parts, coupling losses caused by the coupling of superconducting filament currents, and ferromagnetic losses related to magnetic materials.

2.3.4 Existing HTS motor topologies for electric propulsion

2.3.4.1 Partially superconducting synchronous machines

Many achievements of partially superconducting synchronous machines have been developed since the discovery of HTS in 1986[42]. The benefits of high-temperature superconductors (HTS) can be maximized by integrating part of the superconducting machine into the rotor or stator and using conventional components in the opposite part. This approach combines the excellent magnetic properties of HTS materials with design simplicity and cost-effectiveness.

PSCMs can be subdivided into two options: superconducting rotor with conventional stator windings and normal rotor with superconducting stator windings. Currently, there are many design concepts that consider the former option while the latter is less focused.

Superconducting rotor with conventional stator windings designs that combine HTS stators with standard copper rotors optimize electromagnetic interactions to improve overall efficiency. For example, a rotor using YBCO tape achieves an average flux density of 1.8 Tesla and operates at a power density of 6.6 kW/kg, keeping the operating temperature around 25 K. It is suitable for compact aerospace applications that require high torque and high efficiency[75]. Another design uses a rotor with trapped flux magnets to optimize flux density without continuous external magnetization, achieving a power density of 7 kW/kg at 20 K[76]. Advanced rotor configurations are able to produce a power density of 7.5 kW/kg and a flux density of 3 Tesla at an operating temperature of 20 K, demonstrating the power of HTS[77].

In this type of machine, only the superconducting coils in the rotor are put into the cryostat. A torque tube is used in the cryostat for rotating machines to connect the cryogenic temperature part with the room temperature part. A structure of this kind of PSCM is illustrated in the figure below.

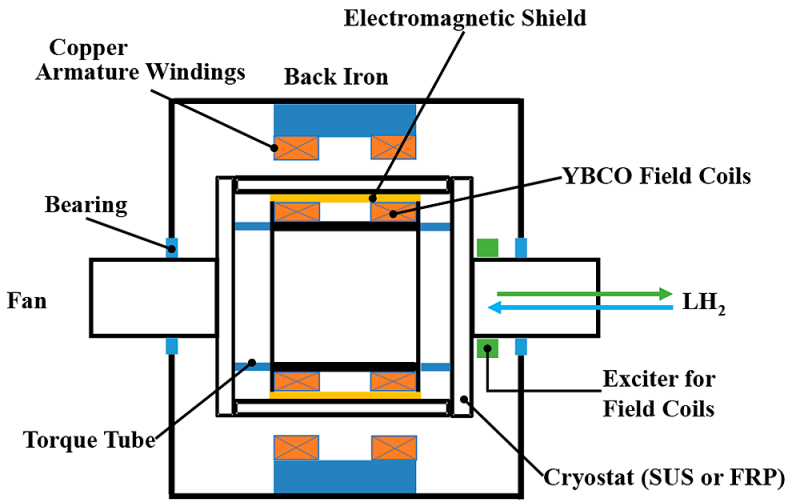


Figure 2.13 The structure of PSCM with cryostat [20]

In such a design in Figure 2.13, the cryostat materials are usually stainless steel (SUS) or fibre reinforced plastic (FRP) and the coolant is liquid hydrogen (LH₂). Regarding[20], without the use of superconducting cryogenic, the machine could achieve 14.4 kW/kg and 16.9 kW/kg at a rated power of 3 MW and 5 MW, respectively. Another PSCM using the same idea is presented

in[25]. Using Novec 7500 as the cooling liquid, this design can achieve a power density of 10.2 kW/kg at a rated power of 3 MW.

HTS stator and conventional rotor, on the other hand, refers to a machine with an HTS stator incorporated into a copper-based rotor. The goal is to improve overall system efficiency by increasing magnetic coupling throughout the stator. Motors that incorporate BSCCO HTS stators are able to achieve power densities up to 16 kW/kg at 20 K, which is a significant improvement over previously manufactured models[78]. Another design pairs the two components together with a power density of 13 kW/kg, thereby focusing on minimizing heat losses during operation while still achieving the highest motor efficiency levels[79]. Another type uses YBCO coated conductor windings, achieving a power density of 7.5 kW/kg and producing 3 T at 20K, which also makes them ideal for aircraft propulsion systems as they have advantages such as producing higher torque[80].

Based on the research in[25], the designs of PSCM with the best power density have relatively low airgap magnetic flux densities in the range from 0.55 to 0.9 T. With this low field range, the stator electrical loading can be maximized thanks to high current capacity of HTS. These magnetic flux densities can be accomplished by PM as well. Therefore, a PSCM with superconducting armature winding and a rotor using Halbach PMs is worth studying.

2.3.4.2 Fully superconducting machines

Fully superconducting machines use HTSs for both the stator and rotor components. This enables not only high magnetic loading on the rotor but also achieves high electric loading on the stator. A slotless design without an iron core is chosen to reduce the machine weight. This allows fully HTS machines to be more efficient, have a higher power density, and deliver better electromagnetic performance[42].

These machines are necessary when a great deal of energy must be saved during high-power applications. According to the review work in[81], fully superconducting machines are a significant advancement in motor technology which can be applied in various fields such as aerospace due to their reduced size, high efficiency, and increased power output. This is also supported by the different prototypes of industrial scale synchronous HTS motor systems built, some of which are given in Table 1.1.

Some existing fully HTS motor designs are given here. A prototype using YBCO windings as both stator and rotor at 20 Kelvin (K) could deliver 7.5 kilowatts per kilogram (kW/kg) power density[82]. Another type of fully HTS motor using multi-filament MgB₂ superconducting wires could achieve 6.6 kW/kg power density at 25 K offering improved thermal stability as well as operational efficiency[83]. Another mixed HTS material motor design using YBCO plates and MgB₂ wires is also proposed[84]. At 20 K, this motor has a power density of 7 kW/kg and an average flux density of 1.8 T. It shows that we can have propulsion systems with very high efficiency to meet the tough requirement of electrical aircrafts.

Compared to PSCMs, putting armature and field coils in the same cryostat makes for FSCMs with a smaller airgap[20]. Matthias et al. stated that FSCMs could achieve 3.5 times higher power density than PSCMs[25]. Though a significant size reduction can be realized through this kind of design, the cooling structure can be more complicated. Meanwhile, AC losses in stator and rotor are interdependent which makes the investigation even more complex[85].

The general options for both superconducting stator and rotor design for radial flux motor designs are summarized in the figure below.

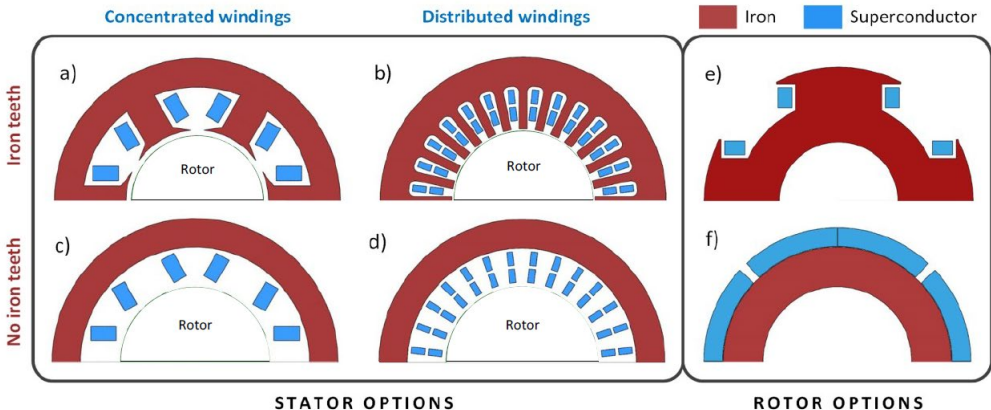


Figure 2.14 Design options for superconducting stator and rotor in radial motors. Stator types: a) b) Concentrated and distributed windings with iron teeth; c) d) Concentrated and distributed windings with no iron teeth. Rotor types: e) Salient pole version; and f) surface-mounted superconducting magnets or coils. [85]

Machine stator design depends on two main factors: whether windings are concentrated or distributed, and whether with iron teeth or not. There is still a lack of evidence to show which option performs the best [85]. As for the rotor, option e in Figure 2.14 is suitable for the rotor using coils while option f in Figure 2.14 is designed for superconducting bulks of stacks of HTS tape. The radial flux motor designs usually requires stator back iron to enhance the magnetic

loading [85], however, coreless stator is sufficient in axial flux motor designs thanks to its compact structure [86-88].

Charalampos et al. focused on superconducting machine stator design and proposed a stator structure with flux diverter in[28]. The schematic diagram of this structure is shown below.

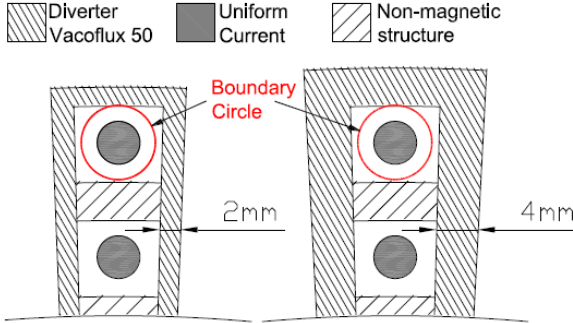


Figure 2.15 Schematic diagram of thin (left) and thick (right) flux diverter position around the stator superconducting coils [28]

This C-shape flux diverter allows for flux passing around coils while reducing flux passing through the coils. Their research also considered the influence of the air core, and the thickness of the flux diverter as well as pole numbers on superconducting losses.

Generally, HTS tapes or bulks are used for field winding while HTS tapes or MgB₂ wires are selected for armature windings. Magnetic flux density in the air gap is greater than 1 T and machine power density can easily exceed 20 kW/kg[25, 28], [19], [20],[85]. However, there is still a long way to go before FSCMs can be realized. Evaluation of AC losses and the requirements of superconducting cooling systems are two main issues that need to be considered carefully.

2.4 Technical importance of AC loss to HTS propulsion motors

Superconductors are developed for application in high-power devices such as transformers, power-transmission cables, motors and generators. To become competitive to normal conductors, superconductors have to meet both the main requirements of a high critical current and a low unit price. In addition, the AC loss should be low enough to make the extra investment in the superconductor and the cooling equipment reasonable. The use of superconductors is mainly determined by financial considerations: the cost of energy, the superconductor price (including extra production steps intended to decrease the AC loss), the cost of the cryogenic

component, maintenance and reliability[71]. As mentioned before, the AC loss in a superconductor is much lower than that in a normal conductor under the same circumstances. However, the AC loss reduction is vitally important as the energy is dissipated in the form of heat in a low-temperature environment. Extra energy is needed by the cryogenic equipment to remove this low temperature AC loss, and this extra energy is usually much greater than the dissipated heat. Regarding[89], the total power consumption of a typical device operating at 77 K (LN₂ operating temperature) is about 15 times the AC loss in the superconductor. Therefore, it is necessary to accurately predict the AC loss and meanwhile minimize the total AC loss.

In superconducting machines, the magnetic loading is set to 1–2 T [71] to increase the total output power. In general fully HTS machine designs, the rotor has DC HTS windings to achieve a nearly constant magnetic field; and the stator has AC HTS windings to subject to the rotating magnetic field produced by the rotor. The main AC loss in a fully HTS machine is generated from the stator AC windings. This AC loss is mainly influenced by the external rotating magnetic field component perpendicular to the tape wide surface and the transport AC current applied to the tape (and the formed coil). In general, from an AC-loss viewpoint, the construction of a fully superconducting motor is a greater challenge than other high-power devices.

2.5 Conclusion

This chapter provides a review of superconductivity from the discovery history and definition of superconductors to categories of superconductors. It reviews the electromagnetic properties behind superconductivity, such as the Meissner effect. It also introduces the discovery of critical temperature, current density, and magnetic field behaviour of the superconducting state.

The distinction between low-temperature superconductors (LTS) and high-temperature superconductors (HTS) provides a framework for analysing their practical applications and material properties. While LTS, including metals such as niobium and tin, are suitable for high-magnetic field applications such as MRI machines and particle accelerators, HTS materials such as YBCO hold great promise for energy-efficient, large-scale applications due to their operability at liquid nitrogen temperatures. The structural properties of HTS, especially the layered structure of 2G HTS tapes, enable improved performance in demanding environments such as electric motors, renewable energy systems, and advanced transportation technologies.

Considering the critical temperature, superconductors can be divided into low-temperature superconductors (LTSs) and high-temperature superconductors (HTSs). Generally, LTSs with lower working temperatures require more expensive coolant (such as liquid helium) while the HTSs with higher critical temperatures need much cheaper coolant (such as LN₂). Moreover, HTSs can work under a higher magnetic field. Hence, HTSs are more widely considered in engineering applications.

Regarding the transition between the superconducting state and normal state, superconductors can be also categorized into Type I and Type II superconductors. While Type I superconductors transition from the superconducting state directly towards normal state, Type II superconductors have a mixed state between purely superconducting state and purely normal state. The Ginzburg-Landau theory, along with coherence and penetration length, helps to classify the two types.

AC loss is an important consideration in the use of superconductors, especially in high-power applications like motors. Unlike zero-resistance performance in DC conditions, AC conditions induce losses. This energy loss is crucial as additional energy is required to remove it under cryogenic temperature. The mechanism behind the AC losses, and different types of AC losses such as hysteresis losses, and coupling losses are explained in this chapter as well. Followed by the overview of existing HTS motor topologies for electric propulsion, the technological importance of AC loss and its decrease is explained, particularly in superconducting propulsion motors, where optimizing the magnetic field and minimizing AC losses are critical in terms of power density and efficiency.

Chapter 3 AC loss evaluation of HTS

3.1 Introduction

This chapter reviews the general methodologies used for the AC loss evaluation of HTS. They are analytical methodologies, numerical modelling methodologies and the experimental methodologies. The analytical methodologies that help to give an initial evaluation of the AC loss are introduced first. Then a comprehensive overview of numerical modelling methodologies is presented, including different electromagnetic formulae explanations, from the widely used general H-formula to the efficiently simplified T-A formula and their strengths and weaknesses. Subsequently, the up-to-date improved numerical modellings adapted to large scale HTS are introduced. Finally, the three commonly used measurement methodologies, electric method, magnetic method and calorimetric method are reviewed as well as their strengths and weaknesses. In addition, a testing coil made of 2G YBCO tapes is proposed here. The transport current loss is measured using the electric method and, with the help of the measurement results, the validation of the numerical models used in this research work is conducted.

3.2 Analytical analysis of AC loss calculations

The calculation of AC loss contains three main steps. First, the E(J) relation should be identified. Besides the consideration of flux creep and flux flow which was mentioned previously, spatial variation of the critical current density (i.e. anisotropy[90]) should also be considered for the refinements of E-J power. The most important step is to solve the electromagnetic quantities. The possible state electromagnetic variables are stated according to Maxwell's equations:

$$\nabla \times E = -\frac{\partial B}{\partial t} \quad (3.1)$$

$$\nabla \times B = \mu_0 J \quad (3.2)$$

The state variables vary with the simulation method. For electric field, the variables are current density, $J(r,t)$, and the related current vector potential, $T(r,t)$; while for magnetic field, the variables are magnetic field, $H(r,t)$ and the magnetic scalar potential $\Omega(r,t)$ or magnetic vector potential, $A(r,t)$, where r and t are position vector and time, respectively[69]. Then the density of local power dissipation:

$$p = \mathbf{J} \cdot \mathbf{E} \quad (3.3)$$

The total AC loss per cycle is obtained through the integral of dissipation in the superconductor domain:

$$Q = \int_0^t \int_V \mathbf{J} \cdot \mathbf{E} dV \quad (3.4)$$

where t is the period cycle, and V is the superconducting domain. Transport loss is the loss produced by transporting an AC current, and magnetization loss is caused by the external AC field[91].

It is common to categorize AC loss according to the source of AC loss: transport current loss refers to the loss due to the current transporting inside the superconductors without any external magnetic field, while magnetisation loss is caused by the external magnetic field without any current flowing inside the superconductors. Magnetization loss consists of hysteresis loss, coupling loss and eddy current loss as introduced in previous sections. Transport current loss consists of hysteresis loss and flux flow loss[72]. Among the transport current losses, the hysteresis loss is produced as a result of a time-varying magnetic field generated by the current flowing through the superconductors. This field is defined as the self-field of superconductors. The flux flow loss exists as the transport current increases thus more and more vortices are moving in the superconductors.

The transport current loss could be evaluated by[72, 92]:

$$P_{trans} = \frac{\mu_0 f I_{c0}^2}{\pi} [(1 - i) \ln(1 - i) + (1 + i) \ln(1 + i) - i^2] \quad (3.5)$$

This expression describes the average transport current loss per unit length regarding the Norris equation [93]. If there is an HTS tape that carries an AC current with the amplitude of I_t with the frequency of f , with its self-field critical current I_{c0} , then the load current ratio, $i = I_t/I_{c0}$. It is noticed that as the load current ratio increases sufficiently high, part of the current will flow into the normal conducting layers of the HTS tape thus leading to a conventional resistive loss contribution.

The magnetization loss could be evaluated by[72, 92, 94]:

$$P_{mag} = 4\pi\mu_0 w^2 f H_0 H_c \left\{ \frac{2H_c}{H_0} \ln \left[\cosh \left(\frac{H_0}{H_c} \right) \right] - \tanh \left(\frac{H_0}{H_c} \right) \right\} \quad (3.6)$$

If there is an HTS tape placed under an external AC magnetic field perpendicular to its wider surface, with the amplitude of B_{ext} or the magnetic strength of $H_0 = B_{ext}/\mu_0$, and H_c describes the characteristic field generated by $I_{c0}/(2w\pi)$, then this expression above describes the average magnetization power loss per unit length regarding the Brandt equation [92] where f is the frequency of the magnetic field, and the HTS tape has the width of $2w$, the thickness of h , and the self-field critical current of I_{c0} .

When an HTS tape with the dimension of $2w$ in width and h in thickness is placed under an AC magnetic field and meanwhile carries an AC transport current, and two AC loss sources have the same frequency as well as the initial phase shift, then the total average power dissipation per unit length could be evaluated by:

$$P_{AC} = \frac{\mu_0 f I_{c0}^2}{4\pi} \left(\frac{b}{w}\right) (P_1 - pP_2) \quad (3.7)$$

where:

$$P_1 = \alpha A \operatorname{arccosh} \alpha - \alpha^2 + \beta B \operatorname{arccosh} \beta - \beta^2 + 2 \quad (3.8)$$

$$P_2 = -A(\alpha + 2\beta) - B(2\alpha + \beta) + 2(\alpha + \beta)^2 \operatorname{arctanh} \left(\frac{AB}{\alpha\beta + 1}\right) + 2AB \quad (3.9)$$

and all other constants:

$$c = \tanh \left(\frac{\pi B_{ext}}{\mu_0 J_{c0} h}\right), \quad b = w\sqrt{1 - i^2}\sqrt{1 - c^2}$$

$$p = \sin(i - c), \quad \alpha = w \left(\frac{1+ic}{b}\right), \quad \beta = \left(\frac{1-ic}{b}\right)$$

$$A = \sqrt{\alpha^2 - 1}, \quad B = \sqrt{\beta^2 - 1}$$

3.3 Numerical modelling methodology

3.3.1 General numerical modelling for HTS materials

Nowadays, 2G HTS has shown potential for large-scale industry, like superconducting machines, which will be focused on in this study. As large-scale superconducting systems are made from hundreds or even thousands turns of HTS tapes, it is important to find an efficient method to study electromagnetic properties (e.g. AC loss) of HTS thus helping design and operation. Numerical modelling is a powerful tool for electromagnetic studies of HTS. There are three typical finite element method (FEM) models derived from Maxwell's equations: H-

formulation[95], A-V formulation [96] and T- ϕ formulation[97]. They are named by the state variables to be solved[68]. However, these methods are usually memory and time consuming and often used for small-scale systems. The study in [98] proposes a T-A model for the accurate and efficient calculation of 2G HTS tapes. Different formulas used to solve Maxwell's equations and numerical models for HTS electromagnetic behaviour simulations are summarized in the table below.

Table 3.1 Different formulae used to solve Maxwell's equations and numerical models for HTS electromagnetic behaviour simulations [99]

Formulation	Equations	Definitions
A - V	$\nabla^2 \mathbf{A} = \mu\sigma \left(\frac{\partial \mathbf{A}}{\partial t} + \nabla V \right)$	$\mathbf{B} = \nabla \times \mathbf{A}$
	$\nabla \cdot \left(\sigma \frac{\partial \mathbf{A}}{\partial t} + \sigma \nabla V \right) = 0$	$\mathbf{E} = -\frac{\partial \mathbf{A}}{\partial t} - \nabla V$ $\sigma = \sigma(E)$
T - ϕ	$\nabla \times \rho \nabla \times \mathbf{T} = -\mu \frac{\partial(\mathbf{T} - \nabla \phi)}{\partial t}$	$\mathbf{J} = \nabla \times \mathbf{T}$
	$\nabla^2 \phi = 0$	$\mathbf{H} = \mathbf{T} - \nabla \phi$ $\rho = \rho(J)$
E-field	$\nabla \times \nabla \times \mathbf{E} = -\mu \frac{\partial(\sigma \mathbf{E})}{\partial t}$	$\frac{\partial \mathbf{B}}{\partial t} = -\nabla \times \mathbf{E}$ $\sigma = \sigma(E)$
H-field	$\nabla \times \rho \nabla \times \mathbf{H} = -\mu \frac{\partial \mathbf{H}}{\partial t}$	$\mathbf{J} = \nabla \times \mathbf{H}$ $\rho = \rho(J)$

The A-V formulation is a proven method for simulating both conventional materials and some superconductors[100]. It was first developed in Flux2D by Nibbio et al. in 2001[101, 102]. It uses the magnetic vector potential, A , and electrostatic potential, V , as state variables, where V is often disregarded in many cases[96]. This 2D model was further extended into 3D in Flux3D environment by Cedrat for solving 3D problems[102]. In [103, 104] a co-tree gauged T-f FEM and an A-V-J formulation solver is presented by Stenvall and Tarshasaari for computing the hysteresis losses of superconductors. These two formulations were compared with the H formulation considering degrees of freedom (DOF) and computation efficiency, as well as accuracy[105]. With the same mesh size, the A-V-J formulation-based solver can be less time-consuming than the other solvers in computational speed, however it was found that the A-V-J formulation usually needs a denser mesh to get solid outcomes compared to the H and T-f formulations.

The E-formulation was developed to reduce calculation time by avoiding the derivative calculation. Nevertheless, this might lead to convergence problems because of its strongly non-linear E-J power law[106]. It shows that this divergence appears frequently when the n-value is greater than 20. Hence it is not frequently used now.

The H-formulation [99, 107, 108] is the most widely used formulation to solve electromagnetic problems of HTS materials. This method uses the magnetic field strength vector, H , as the state variable, solving for its distribution in geometries to simulate the electromagnetic distributions within HTS. It can be intuitively easily built up in COMSOL Multiphysics, and get accurate results due to its fast convergence property. However, it is usually time-consuming to get results as the H-formulation requires the solution of a vector field in non-conducting regions causing the linear matrix size expansion, thus increasing the complexity of computation.

In real cases, there are usually a large number of turns in an HTS coil, making it very complicated and time-consuming to use these introduced methods, especially in 3D cases. Considering modelling reliability, the general 2D H-formulation and 2D H-symmetrical method are presented for solving HTS coil problems.

The 2D H-formulation is a numerical simulation method based on the finite element method (FEM), widely applied in the electromagnetic analysis of high-temperature superconductors (HTS). This formula is particularly suitable for analysing electromagnetic field problems of HTS materials in a 2D plane, especially when the geometric configuration is simple or symmetric, such as individual superconducting tapes, coils and small-scale superconducting devices. Compared to the typical 3D H-formulation, by only considering the electromagnetic field distribution within a 2D plane, the computational efficiency is higher. Hence it is suitable for rapid simulation and analysis. Additionally, the model's structure is relatively simple, facilitating easy implementation and understanding. Regarding[95], 2D is used to simulate the magnetic field distribution and AC losses in HTS tapes carrying AC current. The results showed that the 2D H-formulation is sufficient to simulate the critical state and electromagnetic behaviour of HTS tapes. The study in [109] also validates its applicability to 2D electromagnetic field problems. Overall, the 2D H-formulation plays an essential role in the two-dimensional electromagnetic analysis of HTS systems, showing outstanding performance in rapid simulation and analysis.

The 2D H-symmetrical method extends the conventional 2D H-formulation by considering symmetry conditions to further enhance computational efficiency and accuracy. By applying symmetrical conditions, it is capable of capturing detailed electromagnetic behaviour within the symmetrical regions while maintaining computational efficiency. By focusing on a smaller computational domain, it becomes feasible to use finer mesh discretization, leading to more accurate solutions. Regarding the study in[110], this approach is particularly useful for analysing HTS electromagnetic properties where symmetrical geometries and boundary conditions are present. According to [111] and[95], this approach can provide accurate predictions of the magnetic field distribution and AC losses in the tapes, and effectively capture the critical current and magnetic field interactions within the coils. Therefore, this method is especially suitable for cylindrical or rectangular geometries commonly found in superconducting tapes and coils.

3.3.2 Improved numerical modelling adapted to large scale HTS

The simulation methodologies mentioned above are sufficient to analyse the electromagnetic properties of HTS materials. However, in real cases, the application of HTS machines focused in this research, for instance, requires HTS coils as magnets in a rotor and armature windings in a stator. In these situations, a lot of HTS conductors (tapes) are needed. In addition, as in the electrical machine situation, electromagnetic analysis compounds the HTS material area and other machine areas like back iron or armature slots. Thus the methods previously introduced are too time-consuming to be applied to the modelling. Considering electrical machines, to achieve sufficient modelling, first of all, the models are degraded into 2D models, hence the whole machine geometry is replaced by its cross section area. By ignoring the length of the machine, all machine components including HTS coils are modelled by their cross section.

Meanwhile, the machine area is decoupled into the HTS area and non-HTS area. The HTS area is modelled using methods that are more adaptive to a non-linear E-J power law like the H-formulation. The non-HTS area, however, is modelled using methods that are commonly adopted for conventional electrical machines like the A-formulation.

As introduced in[112], an H-A formulation can be used to simulate an electric machine under rotating conditions with HTS windings. When simulating the HTS, considering electromagnetic analysis, the H-formulation is more reliable than general the A-formulation as it considers a non-linear E-J power law. The A-formulation is sufficient for all the other conventional

electrical machine components. Hence, in an H-A formulation, the H-formulation is in charge of the HTS domain while the A-formulation is in charge of all other electrical machine domains.

Another similar modelling method called T-A formulation is proposed[98, 113-117]. It is a 2D numerical model that is widely used for complex geometries such as large-scale superconducting coil simulations. This method employs a combination of the current vector potential, T, in the HTS domain and the magnetic vector potential, A, for the whole model, allowing for efficient modelling of the current distribution and magnetic fields in superconducting materials.

The T-A formulation is particularly beneficial for addressing the high aspect ratio of HTS conductors and reducing the complexity of the mesh required for simulations. By treating HTS tapes as infinitely thin lines, the T-A method simplifies the computational process while maintaining accuracy in predicting AC losses and other critical electromagnetic properties[113]. This FEM method is easily implemented into commercial software such as COMSOL Multiphysics.

In the study conducted by[113], the T-A formulation was applied to a 2D model of a synchronous motor to evaluate AC losses. The results showed good agreement with previously validated methods. Additionally, the study also highlighted after considering the anisotropy of the critical current density, further enhancing the accuracy of the simulations using the T-A formulation is further enhanced.

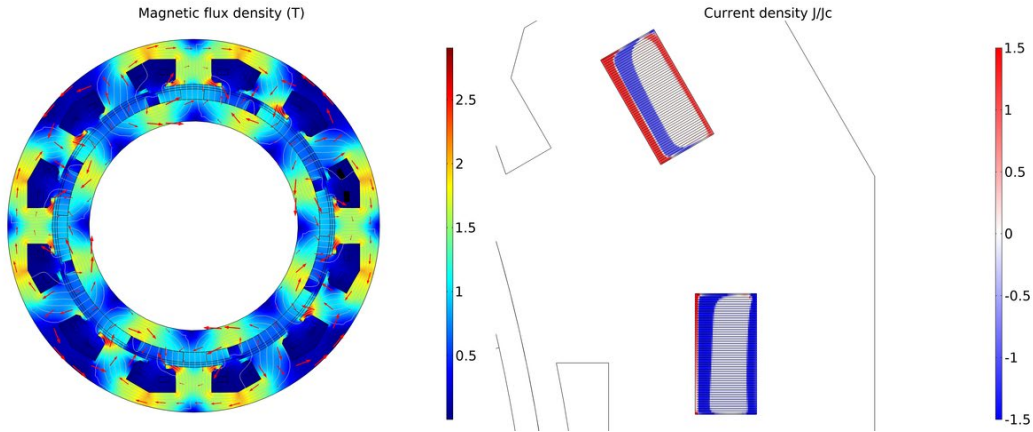


Figure 3.1 2D HTS machine modelling geometry example using T-A formulation [118]

The T-A homogenized method extends the basic T-A formulation by averaging the electromagnetic properties over multiple superconducting layers, effectively simplifying the

analysis of composite superconductors. This approach is particularly useful for large-scale applications where detailed modelling of every individual layer would be computationally prohibitive. By homogenizing the properties, the method provides a practical balance between computational efficiency and model accuracy[95].

There are also some recently proposed modelling methodologies for some special HTS coils using multi-filament structures. The multi-filament structures can be categorized into two types according to the winding methods: multiple tapes coupled at the tape ends, and multiple tapes fully coupled. As shown in the figure, the term coupled-at-ends means that the tapes connected in parallel are electrically connected at tape ends only but are insulated from each other in all other places, while the fully coupled case refers to the structure where all the tapes connected in parallel are electrically connected everywhere.

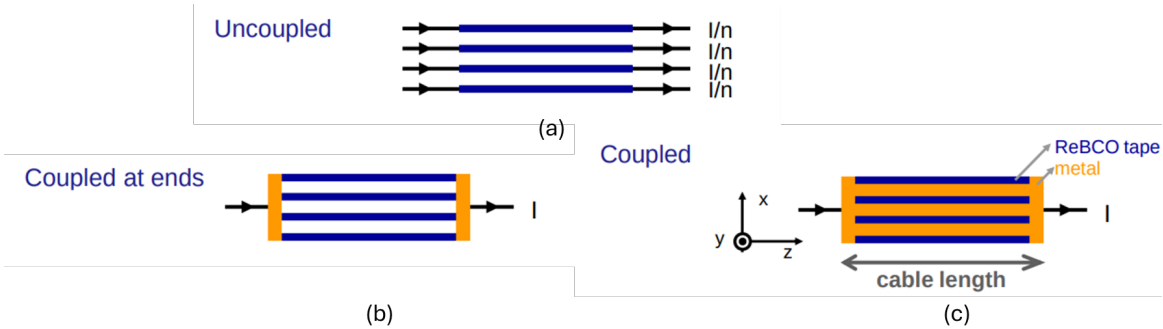


Figure 3.2 Coil structure in 2D view [74] a) uncoupled insulated tape case; b) partially coupled case; and c) fully coupled case

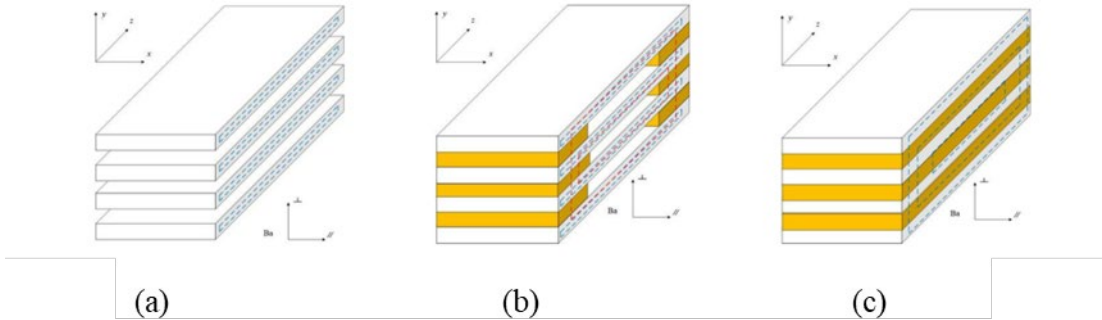


Figure 3.3 Coil (stack) structure in 3D view a) insulated tape case; b) partially coupled case; and c) fully coupled case [119]

The T-A formulation is capable of handling different coupling scenarios between superconducting tapes. In the following section, different methods using the T-A formulation are explained to handle different coupling scenarios.

The 2D T-A Neumann method is a refined numerical modelling technique used in the simulation of HTS. Similar to the conventional 2D T-A method, this approach employs the current vector potential, T , and the magnetic vector potential, A , as state variables, but with an emphasis on applying Neumann boundary conditions to enhance the accuracy and efficiency of the simulations.

The Neumann boundary condition, which specifies the derivative of a function on a boundary, is particularly useful in scenarios where the exact values of the variables are not known, but their rates of change are. In the context of HTS modelling, this allows for more accurate simulations of the magnetic field and current distributions, especially in complex geometries where the boundaries are not well-defined or are irregular.

In the 2D T-A Neumann method, the boundary conditions are set such that the normal derivative of the magnetic vector potential A is zero at the boundaries. This reflects a realistic scenario where the magnetic field lines are parallel to the boundary, ensuring that the field does not artificially diverge or converge at the edges of the computational domain. This is particularly important in HTS applications where edge effects can significantly impact the overall performance and loss characteristics of the material.

A study by Grilli et al. [113] demonstrated the effectiveness of the 2D T-A Neumann method in modelling the AC losses in HTS tapes and coils. The application of Neumann boundary conditions allowed for more accurate predictions of the magnetic field distribution and current density, leading to better correlation with experimental results. This approach was particularly useful in reducing computational errors at the boundaries, which are common in conventional methods that use Dirichlet boundary conditions.

Further research by [95] explored the use of Neumann boundary conditions in the T-A formulation for HTS coils with complex geometries. They found that this method provided superior accuracy in simulating the magnetic behaviour near the boundaries of the coils, resulting in more reliable predictions of AC losses. This was especially critical in high-

performance applications where precise modelling of edge effects and boundary interactions is essential.

As presented in [120], with special Dirichlet boundary conditions, the T-A formulation could couple an external electric circuit to determine the voltage drop as well as the current flowing through each tape. The only difference between two cases is that there will be one extra voltage constraint for fully coupled case. This is because the fully coupled case is electrically connected everywhere, thus the voltage drop per unit length for each tape should be kept the same. This is well explained in Figure 3.4. The distinctions between uncoupled (insulated tape), coupled-at-ends, and fully coupled tape configurations are crucial as they impact the distribution of current density and the resultant AC losses within the HTS system. Studies have shown that the uncoupled configuration generally results in the lowest AC losses, while fully coupled tapes can lead to significantly higher losses due to current saturation [120].

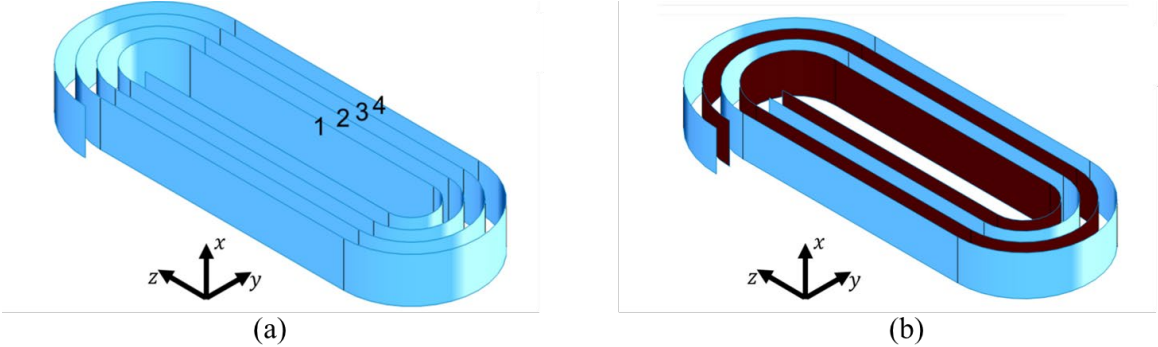


Figure 3.4 Racetrack coil 4 turns structure a) all connected in series; and b) connected in parallel as 2 branches [120]

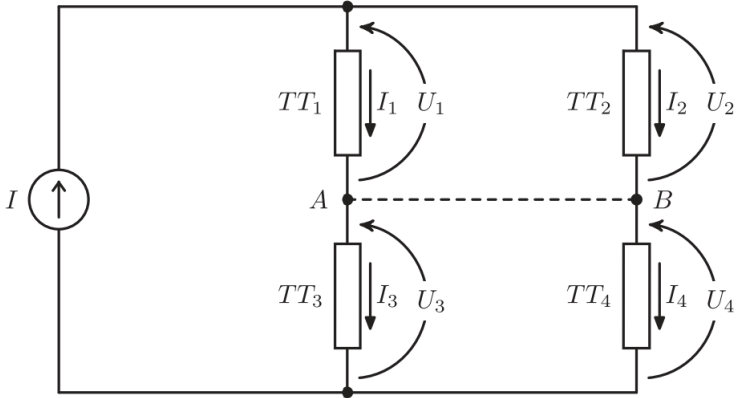


Figure 3.5 T-A coupled electrical circuit [120]

3.3.3 Implementation of critical current dependency in numerical modelling

HTS materials show anisotropy in their critical current density because of their layered crystal structure. The critical current density, J_c , is higher or the superconducting properties are better for the wider tape surface (i.e. Cu-O planes) than the narrow surface because of the intrinsic pinning associated with the Cu-O planes and the higher upper critical field[90, 91]. The critical current density, J_c , also shows external field dependency. The field dependence could be explained with the help of Figure 3.6.

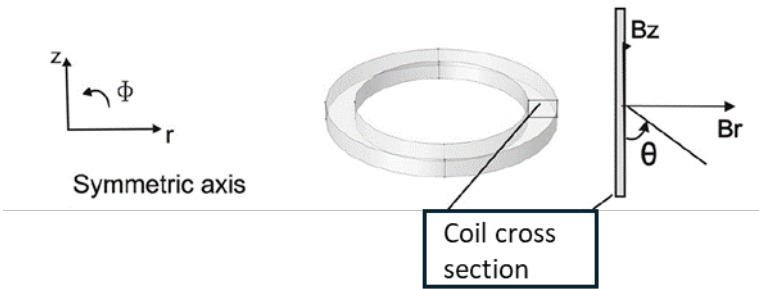


Figure 3.6 HTS tape critical current dependence on external magnetic field

The critical current is dependent on the magnetic field amplitude and the direction to the wider tape surface. The higher the field, the lower the J_c . As for the field direction, as indicated in Figure 3.7b, there is an angle function, $J_c(\theta)$, of field dependence. In cylindrical coordinates, if the tape width is placed along the z-direction, then the field direction is aligned with respect to the tape varying from 0 to 180 degrees (negative z-axis towards positive z-axis). $J_c(\theta)$ achieves the minimal value if the field is 90 degrees (along the r-direction) and achieves the maximal value if the field is parallel to the wider tape surface (along the z-direction).

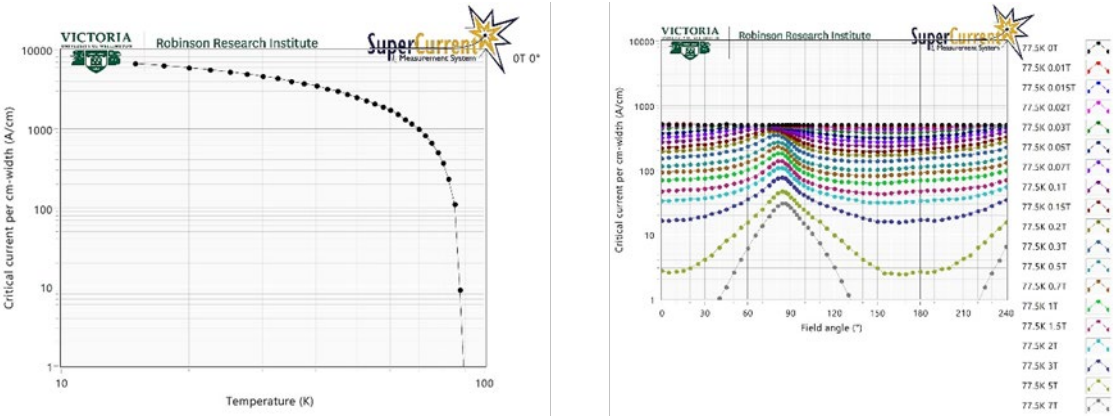


Figure 3.7 An example of the critical current characteristic of SuperOx tape a) temperature dependency; and b) angle dependency at 77 K

The critical current density dependence on the magnetic field can be summarized by the following equation[117, 121]:

$$J_c(B) = \frac{J_{c0}}{\left(1 + \sqrt{\frac{(kB_{\parallel})^2 + B_{\perp}^2}{B_c}}\right)^b} \quad (3.10)$$

where B_{\parallel} and B_{\perp} are the parallel and perpendicular components of the magnetic flux density with respect to the tape. Assuming a typical HTS 4 mm tape having the self-field critical current of 160 A at 77 K, then the parameters J_{c0} , k , B_c and b have the respective values of 49 GA/m², 0.275, 32.5 mT and 0.6.

Considering the critical current temperature dependence, a parameter named lift factor is defined by the equation below[117, 122]:

$$L = \frac{J_c(\mathbf{B}, T)}{J_c(77K)} = \frac{L_0(T)}{\left(1 + \sqrt{\frac{(k(T)B_{\parallel})^2 + B_{\perp}^2}{B_{c0}(T)}}\right)^{b(T)}} \quad (3.11)$$

In this equation, $J_c(\mathbf{B}, T)$ is the critical current density function of a given temperature and magnetic field, L , is the defined lift factor and all the other parameters that express temperature dependence are given in Table 3.2.

Table 3.2 Lift factor parameters for critical current calculation at different working temperatures with respect to 77 K

T(K)	L_0	K	B_{c0}	b
30	6.12	0.07	3.23	1.41
40	5.29	0.10	1.86	1.12
50	4.12	0.17	1.26	0.96
65	2.44	0.61	0.59	0.77

All the lift factor parameters are decided regarding the working temperature, and the lift factor is defined by the ratio between the target temperature and 77 K. An example of critical current dependence data is plotted here:

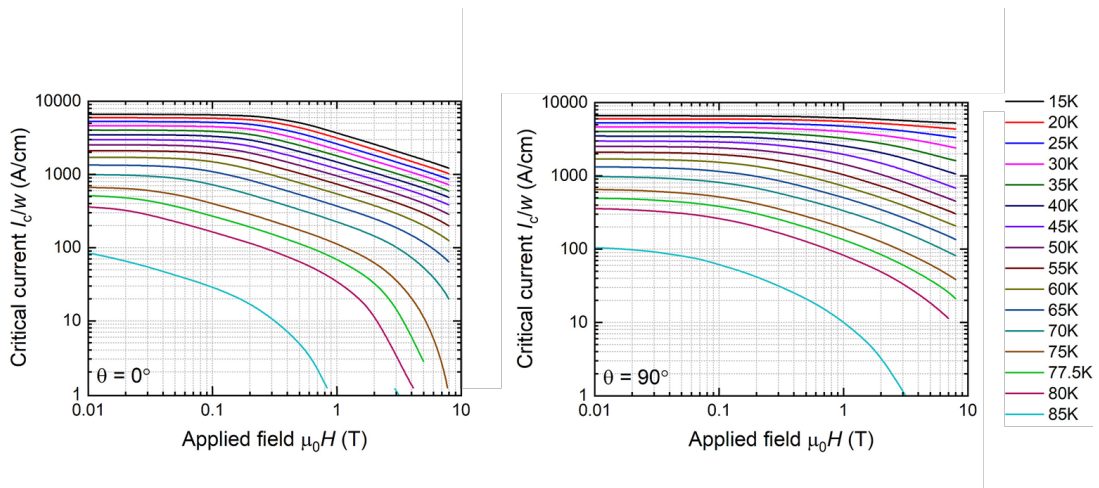


Figure 3.8 An example of the critical current field dependency of SuperOx tape a) field perpendicular to tape wider surface; and b) field parallel to tape wider surface

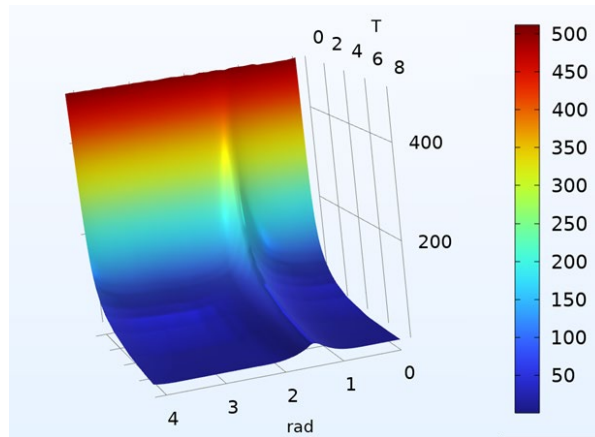


Figure 3.9 An example of the 3D critical current characteristic of SuperOx tape at 77 K

3.4 Experiment methodology for modelling validation

Experimental measurement of AC losses is essential for validating numerical models and understanding the real-world performance of HTS. The primary experimental techniques include the electrical method and the calorimetric method.

3.4.1 Electrical methodology

The electrical method is a widely used technique for measuring AC losses in HTS materials. This method involves direct electrical measurements of the superconductor's voltage and current responses to alternating currents, giving the AC loss produced by HTS materials to thus evaluate the performance of superconducting devices.

The electrical method [109, 123] typically measures the voltage drop across the superconductor as an alternating current (AC) passes through it. This method often uses sensitive voltmeters and current sources to ensure precise measurements. To enhance signal detection and accuracy, the setup may also include additional components such as current transformers, filters, and amplifiers[73].

The overall transport AC loss measurement testing circuit diagram is shown in Figure 3.10. The HTS coil is treated as an inductance, L_{sc} , in series with a resistance, R_{sc} . The mutual inductance of the compensation coil is set to cancel the L_{sc} by adjusting the position of the secondary side of the compensation coil. Therefore, only resistive voltage is left to measure in the circuit and the coil AC loss can be calculated by:

$$Q_{elec} = \frac{V_{rms} * I_{rms}}{f} \text{ (J/cycle)} \quad (3.12)$$

where f is the frequency of the applied current, I_{rms} is the root-mean-square (rms) value of the transport current applied to the coil and V_{rms} is the rms value of the voltage component that is in phase with the I_{rms} after compensation coil correction.

Alternatively, the measurement of transient voltage and current across the coil could be used to calculate the total AC loss. By averaging the integration of transient loss over n cycles, the AC loss per cycle is described by Equation 3.13. Ideally, these two calculations should be equivalent to each other.

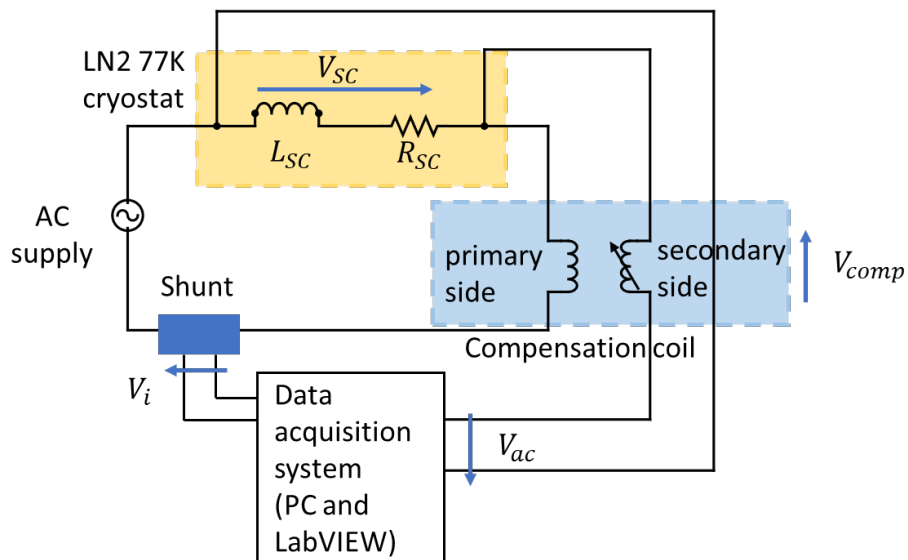


Figure 3.10 AC loss measurement setup for the electrical method

$$Q_{elec} = \frac{1}{n} \int_0^{nT} v_{ac} \times i_{app} \text{ (J/cycle)} \quad (3.13)$$

The electrical method is applicable to a variety of configurations, including single HTS tapes, multilayer superconducting cables, and more complex geometries such as racetrack coils. It is particularly valuable for characterizing AC losses in HTS materials used in power transmission cables, motors, and generators. The method works under a variety of operating conditions, including varying temperatures and magnetic fields, allowing for a comprehensive assessment of the performance of superconductors in real-world applications [99].

In study [76], the electrical method was used to measure AC losses in HTS coils placed under an external magnetic field. The results highlighted the method's ability to accurately capture the loss characteristics under different magnetic conditions, showing its applicability in the design of superconducting motors and generators. Similarly, in [99] the electrical method was used to evaluate the performance of a 1-metre-long HTS power cable, providing valuable data for improving cable design and reducing operating losses.

As the electrical method is a straightforward measurement approach, it could provide accurate and immediate results on the AC losses. This method also allows for continuous monitoring of superconductor performance under operational conditions, providing real-time data that is critical for optimizing device design and operational parameters[95].

However, the accuracy of the measurements is sensitive to noise and external electromagnetic interference. It is necessary to carefully build the setup and add shielding equipment. Furthermore, this method requires careful calibration of the measuring instrument to ensure accuracy. This method can only measure the total losses and cannot distinguish between different loss mechanisms such as hysteresis losses and eddy current losses [109].

3.4.2 Magnetic methodology

The magnetic method is used to measure the hysteresis loss of superconductors. Standard methods such as pickup coils, Superconducting Quantum Interference Devices (SQUIDs) and vibrating sample magnetometers (VSM) are usually used in magnetic measurement[124-126]. As illustrated in Figure 3.11, the measurement system usually consists of the AC magnet,

cryostat, pick-up coil, compensation coil, high-current amplifier, as well as DAQ. An optional lock-in amplifier can be used to increase signal sensitivity, especially at low signal levels. This helps isolate the magnetic signal from background noise, allowing for a more accurate determination of hysteresis losses.

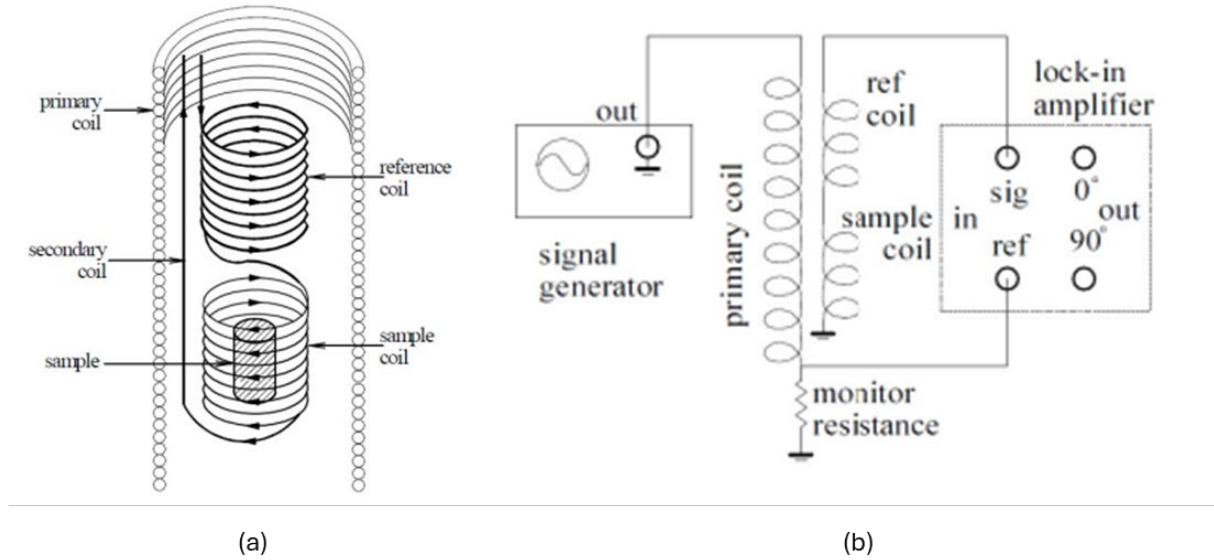


Figure 3.11 Measurement system using the magnetic method a) Layout of different coils; and b) setup equivalent circuit [124]

The hysteresis loop measurement [125] is usually achieved by measuring the voltages over pick-up coils around the superconducting specimen, then taking the integral of the multiplication of the voltages and the field strength over one cycle, so that the variation in the magnetic moment of the specimen can be identified. By integrating over the hysteresis loop, the hysteresis loss per unit length (W/m) can be calculated[125]:

$$P_h = CAf\mu_0 \oint H_e dM = -CAf\mu_0 \oint M dH_e \quad (3.14)$$

where H_e and M are the applied AC magnetic field and the magnetization, A is the geometrical cross-section of the superconductor sample, and C is the effective coefficient. $C = 1$ at low frequency.

3.4.3 Calorimetric methodology

Though the electric method can provide accurate and immediate results on the AC losses, it has some limitations. When the HTS material carrying an AC current is placed under an external AC magnetic field, it requires both the AC transport current and the external AC field to be at

the same frequency and in phase. In general, it is normal to have the applied current and external field out of phase in electrical machines. Under this condition, the calorimetric method could be an excellent alternative.

The calorimetric method is a precise technique for measuring AC losses in HTS by quantifying the heat generated during their operation. This method is particularly valuable for its ability to provide an integrated measurement of all forms of energy dissipation within the superconducting material.

The calorimetric method can be summarized as follows[73, 127, 128]. The HTS sample is placed in a cryogenic environment, typically liquid nitrogen (77 K) as an example, and then the resultant boil-off rate of the cryogen is measured as the superconductor carries an AC current and or is exposed to an AC magnetic field. The heat generated by the AC losses causes the cryogen to evaporate, and this evaporation rate is directly proportional to the energy dissipated within the superconductor. By precisely measuring the mass flow rate of the evaporated cryogen, it is possible to determine the total AC losses[73].

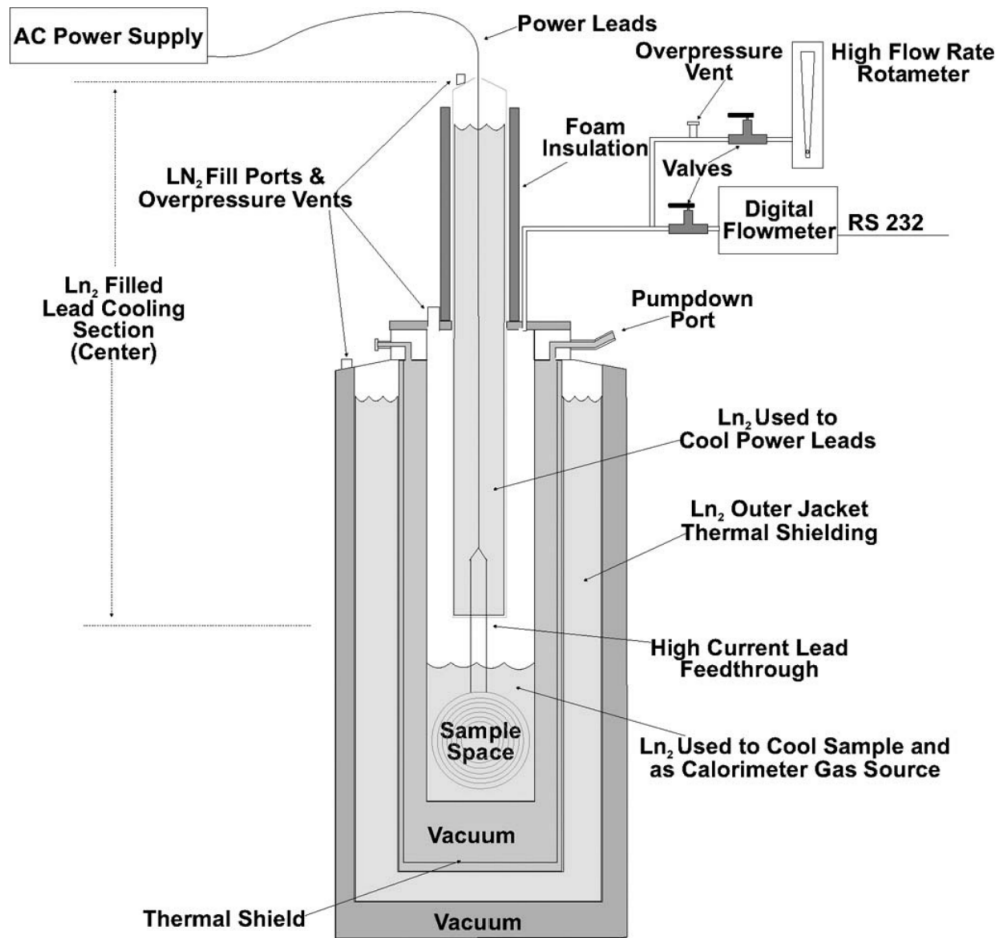


Figure 3.12 AC loss measurement setup for the calorimetric method [73]

There are two primary setups used in calorimetric measurements: self-field and external magnetic field setups. In the self-field setup, the superconductor is subjected to an AC transport current, and the resultant losses are measured based on the boil-off of the surrounding cryogen. The external magnetic field setup, on the other hand, measures the AC loss produced by both transport current and the external AC field. The superconductor carrying an AC transport current is placed in a varying magnetic field, possibly produced by a rotating magnet, and the setup measures the boil-off due to both the transport current and the external field[73].

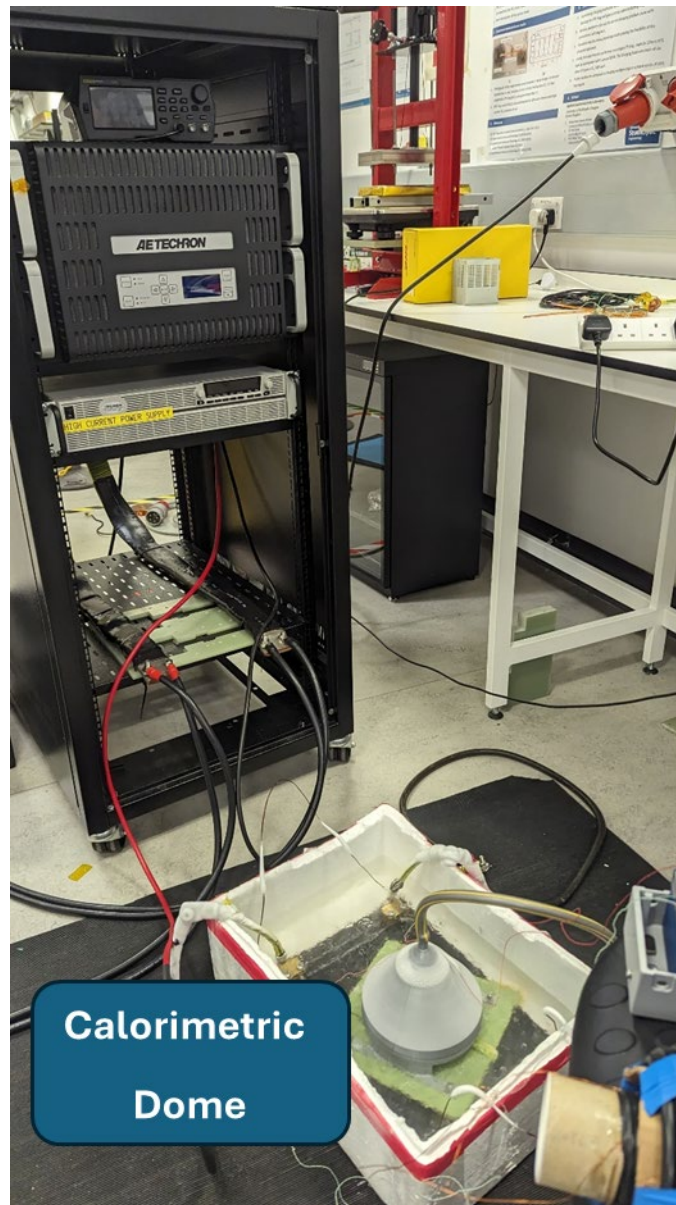


Figure 3.13 Calorimetric boil-off measurement setups in the laboratory

The calorimetric method is particularly effective for characterizing the AC losses in HTS materials used in power applications such as electrical machines in this research. Similar to the electric method, it provides comprehensive direct measurement of the total AC loss in all forms of dissipation, including resistive, hysteretic, and eddy current losses. Additionally, the calorimetric method is highly sensitive, capable of detecting even small amounts of heat generated, thus providing precise loss measurements[73].

However, the calorimetric method also has some limitations. The primary challenge is the requirement for a cryogenic environment, which adds complexity and extra cost to the

experimental setup. Additionally, accurate measurements depend on precise control and calibration of the cryogenic system, as any external heat leaks can affect the accuracy of the results. The method also requires a stable thermal environment to ensure that the measured boil-off rate is solely due to the AC losses and not influenced by external factors[120].

As indicated in[95], their research applied the calorimetric method to study the losses in HTS tapes and cables. Their research demonstrated that the calorimetric measurements closely matched theoretical predictions and electromagnetic measurements, achieving the validation of the method accuracy and reliability. Similarly, regarding[73], the calorimetric method was used to measure AC losses in HTS coils subjected to external magnetic fields. The setup included a sensitive boil-off calorimeter that could measure losses ranging from a few milliwatts to several hundred milliwatts. The results provided detailed insights into the loss characteristics under varying magnetic conditions, showing the strengths of the calorimetric method in evaluating the AC loss performance of superconducting motors and generators.

A comparison between these three AC loss measurement methods is summarized in Table 3.3.

Table 3.3 Comparison between two AC loss measurement methods [129]

Measurement method	Main purpose	Advantages	Limitations
Electrical method	Transport current loss; total AC loss	High sensitivity; high accuracy; Able to measure low AC loss	Extra compensation coil needed; Only works with pure sinusoidal signals; Easily introduces harmonics
Magnetic method	Magnetization loss	High sensitivity; high accuracy; Able to measure low AC loss	Limited to static measurement; Pick-up coils easily disturbed by the external magnetic field
Calorimetric method	Total loss	Disregarding object shape; Able to measure large scale samples	Poor sensitivity and weak accuracy for low AC loss measurement; Long time; Possible disturbance from thermal effects of non-superconductors

3.5 Numerical model validations by experiments

3.5.1 Test coil preparation and critical current determination

Initially, as shown in **Error! Reference source not found.**, a 68 turn (34 turns per layer) double pancake coil wound from SuperOx 2G YBCO tapes is made in this work. The tape width is 4 mm, and for each coil turn, the copper stabilizer around each tape is about 20 μ m thick and this coil is named an insulated coil. The coil information is given in table below.

Table 3.4 Insulated double pancake coil parameters

Parameter	Value	Unit
Inner Diameter	60	mm
Outer Diameter	85	mm
N° of layers	2	
N° of turns per layer	34	
Tape width	4	mm
Self-Field I_c	80	A(DC)
Working Temperature	77	K

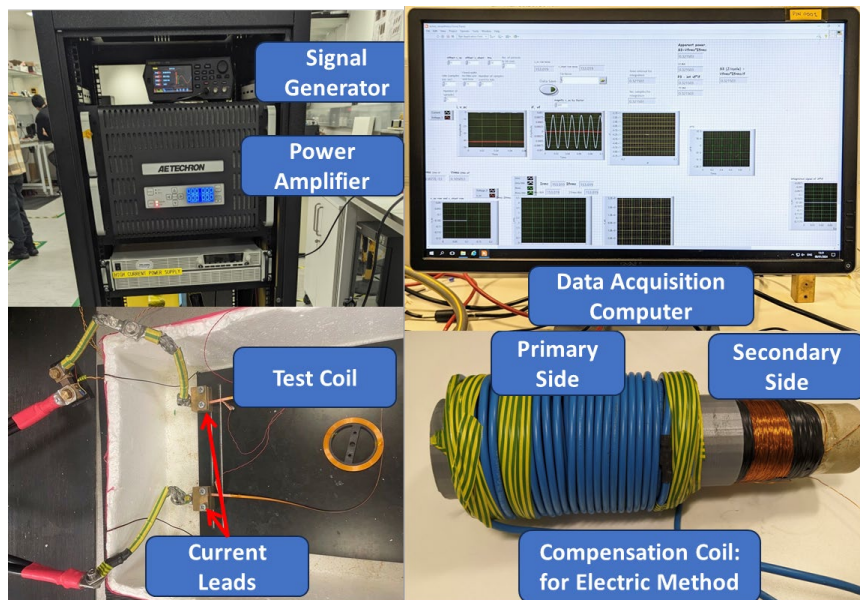


Figure 3.14 The tested insulated double pancake coil sample and its measurement setups

The coil self-field critical current, I_c , is measured under LN₂ working temperature, 77 K. As observed in the figure below, the measured I_c for this sample coil is around 80 A. This critical current is used for later simulation model calibration.

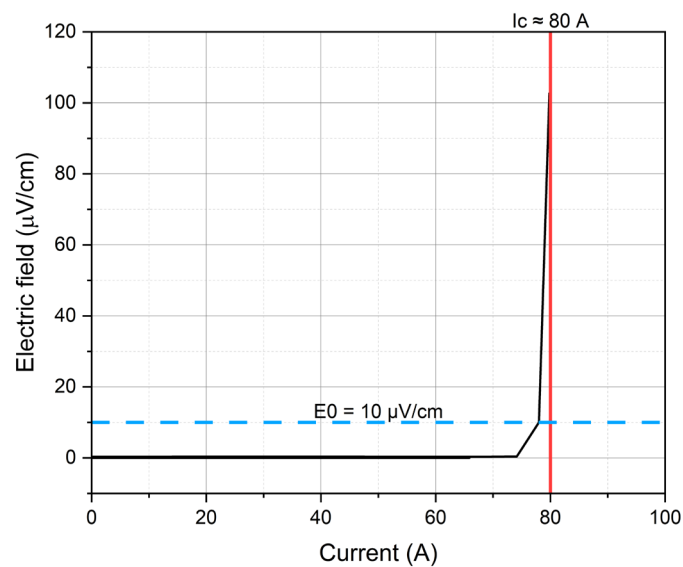


Figure 3.15 Coil self-field critical current measurement

3.5.2 AC loss measurement

The coil AC loss is measured with applied transport current only. The loss measurement is using electrical method as explained in previous chapter. Regarding its self-field critical current (80

A), the coil transport loss is measured under different currents and frequencies, respectively. The AC current applied to the coil is set to 10 A_{rms} (12.5% of I_c), 20 A_{rms} (25% of I_c), 30 A_{rms} (37.5% of I_c) and 40 A_{rms} (50% of I_c), and the maximum testing current is limited by the power supply in the lab. The coil is tested under LN₂ working temperature (77 K), and the coil transport current AC loss is measured at 50, 75 and 100 Hz, respectively. The measurement results under different frequencies are shown in logarithm scale plot in Figure 3.16. It is shown that the coil AC loss with applied current only increases as the current increases. There is no obvious frequency dependency showing here, which agrees with the hysteresis loss properties. We also noticed that, when the applied current is as small as 10 A_{rms}, the measurement results are not accurate enough since the current generated is more noisy and unstable.

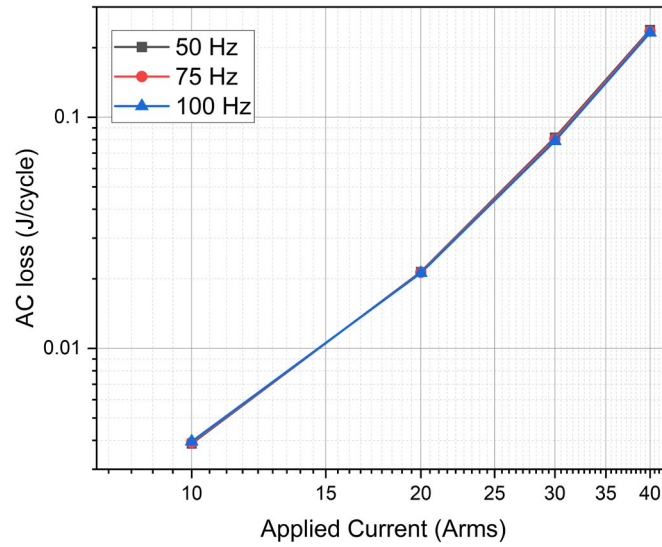


Figure 3.16 Transport current AC loss measurement under different working frequencies

3.5.3 Coil model methodologies

3.5.3.1 H-formulation: 2D axis-symmetrical model

For time-sufficient consideration as well as coil geometry, a 2D-symmetrical model is developed in this study. In 2D cylindrical geometry, the current J_θ is flowing along the θ direction, while the two magnetic field variables, $\mathbf{H} = [H_r; H_z]$ are in the r-z plane. The relationship between current and magnetic field is obtained by the original Ampère's law:

$$J_\theta = \frac{\partial H_r}{\partial z} - \frac{\partial H_z}{\partial r} \quad (3.15)$$

By substituting magnetic field and electric field variables into Faraday's law for cylindrical coordinates:

$$\begin{bmatrix} -\frac{\partial E_\phi}{\partial z} \\ \frac{1}{r} \frac{\partial(rE_\phi)}{\partial r} \end{bmatrix} = -\mu_r \mu_0 \begin{bmatrix} \frac{\partial H_r}{\partial z} \\ \frac{\partial H_z}{\partial r} \end{bmatrix} \quad (3.16)$$

A 2D axial symmetrical model using the H-formulation is applied to the model. The coil geometry is illustrated below. Regarding study[90], since most of the current is flowing into the HTS layer, it is reasonable to simplify the tape structure by modelling only the 2 μm YBCO layer while ignoring all other layers.

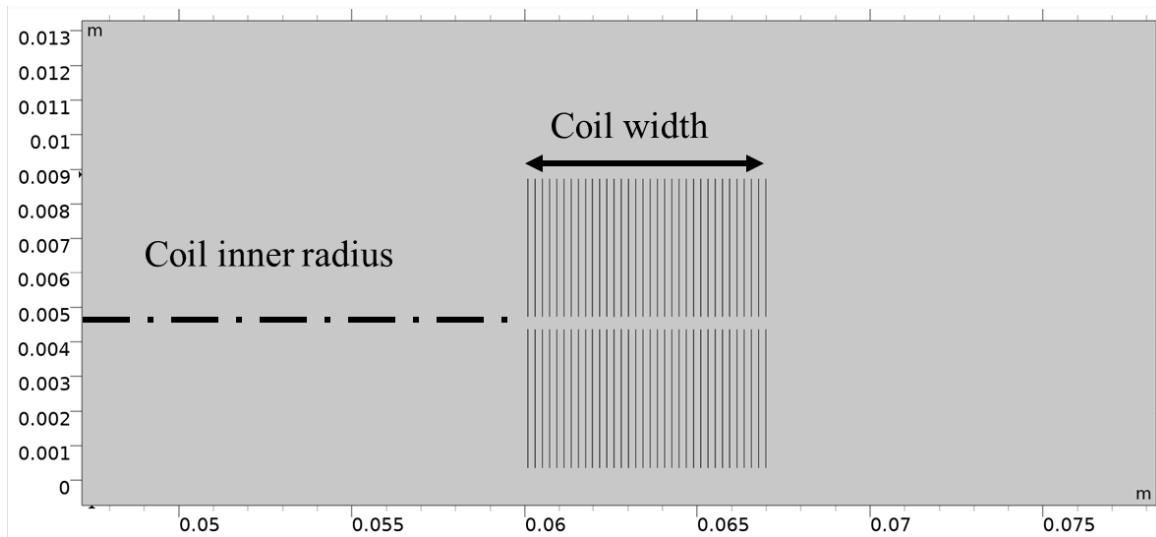


Figure 3.17 Coil model geometry in COMSOL Multiphysics

In cylindrical coordinates, the coil cross section is shown in the r - z plane with the innermost turn placed at the coil inner radius, and all other turns placed adjacently with the same spacing in between. The field angle, θ , is defined as the angle between the field and the coil (tape) width surface. The critical current decays the most when the field is perpendicular to the tape width surface.

AC current is assigned to every YBCO layer using the global constraints of COMSOL. The total current of each turn is represented by the integration of local J_ϕ in each YBCO layer. Finally, a global constraint is set for each YBCO layer to be equal to the total current, which refers to a predefined applied current.

3.5.3.2 T-A formulation: 2D axis-symmetrical model

Since this research work only focuses on HTS coils used as armature windings in a stator, it is sufficient to use 2D models. Hence, only the 2D T-A model is introduced here. A full explanation of 2D and 3D T-A formulations can be found in [98] and [68], respectively.

Considering that the thickness of superconducting tape is far smaller than the superconducting layer width, the superconducting layer is approximated as a 1D line (the thin strip approximation) for modelling stacked superconducting stacked tapes. The working process of the T-A formulation is given below.

The T-A formula approach solves two state variables separately: the current vector potential, \mathbf{T} , along the HTS tape layer, and the magnetic vector potential, \mathbf{A} , for the whole geometry. The governing equations are given:

$$\mathbf{J} = \nabla \times \mathbf{T} \quad (3.17)$$

$$\nabla \times \rho \nabla \times \mathbf{T} = -\frac{\partial \mathbf{B}}{\partial t} \quad (3.18)$$

where μ is the magnetic permeability, \mathbf{J} is the current density and ρ is the resistivity.

The use of the thin strip approximation implies that the current only flows in the tangential direction of the superconducting layer ($J_y = 0$). This transfers the 3D problem into a 2D surface problem. In 2D cartesian coordinates, with the help of assuming that the superconducting layer is infinitely long in the Z direction, the current flows only longitudinally ($J_x = 0$). As result, the calculation area becomes a 1D line. The simplified equations are given here respectively.

$$J_z = \frac{\partial(\mathbf{T} \cdot \mathbf{n}_y)}{\partial x} \quad (3.19)$$

$$-\frac{\partial}{\partial x} \rho \frac{\partial(\mathbf{T} \cdot \mathbf{n}_y)}{\partial x} = -\frac{\partial B_y}{\partial t} \quad (3.20)$$

For axial-symmetric problems in cylindrical coordinates, these equations are modified as:

$$J_\varphi = \frac{\partial(\mathbf{T} \cdot \mathbf{n}_r)}{\partial z} \quad (3.21)$$

$$-\frac{\partial}{\partial z} \rho \frac{\partial(\mathbf{T} \cdot \mathbf{n}_r)}{\partial z} = -\frac{\partial B_r}{\partial t} \quad (3.22)$$

where the current potential B_y can be found through following A formulations:

$$\nabla \times \nabla \times \mathbf{A} = \mu \mathbf{J} \quad (3.23)$$

$$\mathbf{B} = \nabla \times \mathbf{A} \quad (3.24)$$

The boundary conditions can be found when applying a transport current to the coil terminals:

$$I = \iint_S \mathbf{J} dS = \iint_S \nabla \times \mathbf{T} dS = \oint_L \mathbf{T} dS \quad (3.25)$$

where S is the conductor cross section, and L is the boundary cross edges of S.

Since \mathbf{T} has only one component which is perpendicular to the conductor surface,

$$I = (T_1 - T_2) \cdot d \quad (3.26)$$

Meanwhile, for air, ρ is set to 1000 Ωm and for HTS tape, ρ is obtained through the E-J power law:

$$E_z = \rho J_z = E_0 \left(\frac{J_z}{J_c} \right) \left(\frac{|J_z|}{J_c} \right)^{(n-1)} \quad (3.27)$$

where E_0 is 100 $\mu\text{V/m}$, n value is 31 in this study, and J_c is the critical current.

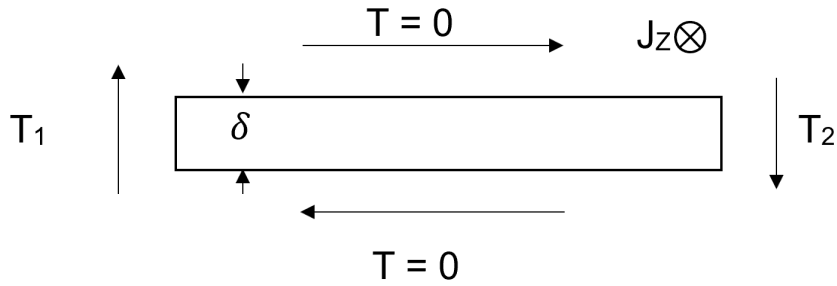


Figure 3.18 Explanation of T-A formulation

Considering the anisotropic characteristics of 2G tapes, the E-J power law is rearranged:

$$E_z = \rho J_z = E_0 \left(\frac{J_z}{J_c(B)} \right) \left(\frac{|J_z|}{J_c(B)} \right)^{(n-1)} \quad (3.28)$$

where variable $J_c(B)$ implies the influence of the external field on tape critical current density and can be described by:

$$J_c(B) = J_{c0} \times \{P1(B) + [P2(B) - P1(B)] \times G(\theta)\} \quad (3.29)$$

where J_{c0} is the self-field critical current density, $P1(B)$ is the perpendicular field J_c dependency, $P2(B)$ is the parallel field J_c dependency, and G is the normalized angle dependency[90].

3.5.4 Coil self-field critical current calibration

The coil self-field critical current calibration in the model can be summarized in the following process. First, the critical current J_{c0} of the tape used for this coil is set regarding the tape datasheet. Then the normalized self-field critical current dependence of the applied external field, $J_{cB}(\theta, B)$ is implemented in the HTS domain in the form of interpolation. A mapping data of J_{cB} in the function of external field angle respect to the tape width surface, θ and the norm field value, $J_{cB}(\theta, B)$, is used to quantify the YBCO tape critical current density field dependency. The 3D plot of the specific mapping data used for this insulated coil is given below.

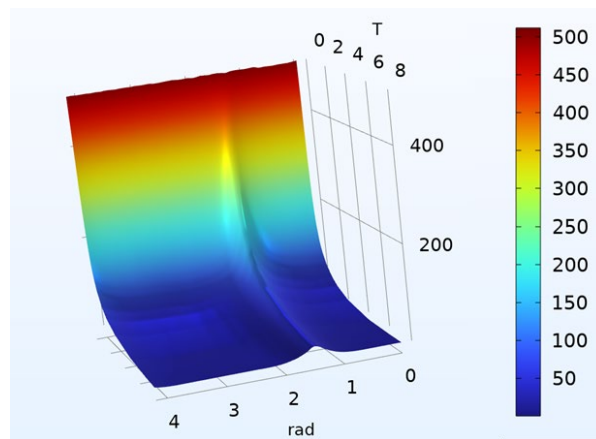


Figure 3.19 The 3D plot of the $J_{cB}(\theta, B)$ mapping data for this specific insulated coil

In the model, a ramping up DC current is applied to the HTS coil. The coil self-field current is the cross point of applied DC current and $J_{cB}(\theta, B)$. Since the coil critical current is influenced by the number of coil turns and the coil dimensions, this empirical interpolation function is not a perfect match for the real test coil properties. The coil self-field critical current in the simulation will be slightly different from that of real measurements. By modifying the tape J_{c0} , the coil self-field critical current in the simulation will finally match the measurement result.

As the current penetrates from the coil edges, the highest current that can be sustained in the coil is limited by the innermost turn where the field generated by the coil itself reaches its highest value. Therefore, the I_c calibration can be achieved by comparing the I_{cB} and the applied current, I_{app} , of the innermost turn. As a ramping up DC current is applied to the coil, two probes help to visualize the innermost turn two currents: I_{cB} and I_{app} . The critical current of the coil is the cross point between these two currents. Finally, a calibration of the coil self-field critical current is achieved. The coil self-field critical current calibration plot is shown in Figure 3.20.

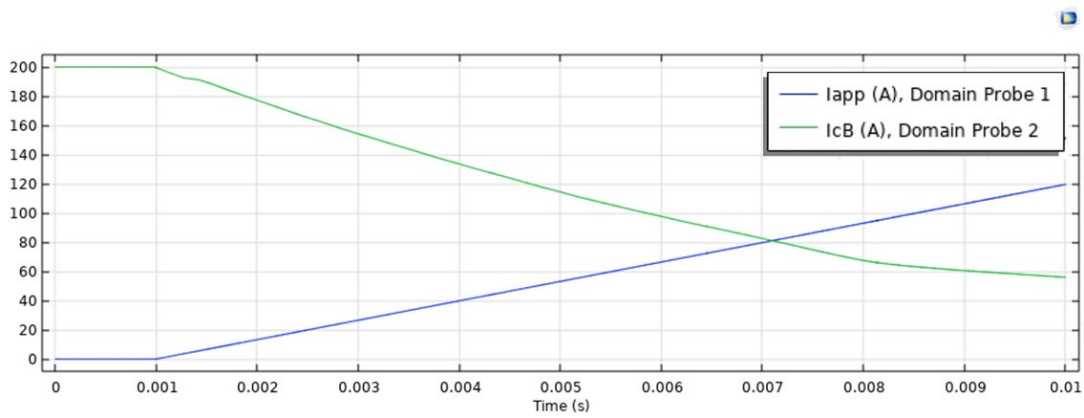


Figure 3.20 The tested insulated coil self-field critical current calibration in COMSOL Multiphysics

3.5.5 AC loss validation

Once the critical current in simulation is calibrated, the transport current loss can be calculated in the simulation. As seen in the coil geometry in Figure 3.17, the surrounding air domain (grey area) is assumed to be large enough that the field generated by the coil current decays to zero at the air domain boundaries.

Figure 3.21 shows the transport current loss comparison between the 2D axial-symmetrical simulation and measurements taken at 50 Hz and 100 Hz. It shows good consistency. The obvious difference occurs at the 10 A_{rms} point. There are two main reasons to be considered here: first, as mentioned before, measurement of the low current range has an unstable input signal, which makes the measurement not accurate enough; meanwhile only the HTS layer is simulated, and the ignorance of other layers will reduce the total AC loss. In the end, the 2D axial symmetrical model using the H-formulation is validated and can be used for coil transport current AC loss analysis. This is the first step of analysing the AC loss for HTS armature design. In addition, the T-A 2D axial-symmetrical simulation is also validated with respect to the H-formulation as given in Figure 3.22. Since this is the validation between models, the validation range of both frequency and current are increased: from 25 Hz to 100 Hz and 10 A_{rms} to 60 A_{rms} , respectively. It also shows good consistency. The T-A formulation will be used for large scale stator coil AC loss analysis under a real machine environment in Chapter 6.

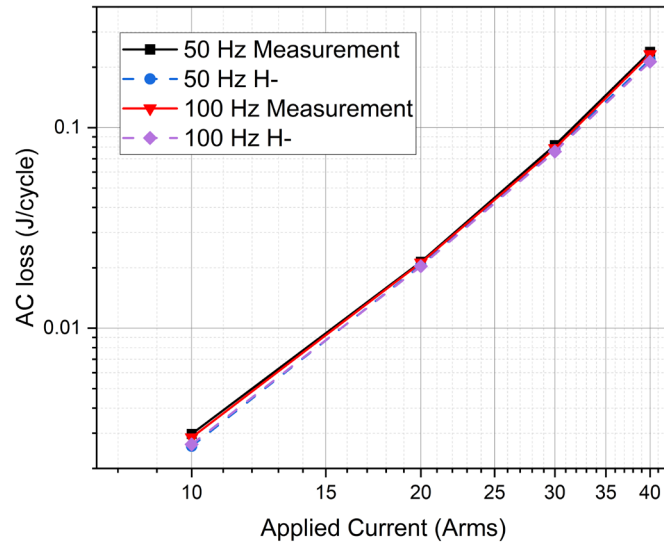


Figure 3.21 Transport current AC loss H-formulation simulation validation

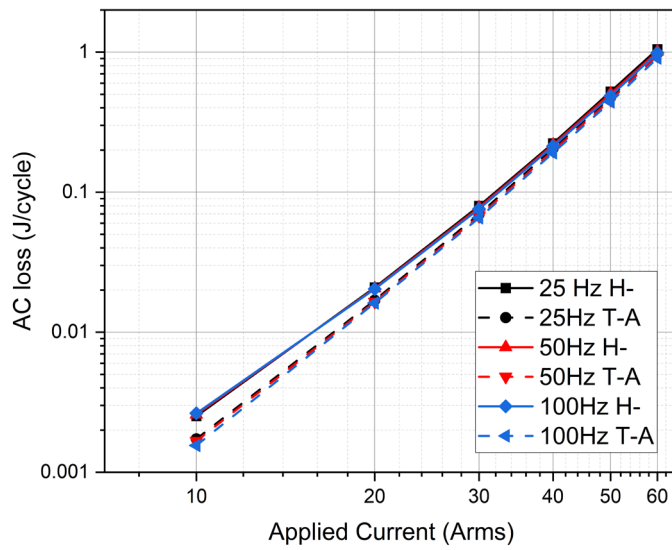


Figure 3.22 Transport current AC loss T-A simulation validation

3.6 Conclusion

Compared to LTS, HTS materials have higher critical temperatures and are more stability to thermal perturbations. However, when subjected to an AC current or a time-varying external magnetic field, HTS materials develop AC losses, which are crucial in determining their performance efficiency and thermal management. Therefore, the assessment of AC losses in HTS materials is a comprehensive and critical aspect of their application in various technologies, especially in large-scale power applications and medical devices. This chapter looks at the different methods used to evaluate AC losses in HTS materials.

This chapter first reviews the assessment of AC losses performed by numerical modelling using FEM. This chapter provides a comprehensive overview of various numerical modelling methods, including the widely used H-formula and the efficient T-A formula, and highlights their advantages and disadvantages. It also reviews the state-of-the-art modelling methods for AC loss evaluation of different HTS coil structures.

Experimental loss measurements are then introduced as experimental measurements are essential to understanding the actual performance of HTS and to validate numerical models. The main experimental techniques include the electrical, magnetic and calorimetric methods. This chapter reviews these three measurement methodologies, including their respective advantages and limitations. The electrical method involves directly measuring the voltage and current response of a superconductor to an AC current to assess the AC losses. It provides accurate and immediate results and is valid under a wide range of operating conditions. However, it is sensitive to noise and electromagnetic interference, and requires careful setup and calibration. The magnetic method for hysteresis loss measurement is achieved by integrating the signals from pick-up coils around the superconductor samples. Similar to the electric method, it is sensitive and the pickup coil is easily disturbed by the external magnetic field. The calorimetric method measures AC losses by quantifying the heat generated during operation, using the evaporation rate of a refrigerant in a controlled environment. This method is particularly effective for characterizing total AC losses, including resistance, hysteresis, and eddy current losses. Although it has high sensitivity and accuracy, it requires a cryogenic environment, increasing the complexity and cost of the setup.

Finally, a testing coil is proposed, and its transport current AC loss is measured at three different frequencies (25, 50 and 100 Hz) to help validate the numerical modelling used in the following

research work. The results indicate that H- and T-A formulations perform well on HTS coil AC loss evaluation.

Evaluating AC losses in HTS is a key factor in the development and application of superconducting technologies. Having accurate numerical and experimental methods to measure them is essential for mitigating total HTS AC loss.

Chapter 4 The radial flux HTS synchronous motor topology comparison for electrified aircraft applications

4.1 Introduction

As indicated in previous chapters, it is known that HTS machines have great potential in electric propulsion applications due to their high current capacity under cryogenic temperature. Radial flux motor topologies are commonly considered in high power level motor applications, as they have higher centrifugal force tolerance compared to an axial flux motor structure. To achieve the ambitious targets of PTW for electrified aircraft [15, 18], it is important to determine suitable motor topologies. Considering the main component of losses comes from the stator part, it is therefore crucial to determine the stator design.

This study compares the radial flux synchronous motor topology of different HTS motors for aviation applications, evaluating the performance of slotless stator designs, highlighting the impact of different stator winding technologies, and the specific benefits of HTS stator coils. The comparison focuses on the machine PTW performance and the stator AC loss. First of all, regarding magnetic loading limits, two motor benchmarks rated at 450 kW with permanent magnet rotor and 1 MW with HTS magnet rotor are proposed, respectively. The purpose behind analysing two different designs is that it is necessary to evaluate the potential of using HTS coils as armatures for both partially HTS motors with permanent magnet rotors as well as fully HTS motor environments with higher rotating fields. The iron teeth impact on the machine performance is analysed to explore the features of the slotless stator design. In the following part, the HTS stator coil is compared to the copper and aluminium Litz structure coils [130, 131] under cryogenic temperatures to investigate the strengths of the HTS stator design. Before the analysis, the benchmark developments are also explained.

4.2 Radial flux motor in electrified aviation

The drive towards high-power density motors has led to increased interest in radial flux machines for aviation. Though the axial flux motor is desirable because of its compact structure thus high PTW, this design suffers from a big mechanical challenge[132]. Generally, a motor achieves high power density by increasing its rotation speed as fast as mechanically possible. Axial flux motor speed is usually limited by the centrifugal force acting on the rotor which tries to pull it apart. Hence, for high power motor design (such as MW level) in electrified applications, radial flux motors with smaller diameters are preferred due to the lower centrifugal force.

The integration of HTS technology into radial flux motors marks a significant step forward in aviation propulsion. Traditional copper and aluminium motors face limitations in power density and efficiency at cryogenic temperatures. By leveraging HTS materials in the stator and rotor, motor performance can be dramatically improved. HTS rotors, in particular, can achieve magnetic flux densities of 1–2 T, compared to the 0.5–0.7 T typically seen in permanent magnet rotors.

For aircraft, power-to-weight ratio (PTW) is a crucial performance metric. HTS radial flux motors can enhance PTW by reducing losses and increasing current density. For instance, aluminium Litz wire, used in some designs, can achieve 30 A/mm² at cryogenic temperatures, offering lightweight and efficient alternatives to copper wires. HTS armature windings provide even greater current-carrying capacity and lower losses at temperatures below 77 K, making them ideal for high-power aviation applications.

4.2.1 Two power level motor benchmarks

As indicated in[25, 133], to achieve ideal electrical loading for HTS motors, the magnetic loading could be kept under 1 T, which is achievable for both permanent magnet rotors and HTS magnet rotors. Two benchmarks are used for comparison in this study: a 450 kW motor with permanent magnet rotor operating at 77 K, and a 1 MW motor with HTS magnet rotor at 77 K and 40 K. These benchmarks allow the exploration of different stator winding choices and their performance at various temperatures. The detailed benchmark parameters are given in Table 4.1.

Table 4.1 Motor benchmark parameters

Benchmark	450 kW		1 MW	
Parameter	value	unit	value	unit
Output power	450	kW	1	MW
Input phase voltage	170	Vrms	400	Vrms
Pole pair number	6		6	
Mean airgap radius	0.195	m	0.5	m
Stack length	65	mm	100	mm
Rated speed	5000	rpm	5000	rpm
Frequency	500	Hz	500	Hz
Airgap magnetic loading	0.68	T	1	T
Stator working temperature	77	K	77, 40	K

Both motors are designed to operate at a rated speed of 5000 rpm, with an airgap magnetic loading of 0.68 T for 450 KW design and 1 T for 1 MW design. These benchmarks allow for a meaningful comparison between copper/aluminium Litz wire stators and HTS stator coils in terms of power density and losses.

4.3 Motor topology determinations

In general, the motor components can be divided into two main categories, which are active components such as rotor magnets and stator windings and inactive components like the stator core structure. The machine PTW is determined by both types of components. In this study, motor topology determination is mainly focused on the stator part. In this section, the impact of the iron core as well as different types of stator windings on the motor overall loss and the PTW is analysed.

4.3.1 Slotless stator design

First of all, the iron core always adds extra weight, which is not desirable for a high PTW requirement motor design. In addition, this structure produces extra loss. For cryogenic motors, an iron core can introduce additional challenges due to increased hysteresis and eddy current losses. At cryogenic temperatures, iron suffers same amount of hysteresis loss as at room temperature, however, iron experiences 10–20% higher eddy current losses [134] compared to room temperature due to increased conductivity. For example, in the 450 kW motor benchmark, this results in 1.5 kW of additional cooling power required, 3–5 kg extra weight, and in the 1 MW motor benchmark, this increases to 3 kW of cooling power and 8–12 kg extra weight. These results make slotless structures more desirable for high PTW cryogenic motor designs.

4.3.2 Stator winding comparison

Before the AC loss evaluation of real HTS armature coils, a case study of different armature winding comparison is proposed. The purpose of this study is to investigate the potential value of using HTS armature winding compared to conventional armature winding types.

4.3.2.1 Analytical AC loss calculations: Litz wire winding

Litz wire, a multi-filament wire made of fine, insulated and twisted strands can be used in cryogenic temperature to improve the power density of electrical machines by increasing their current capacity. For instance, it is proved that the current density could achieve as high as 30 A_{peak}/mm² [130] at 77 K. However, the eddy current loss could be a serious problem due to the low resistivity and high magnetic field. The total loss in a Litz wire coil is summarized in:

$$P_{tot} = P_{rms} + P_{skin} + P_{prox} \quad (4.1)$$

where P_{rms} is the coil resistive loss due to transport current, which is independent from the operating frequency, P_{skin} is the skin effect loss and the internal proximity loss (caused by surrounding strands) and P_{prox} indicates the external proximity loss caused by the external field. Considering a Litz wire structure of N strands under a background field strength H , the total AC loss [130] could be described in:

$$P_{tot} = \frac{R_{dc} \hat{I}^2}{2} + \frac{R_{dc} \hat{I}^2}{2} \left(\frac{N(N-1)}{8} \left(\frac{r_s}{r_L} \right)^2 \left(\frac{r_s}{\delta} \right)^4 \right) + \frac{N}{8} \omega^2 (\mu \hat{H})^2 \sigma \pi r_s^4 \quad (W/m) \quad (4.2)$$

The radii of the wire strand, r_s , and of the Litz wire, r_L , are set to 0.08 mm and 2 mm, respectively, with this strand radius being chosen to ensure that the diameter is less than the skin depth, δ , so the reaction field due to the eddy currents can be neglected[135, 136]. The material resistivity at cryogenic temperature is considered:

$$\rho(T) = \begin{cases} a_0 + a_1 T + a_2 T^2 + a_3 T^3 + a_4 T^4 & 20 K \leq T \leq T_x \\ b_0 + b_1 T + b_2 T^2 + b_3 T^3 + b_4 T^4 & T_x \leq T \leq 20 K \end{cases} \quad (4.3)$$

where the coefficients a_i , b_i and T_x for copper and aluminium are given in table below:

Table 4.2 Coefficients for the resistivity of copper and aluminium at cryogenic temperature

Material	a_0 b_0 (nΩ·m)	a_1 b_1 (nΩ·m/K)	a_2 b_2 (nΩ·m/K ²)	a_3 b_3 (nΩ·m/K ³)	a_4 b_4 (nΩ·m/K ⁴)	T_x (K)
Cu	$3.692 \cdot 10^{-1}$	$2.214 \cdot 10^{-3}$	$-4.312 \cdot 10^{-4}$	$1.679 \cdot 10^{-5}$	$-9.311 \cdot 10^{-8}$	75.4
	-2.484	$5.699 \cdot 10^{-2}$	$1.078 \cdot 10^{-4}$	$-3.917 \cdot 10^{-7}$	$4.405 \cdot 10^{-10}$	
Al	$-7.55 \cdot 10^{-2}$	$2.167 \cdot 10^{-2}$	$-1.283 \cdot 10^{-3}$	$2.836 \cdot 10^{-5}$	$-1.306 \cdot 10^{-7}$	75.1
	-1.944	$1.958 \cdot 10^{-3}$	$9.07 \cdot 10^{-4}$	$-2.959 \cdot 10^{-6}$	$3.447 \cdot 10^{-9}$	

and the detailed calculation of resistance, R_{dc} and the skin depth are given in [130] as well.

$$R_{dc} = \frac{1}{N\sigma\pi r_s^2}$$

$$\delta = \sqrt{\frac{2}{\omega\mu\sigma}}$$

4.3.2.2 Analytical AC loss calculations: HTS tape winding

Compared to Litz wire coils, HTS materials have much higher current capacity, especially at lower operating temperatures such as 40 K. Therefore, they show great potential as stator windings for cryogenic motors. However, under AC conditions, HTS coils experience losses due to the transmitted current and external fields, and their performance depends strongly on the operating temperature and the ratio of the applied current to the critical current. The coil loss due to transport current and a sinusoidal background field is given below[45]:

$$P_{ac} = P_{trans} + P_{mag} \quad (4.4)$$

Where the transport current loss and the magnetization loss could be evaluated by Equation 3.5 and Equation 3.6 respectively.

The 4mm YBCO tape is used and its current capacity is assumed to be 50 Arms per tape at 0.68 T and 77 K, and 350 Arms per tape at 1 T and 40 K respectively according to information provided by SuperOx manufacturer [137].

4.3.3 Winding performance comparison

The two benchmarks are set to optimize the performance of Litz wire windings as much as possible to ensure a fair comparison to HTS winding. Regarding AC loss comparison of the three types of windings shown in

Figure 4.1 AC loss comparison for 450 kW benchmark at 77 K

, for 450 kW working at 77 K, the HTS coil produces much higher loss than the copper/aluminium Litz wire coil, but as the applied current increases, the loss difference reduces. As for the machine PTW ratio comparison, the total machine weights considered here are the active stator coil weight and all other component weight assumptions regarding the target PTW of short, mid and long term goals stated in Section 1.2. Regarding the PTW comparison in **Error! Reference source not found.**, Litz wire design has the best PTW performance, followed by HTS design and copper Litz design. The same result could be found in 1 MW benchmark working at 77 K.

However, a different result is given in 1 MW benchmark when further reducing the working temperature to 40 K. As shown in Figure 4.3, HTS coil still produces higher loss than Cu/Al Litz wire coil, however Al Litz wire generates higher losses than copper one because of higher eddy current loss due to lower resistivity. Nevertheless, HTS coil design always has the best PTW performance, especially if the machine weight could be reduced under 50 kg.

Therefore, regarding machine PTW, the advantage of HTS stator over Litz wire structure happens when the cryogenic temperature is low enough for HTS structure to show its superior current capacity.

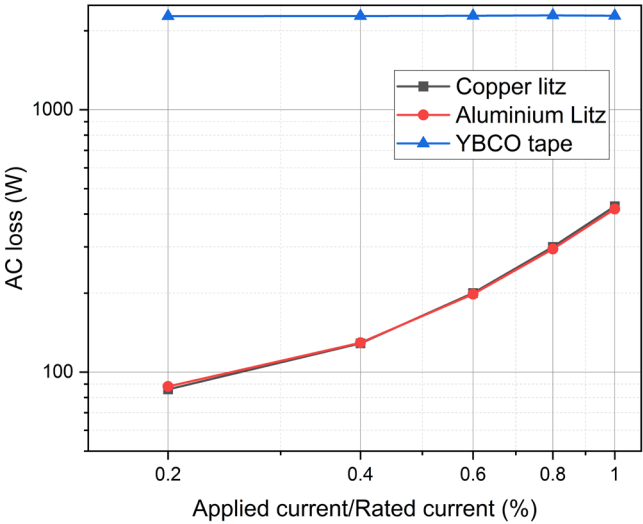


Figure 4.1 AC loss comparison for 450 kW benchmark at 77 K

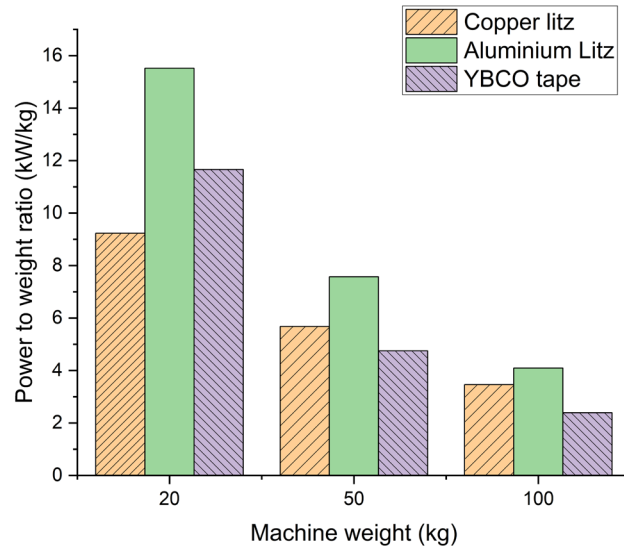


Figure 4.2 Power density comparison for 450 kW benchmark at 77 K

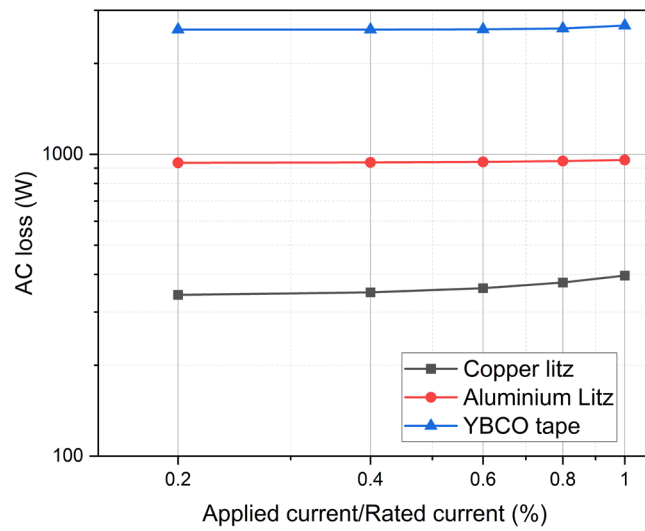


Figure 4.3 AC loss comparison for 1 MW benchmark at 40 K

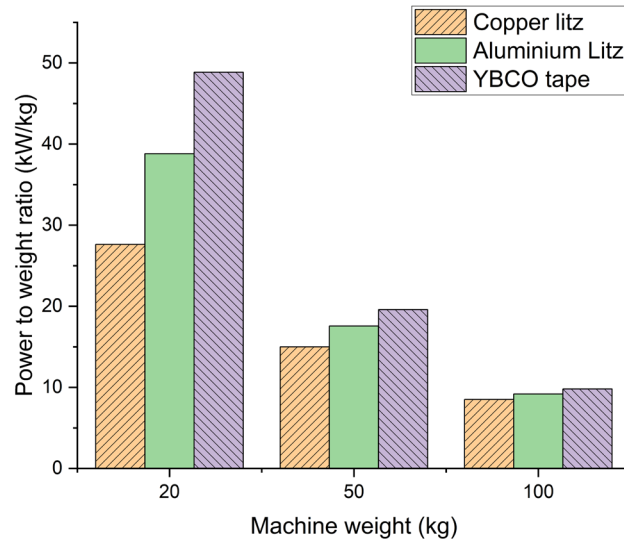


Figure 4.4 Power density comparison for 1 MW benchmark at 40 K

4.4 Conclusion

This study provides a comprehensive analysis of stator design, assessing the impact of the iron teeth and the AC loss evaluation in different armature winding designs of HTS radial flux synchronous motors. These motors are increasingly considered for electrified aerospace applications due to their improved PTW ratio and reduced losses under cryogenic conditions.

The study compared two motor benchmarks: 450 kW motor working at 77 K, and 1 MW motor at varying temperatures (77 K and 40 K). The 450 kW motor used a permanent magnet rotor, while the 1 MW motor used an HTS magnet rotor. There were three different stator winding types: copper/aluminium Litz wire, and HTS tape coil. Both benchmarks were evaluated in terms of stator AC losses as well as the motor PTW.

First of all, the iron teeth stator, which is desirable for conventional motor design because of its improvement in the main air gap magnetic field density and distribution waveform, is not an ideal choice for electrified aircraft motors. The main reason is that this rotor field strength could be achieved by using high field generating HTS magnets. On the other hand, iron teeth also add extra weight and produce hysteresis loss and eddy current loss. The eddy current loss in particular increases at cryogenic temperature as the conductivity of iron reduces. Therefore, slotless stator designs are more suitable for cryogenic environments.

As for the stator windings, for the 450kW level machine, at 77K the aluminium Litz wire stator performs cost-effectively as its AC loss is low, the unit price is cheap, and it has higher PTW than the HTS stator; while for the 1MW level machine, under 40 K the HTS coil shows a slight advantage of low AC loss and higher PTW. However, we should notice that since the benchmarks are set to optimize the performance of Litz wire structures, the HTS coil is far from its I_c in this specific case. In theory, higher power greater than 2 MW could be achieved by the HTS coil, which highlights the scalability of HTS technology for future high-power aerospace applications.

Therefore, the results indicate that lower cryogenic temperatures (40 K in this study) combined with higher applied currents relative to the critical current (I_c) are desirable conditions to maximize HTS stator performance. These conditions make HTS stators a convincing candidate for future electric propulsion systems in aviation.

In summary, aluminium Litz wire offers a competitive solution for medium power level motor design, especially at 77 K cryogenic temperature, while HTS coil technology is more beneficial for high power motors as the working temperature further decreases. For the development of MW level cryogenic HTS motors in electrified aviation, HTS stator designs, air core topologies, and operating temperatures at or below 40 K are preferred conditions to optimize performance and PTW.

Chapter 5 Impact to AC loss of standard HTS coil

5.1 Introduction

To consider using HTS coils as motor armature windings, the most important evaluation is the AC loss generated. This loss is sensitive to the coil working temperature and the applied current as well as to the external field. As mentioned previously in Chapter 2, the AC loss of type II superconductors can be categorized into two components: transport current loss caused by the carried current inside the superconductors without any external background field, and magnetization loss due to an external field in the absence of transport current. As the electrical loading is vitally important to the HTS stator coil, before considering the real machine environment, this chapter focuses on the impact of transport current on the coil AC loss. This chapter first analyses the HTS coil performance under different transport current conditions.

To simplify the case, a single HTS coil wound in a double pancake structure using 2G insulated HTS tape is analysed. This is the same testing coil that was used to validate numerical modelling in Section 3.5.5. The 2D axial symmetric model using the H-formulation is used to analyse the coil performance. In order to have a better understanding of coil loss considering the applied current conditions of a real machine, this study is divided into three main components. First, the coil transport current loss under different working frequencies is analysed at 77 K, with the current in the range of 12.5% to 75% of the coil self-field I_c , in AC sinusoidal form. To broaden the view, in the second part, two more working temperatures are considered: 65 K achievable by LN₂ and 40 K achievable by LH₂. For fair comparison, the same current and frequency ranges are applied. Finally, an extra current harmonic analysis is also considered in the end to see how the current harmonic components impact on coil transport current AC loss. Regarding [138], the 3rd, 5th and 7th component transport current harmonics have a great influence on the overall transport current AC loss. The current harmonic components considered here are the 5th and the 7th components, since the third harmonic component is neglected as it could be eliminated in three-phase motor design.

5.2 Applied current impact

This section first analyses the transport current loss, including losses under different working frequencies. The current applied to the coil is in the range of 10 to 60 A_{rms} in steps of 10 A_{rms} , referring to 12.5% to 75% of coil I_c , in AC sinusoidal form. The reason for not applying current until 100% of the coil I_c is to set a safe working margin thus avoiding any coil damage. The working frequencies are 25 Hz, 50 Hz and 100 Hz. All transport current loss results are shown in Figure 5.1. It is noticeable that the transport current loss increases only as the applied current increases. However, the loss frequency dependency is not very obvious. These results also agree well with the measurements given in Figure 3.16 and Figure 3.21.

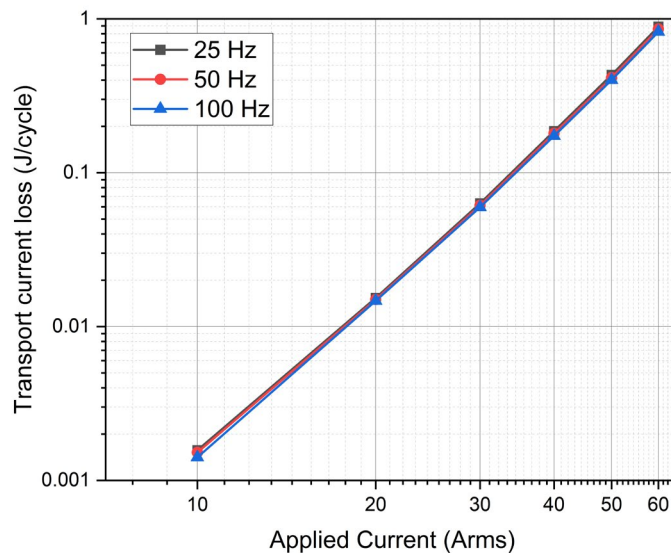


Figure 5.1 Transport current loss of the coil with different working frequencies at 77 K

5.3 Coil working temperature impact

As for the cryogenic environment, both 77 K and 65 K can be achieved by LN_2 , and 40 K can be achieved by LH_2 . Since the current capacity of HTS increases massively as the working temperature decreases, regarding the critical current lift factor in Table 3.2, the current capacity doubles as the temperature reduces from 77 K to 65 K, and this increases to 10 times from 77 K to 40 K. Therefore, to consider the possible cryogenic temperature for the future HTS stator, the transport current AC loss of the coil is calculated again under 65 K and 40 K.

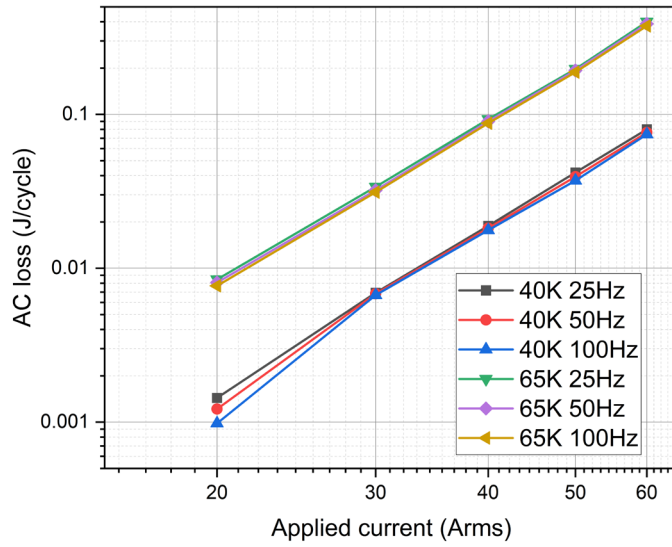


Figure 5.2 Transport current loss of the coil at 40 K and 65 K, respectively

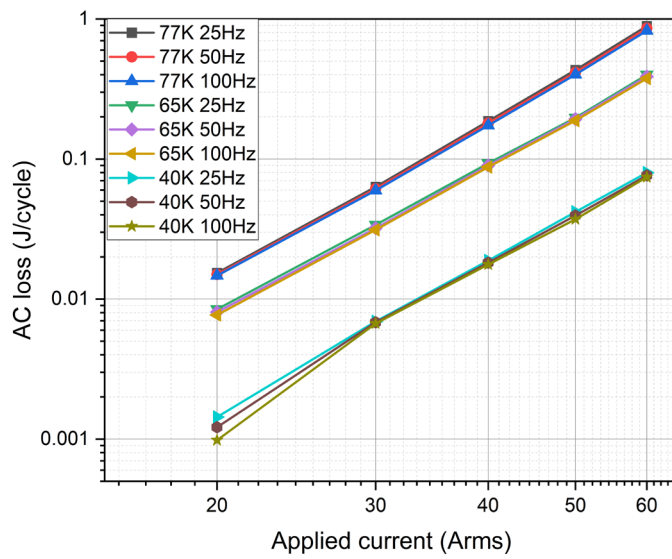


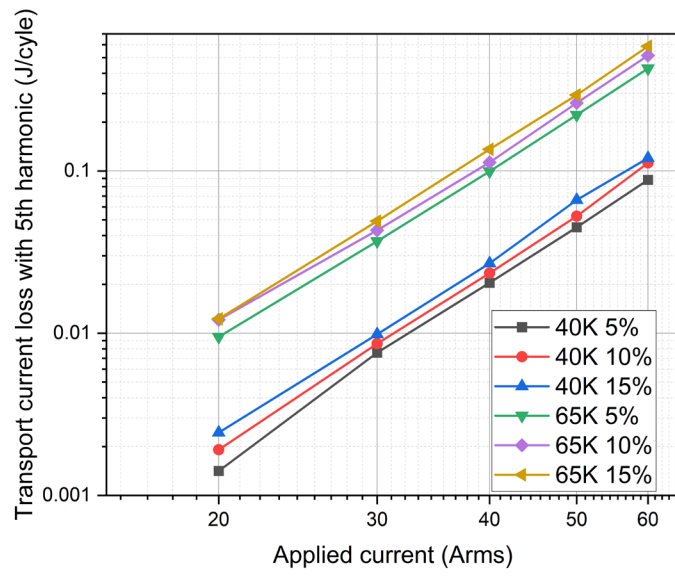
Figure 5.3 Transport current loss comparison at different working temperatures

The results show that the transport current loss under different working temperatures exhibits the same trend. The 10 A_{rms} cases for both 40 K and 65 K are not given here because the calculated loss is too small to be noticed. Figure 5.3 shows that as the critical current increases twice and 10 times from 77 K to 65 K and 40 K, respectively, the transport current loss reduces

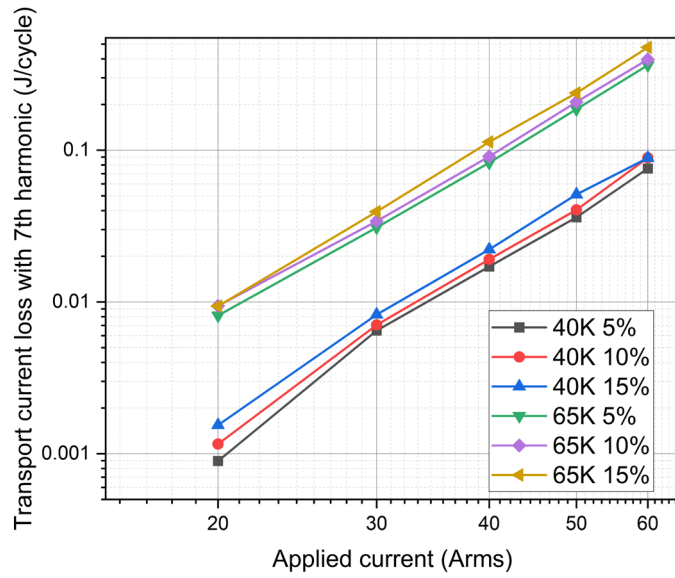
by 50% and 90%. Therefore, the transport current loss varies almost linearly with the critical current.

5.4 Applied current harmonics impacts

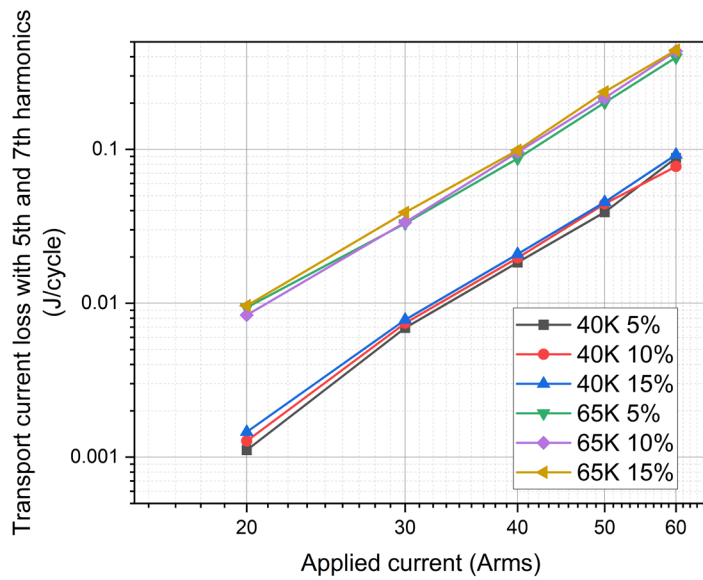
There is no third harmonic as a result of three phase armature design, however, as stated in[139], usually there will be unneglectable 5th harmonic and or 7th harmonic components in synchronous motors. As 18% of the 5th harmonic component is indicated in[139], it is reasonable to consider 5%–15% components of harmonics in this study. However, considering that the self-field I_c for the testing coil at 77 K is limited to 80 A, the applied current might reach beyond the coil current capacity when the fundamental component reaches 50 or 60 A_{rms} , especially when considering the 5th and 7th components at the same time. Therefore, the current harmonic impact on the coil transport current loss is tested at temperatures below 65 K and 40 K only. The transport current loss results regarding different harmonic components are shown in Figure 5.4. It is observed that in most of the cases, the higher the fundamental current, the higher the total transport current AC loss. In fewer cases such as the 7th harmonic and both 5th and 7th case at 40 K, when the fundamental applied current is 60 A_{rms} , the total transport current loss with 5% of harmonic component is greater than that of 10% of harmonic component. This can be explained by the elimination of the total current amplitude. Higher harmonic components sometimes result in a lower total current amplitude. All the results in Figure 5.4 are at 100 Hz, however, the same trend can be found at 25 Hz and 50 Hz.



a)

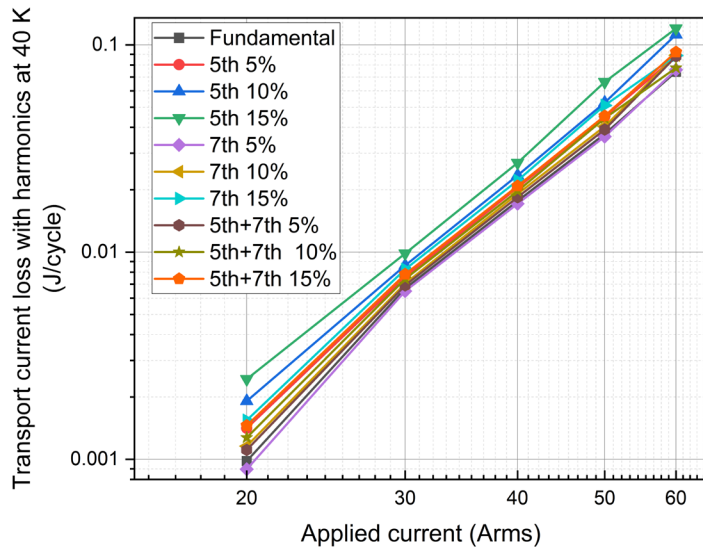


b)

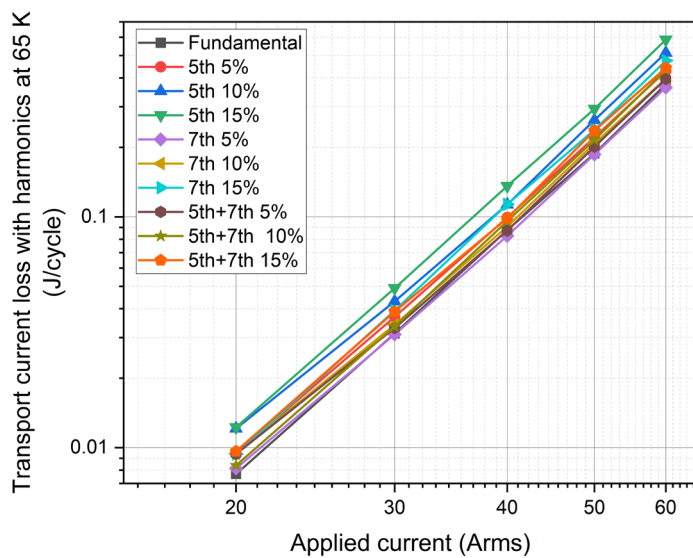


c)

Figure 5.4 Transport current loss considering current harmonics at 100 Hz: a) 5th harmonic components; b) 7th harmonic components; and c) 5th and 7th harmonic components

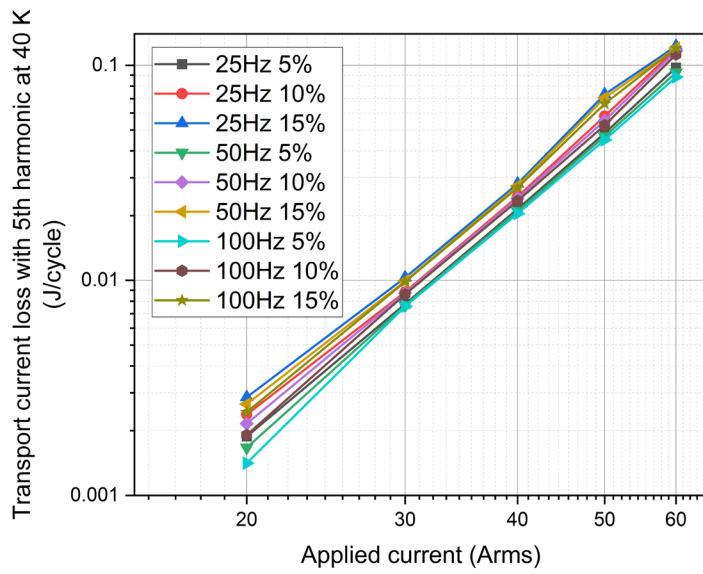


a)

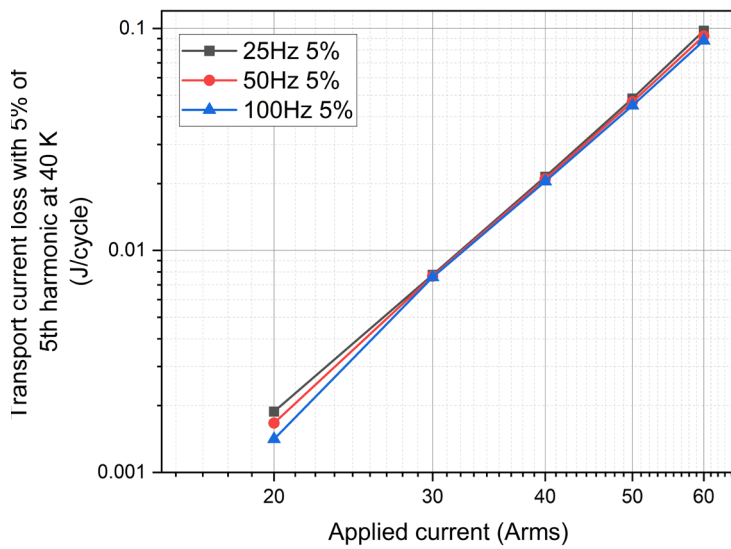


b)

Figure 5.5 Transport current loss considering current harmonic components a) at 40 K; and b) at 65 K. By comparing all the harmonic cases at 40 K and 65 K respectively, regardless of the working temperature, the highest loss happened at the case with 15% of the 5th harmonic component applied, while the lowest loss happened at the case with 5% of the 7th harmonic component applied. The 5th component has bigger impacts than the 7th harmonic. Therefore, the 5th harmonic component has a higher impact on the transport current loss. In the following part, the same loss evaluation is conducted at 25 Hz and 50 Hz to figure out the frequency impact.

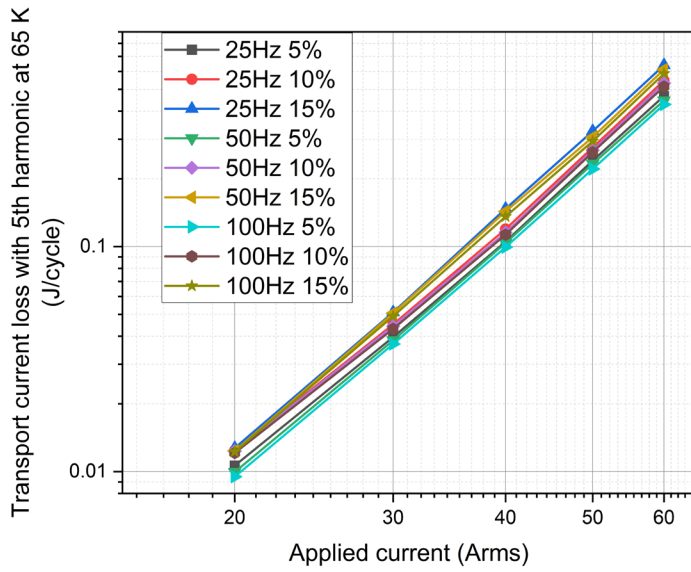


a)

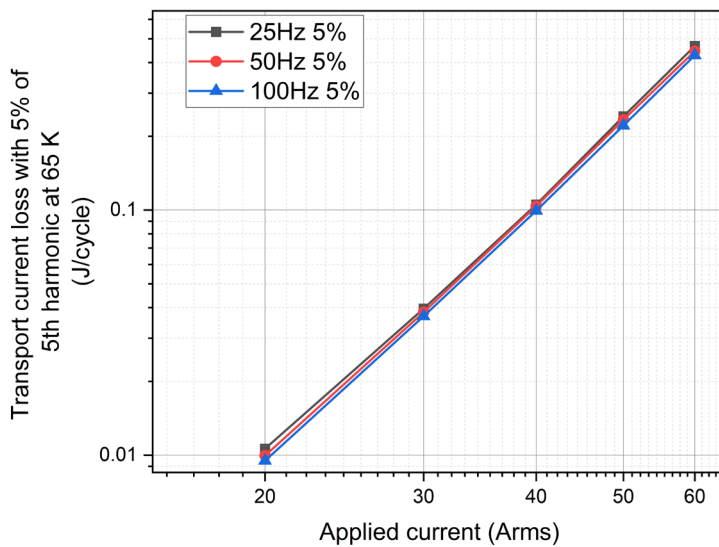


b)

Figure 5.6 Transport current loss with 5th current harmonic frequency dependency at 40 K a) harmonic components in portion of 5%, 10% and 15%, respectively; and b) 5% of harmonic component



a)



b)

Figure 5.7 Transport current loss with 5th current harmonic frequency dependency at 65 K a) harmonic components in portion of 5%, 10% and 15%, respectively; and b) 5% of harmonic component

As shown in Figure 5.6 and Figure 5.7, the transport current loss considering harmonic components only has a slight increase as the frequency grows regardless of the working temperature variation, and the same trend could be observed for the other two harmonic cases. In summary, at same working temperature, the portion of harmonic components has the dominant impact on the magnitude of transport current loss.

5.5 Conclusion

HTS coils, particularly those made from 2G YBCO tapes, have shown significant promise in applications such as motor armature windings due to their high current capacity and low energy losses under optimal conditions. Transport current loss refers to the loss as the current passes through the superconducting coil in the absence of an external magnetic field. This loss is significant as it is related to the electrical loading of the HTS stator coils. This chapter delves into a comprehensive analysis of transport current AC losses of HTS coils wound from insulated tapes under various transport current conditions, focusing on transport current and its possible harmonic components, working frequencies, and the working temperatures. The key findings and implications of the study are summarised below.

The study employed a 2D axial symmetric model using the H-formulation to simulate the YBCO coil performance accurately. The model was validated with experimental data (see Section 3.5.5 for details), ensuring reliable prediction of AC losses under different conditions. The double pancake coil used here was the same testing coil used for previous model validation. After the modelling validation, this study conducted the transport current loss analysis in the following order:

The analysis first focused on the effect of the sinusoidal transport current at various frequencies (25 Hz, 50 Hz, and 100 Hz). The results show that transport current loss increases with the amplitude of the applied current, but has little dependence on the operating frequency. This highlights that current amplitude, rather than frequency, is the dominant factor affecting transmission current losses in HTS coils.

Meanwhile, the study explored the effect of operating temperature on transport current AC losses by simulating coil performance at 77 K, 65 K, and 40 K. The results show that the loss reduced with decreasing temperature. This reduction became more significant after increasing the applied current. This finding emphasizes the importance of optimizing operating temperatures in HTS applications to enhance efficiency. For example, reducing the temperature from 77 K to 40 K can reduce transport current loss by up to 90%, emphasizing that efficiency improvements can be achieved through advanced cryogenic cooling techniques.

The study then extended the focus to analyse the effects of applied current harmonics, specifically the 5th and 7th harmonic components that are common in synchronous motor

operation. The results show that the amplitude of the harmonic components significantly affects the transmission current losses, with the 5th harmonic having a greater impact than the 7th harmonic. Interestingly, some scenarios show that higher harmonic contributions reduce the total current amplitude, thus slightly mitigating the losses. These exceptions are caused by the total current amplitude reduction after considering the current harmonics. Despite these exceptions, the overall trend confirms that minimizing harmonic distortion in the applied current is critical to reducing transport current AC losses.

In addition, the effect of frequency on harmonic losses was evaluated. While frequency variation (25 Hz, 50 Hz, and 100 Hz) had a limited effect on harmonic impacted transport current losses, the proportion of harmonic components in the applied current was the dominant factor. These findings are critical for the design of HTS stator windings in electric motors, as the applied current harmonic distortion must be minimized to achieve optimal performance.

In summary, this chapter provides a detailed evaluation of the transport current AC losses of HTS coils according to the conditions relevant to electric motor design in electric propulsion systems. The results show that operating temperature (coil critical current) and the proportion of current harmonic component have great impact on the transport current loss.

The results from this analysis provide a foundation for future research and development of more efficient HTS stator design. Future work should explore the combined effects of both transport current and external rotating magnetic field to represent the actual operating conditions of HTS armature windings. In addition, experimental validation of the harmonic loss model in actual motor designs will further enhance the understanding and application of HTS technology in electric propulsion systems. The real portion of harmonics should also be considered to enhance the simulation results. Hence, in the next chapter, the HTS armature windings will be placed under real motor environments with different rotor generated magnetic fields to analyse the total AC loss generated on the windings.

Chapter 6 HTS armature AC loss analysis under radial flux HTS motor environment

6.1 Introduction

Nowadays, electric aircraft have become popular as a result of aviation regulations on efficiency, noise and emissions. To commercialize electric aircraft, the motor to be designed requires high power. According to [11], the smallest commercial air transport requires 2 MW power. Meanwhile, air transportation also requires light weight and small size. The high power density required by MEA/AEA makes superconducting motors a promised solution. Recently, the MEA is undergoing a transition from conventional fuel aviation systems to hybrid or full electric aviation propulsion systems. Liquid hydrogen (LH₂) is a good candidate as a potential sustainable aviation fuel. Recent projects, for instance, ASCEND (Advanced Superconducting & Cryogenic Experimental Powertrain Demonstrator) by Airbus group, propose that LH₂ could be both fuel and coolant for the whole propulsion system. This idea makes superconducting machines a more competitive candidate for MEA, since superconducting machines need low working temperatures.

As indicated in [90], the critical current decreases dramatically under a field perpendicular to the width of the tape. As for HTS stator performance in a real machine environment, besides the transport current impact discussed in Chapter 4, there is also the impact of the rotational field generated by the machine rotor part. As mentioned before in Chapter 2, HTS materials will suffer from high AC loss especially when there is a large background field. Hence, in the next step, the HTS stator needs to be placed in a real motor environment.

This chapter will analyse the radial flux synchronous HTS motor performance focusing on AC loss produced by HTS armature windings. The HTS motor designs studied here are a partially HTS motor with permanent magnet (PM) rotor and HTS stator, and a fully HTS motor with both HTS rotor and stator for radial flux machine. From an armature point of view, the main difference between a partially and fully HTS motor is the surrounding magnetic loading. The motor design analysis goes from their design and sizing methodology to modelling and finally gives the AC loss performance for stators. With the help of radial flux motor analysis, potential ways of reducing AC loss in HTS stator winding are presented in the end.

6.2 Radial flux partially HTS motor

Compared to a traditional electric magnet rotor (generated by wound field winding via DC current) and an HTS rotor working in a low temperature environment, a permanent magnet has the advantage of easy manufacturing while maintaining good magnetic field distribution. Though the field generated by a PM is lower than that generated by an HTS rotor, this magnetic field generated in the range of 0.5 T to 1 T [140] enables an HTS armature to carry higher current as the HTS critical current decays a lot under a high background field. Regarding [25, 133], the airgap magnetic field between 0.5 T and 0.9 T, the electrical loading of an HTS armature could reach as high as 250 kA/m. Therefore, the machine topology studied for a radial flux partially HTS motor is a synchronous motor with PM rotor and HTS stator. Moreover, as discussed in Chapter 4, the iron slots are removed to make an slotless structure to further reduce the machine weight and increase the machine power-to-weight ratio (PTW). An analytical technique for finding machine equivalent circuit variables of slotless radial flux partially HTS motor is developed. It is achieved through MATLAB coding, and the output variables include induced electromotive force (EMF), HTS armature winding inductance and its equivalent AC resistance. The output from this 2D analytical modelling is compared with the results from corresponding finite element modelling fulfilled in COMSOL. The overall HTS armature AC loss and its equivalent AC resistance are calculated from 10% to 100% of its rated electrical loading within the temperature range of 30 K to 75 K. The preferred HTS stator working conditions, particular temperature and electrical loading are carried out in the end. This equivalent circuit model could be used in an electric system to analyse the HTS motor impact on the whole system.

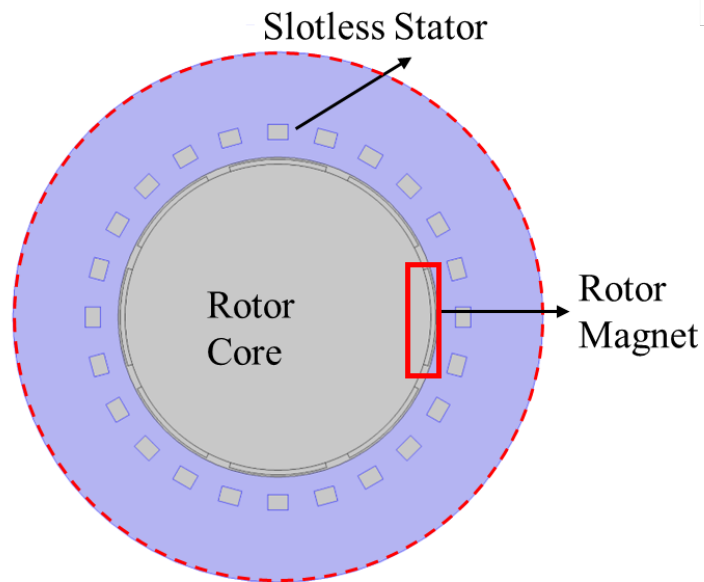


Figure 6.1 An example structure of radial flux partially HTS motor: PM rotor and HTS Stator

6.2.1 Design methodology

Initially, this study introduces a general analytical model for a slotless radial flux PM-HTS (i.e. permanent magnet rotor and HTS stator) motor. The analytical modelling will be realized through simplified MATLAB coding. The expected model output as shown in Figure 6.2 aims to obtain machine equivalent circuit variables for a given voltage and rated power. The modelling process is illustrated in Figure 6.3. The main target to obtain variables of the equivalent circuit is highlighted in a red box. The induced electromotive force (EMF) will be calculated through definition of the EMF for conductors with the help of the rotor magnetic field analysis, armature winding inductance will be determined by magnetic energy in inductance, and finally the AC loss of armature winding will help figure out the equivalent AC resistance. All the results obtained will be checked through numerical modelling. Although this study only considers the steady state mode, transient fault conditions such as short circuits are worth analysing in the future. After all the parameters in equivalent circuit are analysed, the possible machine optimization function can be figured out.

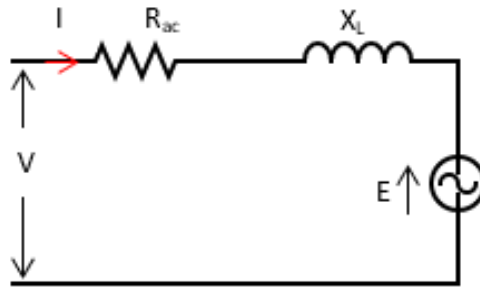


Figure 6.2 Machine equivalent circuit diagram

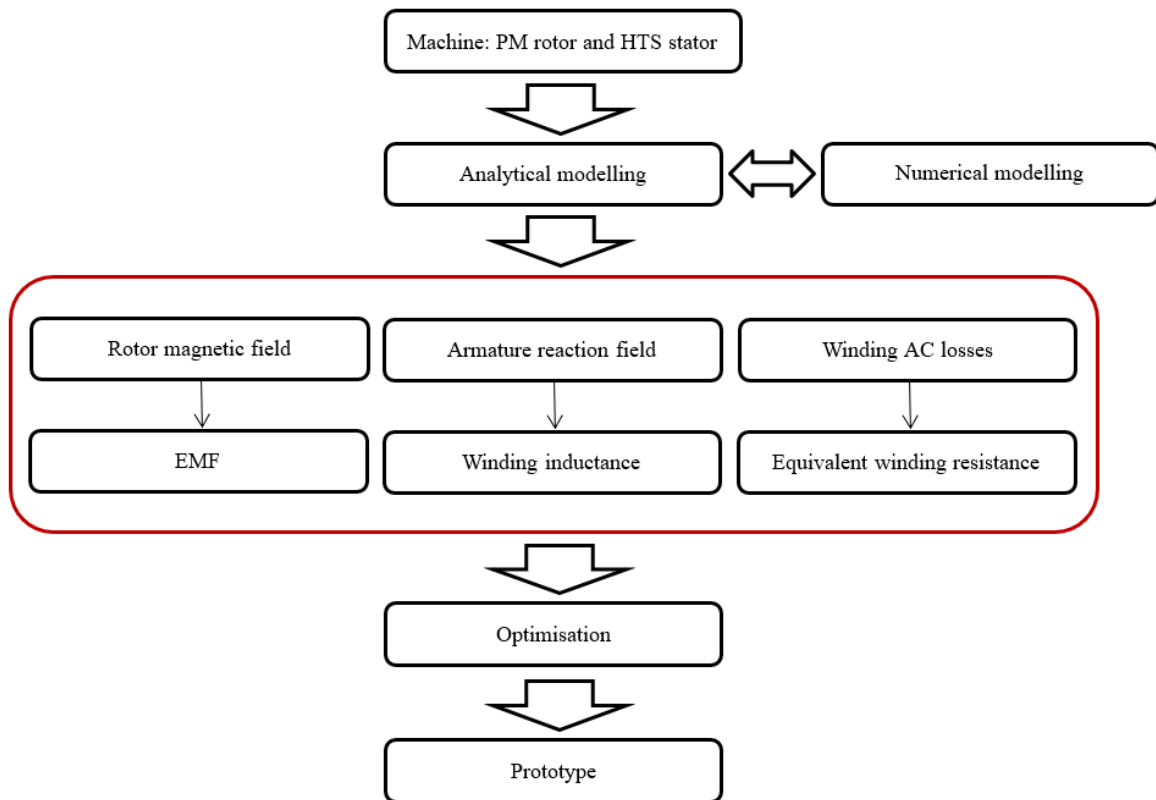


Figure 6.3 The analytical modelling process flow chart

6.2.2 Structure of the machine

A schematic cross-sectional view of a slotless radial flux PM-HTS motor is given in Figure 6.4, where R_r is the rotor hub radius, R_g represents the mean air gap radius and R_s is the outer radius of the stator winding. As curve length is close to straight-line length when it is small, and the difference in length between the upper and lower arc edges is very small, it is reasonable to simplify sector shape cross-section to a rectangular shape in the magnetic field study. The rotor

magnet is mounted on the surface of the rotor yoke, and the distributed HTS winding is chosen for the stator as we assumed distributed HTS winding could be achieved in the future. The motor dimensions according to its structure are given in Table 6.1 below.

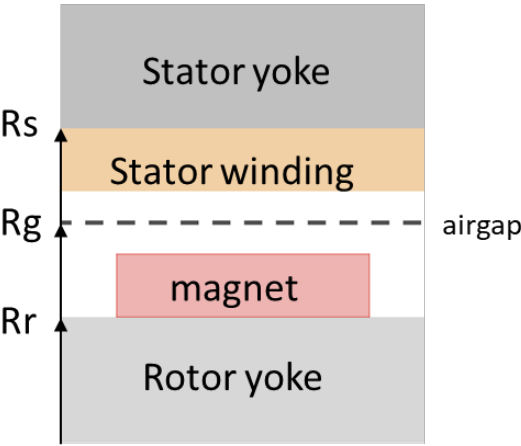


Figure 6.4 A simplified one pole structure of a slotless partially HTS motor with permanent magnet rotor

Table 6.1 Design dimension parameters of the slotless radial flux PM-HTS motor

	Characteristic	range	Units
stack length	L	65	mm
rotor radius	R_r	183.5	mm
stator radius	R_s	201.3	mm
stator yoke height	H_{sy}	14	mm
air gap height	G	3.5	mm
pole pitch	τ_p	102	mm
ratio of magnet width to pole pitch	α_p (i.e. w_m/τ_p)	75%	
magnet width	W_m	74	mm
magnet height	H_m	9.5	mm
rotor yoke height	H_{ry}	14	mm

The magnet air gap is 3.5 mm, which is slightly bigger than the conventional PM machine since this is a slotless design. The ratio of magnet width to pole pitch is chosen to be 75% [141, 142] for an initial investigation.

The motor electrical specifications are provided here. The machine output power is set to 450 kW with a 170 Vrms phase voltage. The airgap magnetic loading is 0.68 T which is a better performance value than PM rotors[140]. It should be noticed that currently there is not any distributed HTS armature winding design available, but there are studies [143, 144] showing

that quasi distributed HTS winding design could be achieved by connecting HTS coils in series in different layers [145, 146]. Hence we are using distributed winding design in this study, and the coils per phase are set to 12.

Table 6.2 Design electrical parameters of the slotless PM-HTS motor

Parameter	symbol	range	unit
output power	P	450	kW
pole pair number	p	6	
input phase voltage	V _{ph}	170	V _{rms}
rated speed	ns	5000	rpm
input frequency	f	500	Hz
airgap magnetic loading	B _g	0.62	T
Armature Winding design			
stator winding distribution	distributed		
no. coils per phase	12		

6.2.3 Modelling methodology

6.2.3.1 Magnetic field distribution

The induced EMF depends on the rotor magnetic field. Hence, the main task here is to model airgap flux density. A 2-D analytical method for predicting open-circuit field distribution analysis is proposed in [147]. The method decouples the whole magnetic flux density waveform into different harmonic components through Fourier expansion. Considering the n th harmonic component, in general, for typical inner rotor outer stator topology as shown in Figure 6.5, no-load rotor magnetic field distribution in both radial and axial directions respectively are given in Equation 6.1 and Equation 6.2. The harmonic components considered in this study are the fundamental, 3rd, 5th, 7th and 9th.

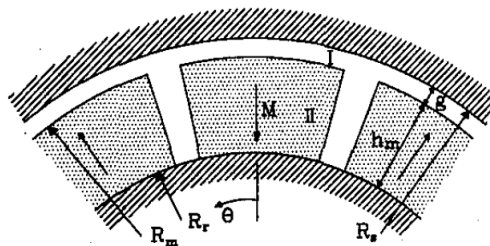


Figure 6.5 Inner rotor PM machine cross section scheme [7]

$$\begin{aligned}
B_r(r, \theta) &= \sum_{n=1,3,5,\dots}^{\infty} \frac{\mu_0 M_n}{\mu_r} \frac{np}{(np)^2 - 1} \cdot \left\{ \frac{(np - 1) + 2 \left(\frac{R_r}{R_m}\right)^{np+1} - (np + 1) \left(\frac{R_r}{R_m}\right)^{2np}}{\frac{\mu_r + 1}{\mu_r} \left[1 - \left(\frac{R_r}{R_s}\right)^{2np}\right] - \frac{\mu_r - 1}{\mu_r} \left[\left(\frac{R_m}{R_s}\right)^{2np} - \left(\frac{R_r}{R_m}\right)^{2np}\right]} \right\} \cdot \left[\left(\frac{r}{R_s}\right)^{np-1} \left(\frac{R_m}{R_s}\right)^{np}\right] \\
B_\theta(r, \theta) &= \sum_{n=1,3,5,\dots}^{\infty} \frac{-\mu_0 M_n}{\mu_r} \frac{np}{(np)^2 - 1} \cdot \left\{ \frac{(np - 1) + 2 \left(\frac{R_r}{R_m}\right)^{np+1} - (np + 1) \left(\frac{R_r}{R_m}\right)^{2np}}{\frac{\mu_r + 1}{\mu_r} \left[1 - \left(\frac{R_r}{R_s}\right)^{2np}\right] - \frac{\mu_r - 1}{\mu_r} \left[\left(\frac{R_m}{R_s}\right)^{2np} - \left(\frac{R_r}{R_m}\right)^{2np}\right]} \right\} \cdot \left[\left(\frac{r}{R_s}\right)^{np-1} \left(\frac{R_m}{R_s}\right)^{np}\right] \\
M_n &= 2 \left(\frac{B_r}{\mu_0}\right) \frac{\sin \frac{n\pi\alpha_p}{2}}{\frac{n\pi\alpha_p}{2}} \tag{6.3}
\end{aligned}$$

where p is the pole pair number, R_m is the magnet surface radius, residual magnetization vector, and α_p is the magnet pole-arc to pole-pitch ratio.

This model is validated through numerical modelling in COMSOL. As mentioned previously, a geometry simplification to rectangular shape is made in the finite element (FE) model in COMSOL. As shown in Figure 6.6, the PM rotor flux density distribution for one pole pair section is illustrated. As indicated in Figure 6.7, evaluation of the radial flux density distribution using both analytical and FE models shows good consistency. Meanwhile, the air gap flux density value is around 0.62 T where the fundamental component is around 0.68 T.

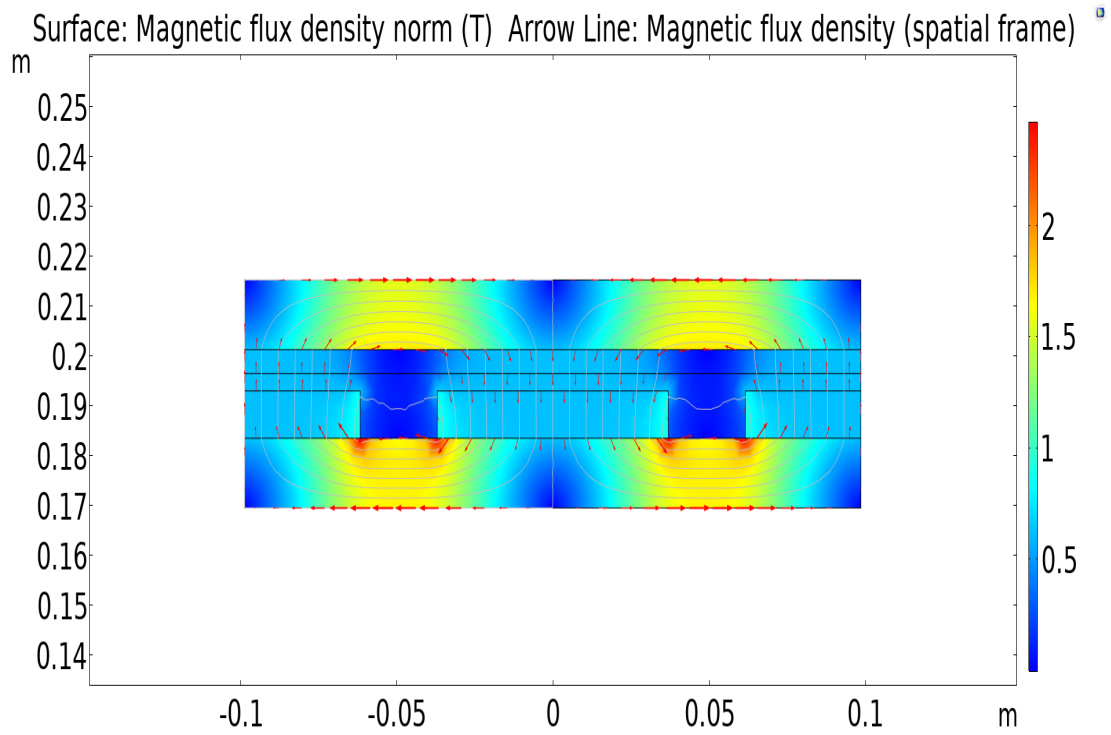


Figure 6.6 PM rotor no-load magnetic flux density distribution

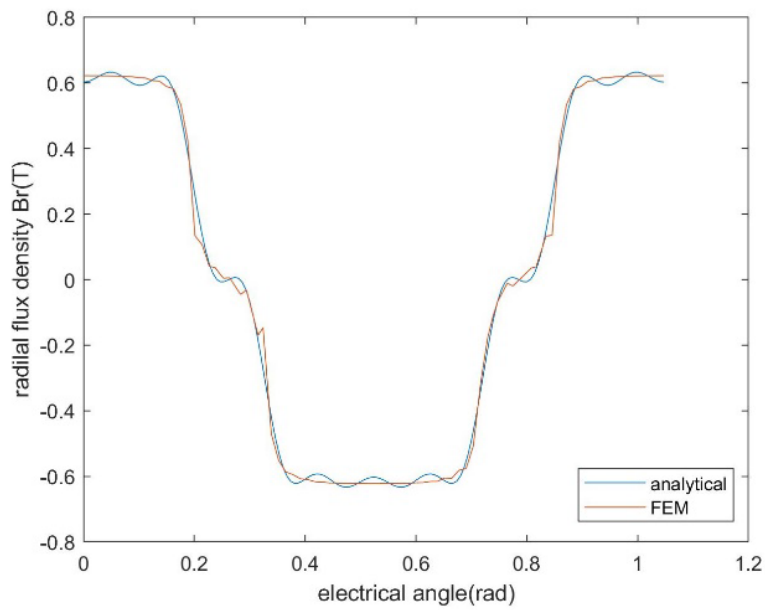


Figure 6.7 Analytical modelling validation for rotor radial flux density

6.2.3.2 Inductance of armature winding

The stator winding distribution along one stator pole pair is illustrated in the figure below.

This distributed winding design has 36 slots in total and 1 slot per phase per pole.

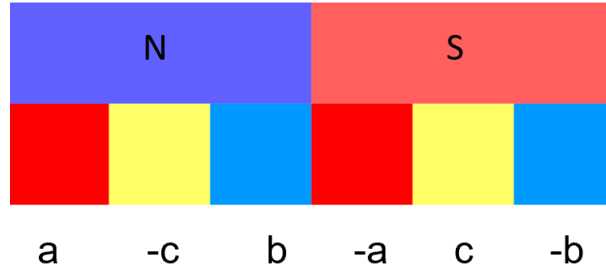


Figure 6.8 Stator winding distribution

The inductance is obtained through the definition of induced emf:

$$emf = N \frac{d\phi}{dt} = L \frac{di}{dt} \quad (6.4)$$

where N is the winding turn per phase and L is the self-inductance per phase. Considering mutual inductance between phases, paper [148] proposed a factor, k_L , that can transfer inductance per phase to total three phase inductance:

$$k_L = \frac{4(\pi - \kappa)}{3\pi - 4\kappa} \quad (6.5)$$

where κ is the half angular width of a winding slot. The results of analytical modelling are compared with results obtained from FEM. The method used in FEM is to calculate inductance through magnetic energy:

$$E_{p,m} = \frac{1}{2} LI^2 \quad (6.6)$$

As can be seen in the results of this study, the analytical modelling agrees well with FEM, only giving about 1% difference lower than the FEM value.

Table 6.3 Inductance modelling case study results

Inductance	Analytical	FEM	Unit
1 phase	49.5	50.08	μH
3 phase	66.9	-	μH

6.2.3.3 AC resistance of armature winding

The HTS coil is assumed to use YBCO insulated tapes manufactured by SuperOx. The AC resistance of the HTS tape is determined by working temperature, frequency and the machine geometry. It is hard to describe it through one equation, therefore, in this study AC resistance is calculated through the definition of AC losses,

$$P_{loss} = I^2 R_{ac} \quad (6.7)$$

where the AC losses of HTS tapes are obtained through numerical modelling in COMSOL using the T-A formulation as explained in [68], which is also validated in Section 3.5.5.

For this 6 pole-pair motor design, an AC resistance analysis is given here. Only one-twelfth of the machine (one pole) is modelled for reasons of calculation time efficiency. Figure 6.9 gives a one-twelfth machine model in detail in COMSOL, in which the simulation work regarding to different working temperature as well as electrical loadings has been completed. The working temperature range is from 30 K to 75K. The rated phase current is stated to be 1000 A_{rms}, and the electrical loading varies from 10% to 100% of its rated loading.

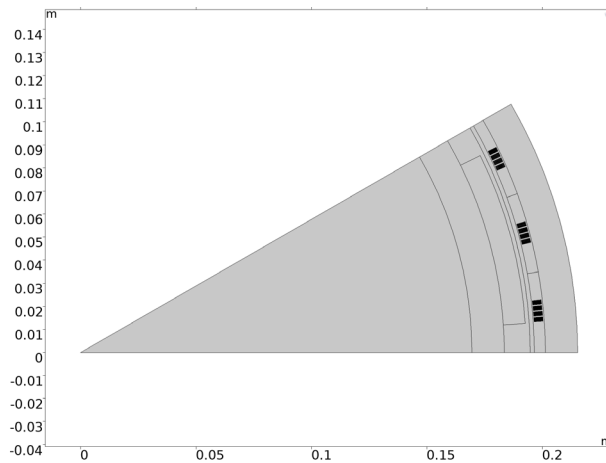


Figure 6.9 One-twelfth machine model built in COMSOL

We should noticed that, since the machine working frequency is around 100 Hz which is far beyond the kHz range, the AC resistance can be assumed to be the same as the DC resistance. The final AC resistance values are plotted in Figure 6.10, in which the AC loss of the HTS armatures increases dramatically when the applied current is above 80% of the rated current and the working temperature is above 65 K. Considering the cooling temperature of liquid nitrogen (LN₂) could be 65 K, it is better to keep the coil working temperature as low as 65 K. As further reducing the working temperature will not reduce AC loss dramatically, and the cooling budget for lower temperature is high, 65 K is an ideal working temperature for an HTS coil working under a background field lower than 1 T. Regarding the equivalent AC resistance figure, this method is limited when the applied current is low, under 50% of rated current in this case. This is because AC loss is proportional to the square of current I, the equivalent R_{ac} will be very high when the applied current is quite low. However, it is worthwhile to evaluate this

equivalent resistance when the current is quite high and close to the rated current, which is the normal HTS stator working condition. It also helps us to figure out that the equivalent AC resistance as well as the AC loss increases dramatically when the working temperature is around 77 K.

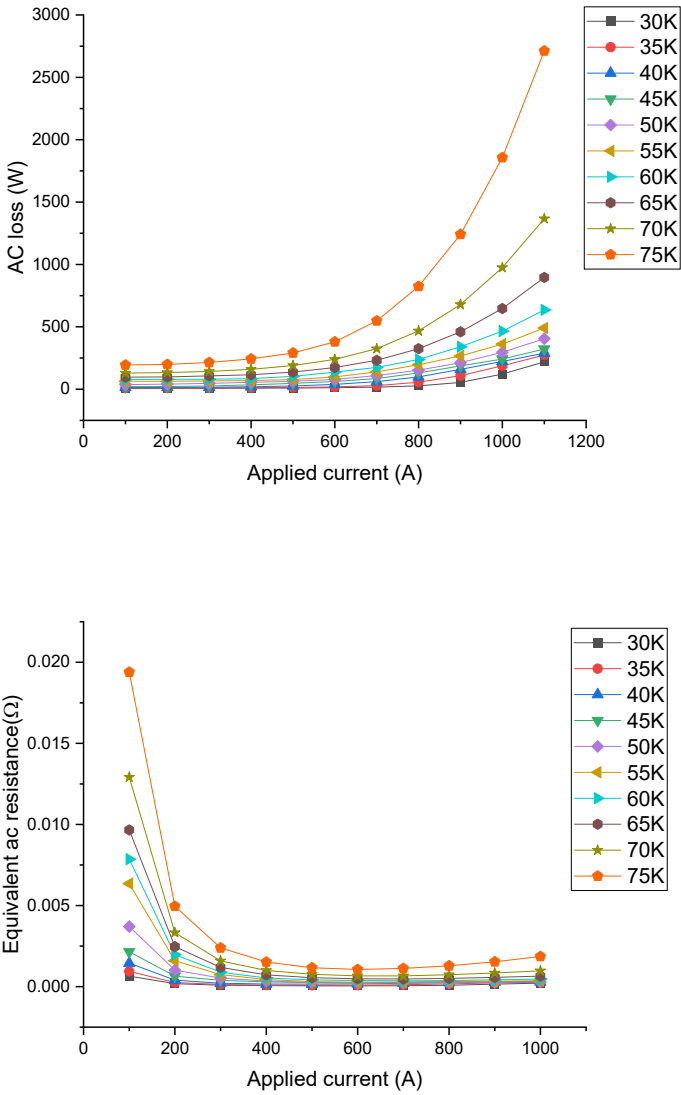


Figure 6.10 HTS armature performance results of a) ac loss; and b) equivalent ac resistance

6.3 Radial flux fully HTS motor

It is known that partially HTS motor design using a PM rotor has a magnetic loading limit less than 1 T. In addition, within the slotless structure, this value becomes 0.5 T or even lower. Hence,

a fully HTS motor using YBCO HTS coils as field winding could help to increase magnetic loading up to several T[149]. In general, the use of HTS materials for both the rotor and stator significantly enhances the motor's performance by enabling high current densities and strong magnetic fields.

Taking the advantage of high field generation from the HTS coil, the mean stator magnetic field can easily achieve the range of 0.5–0.9 T suggested by[25, 133]. Meanwhile, the electrical loading of the HTS armature could still reach as high as 250 kA/m as in the partially HTS motor design. Therefore, this section provides a radial flux fully HTS motor analysis where both rotor and stator use coils wound by insulated YBCO tapes. Since a motor with MW level output power is required to achieve the MEA target[11], the motor benchmark chosen here is a MW level fully HTS machine design.

This study consists of three parts: rotor HTS field winding design and its possible optimization considering using multiple current leads, stator HTS armature winding design and its potential optimization focusing on AC loss reduction, and finally the shielding or back iron impacts on the magnetic loading performance.

6.3.1 Design methodology

The design process begins with establishing the requirements for the motor, including power output, operating frequency, and magnetic loading. Analytical and computational methods are then used to optimize the design parameters to meet these requirements.

The topology chosen in this study is 2G HTS racetrack coils for both rotor and stator windings of a radial-flux slotless machine. The machine sizing equation is taken from the general radial flux machine form[150]:

$$P = \frac{\pi^2}{\sqrt{2}} k_w B_s A_s D^2 L n_s \quad (6.8)$$

And the motor benchmark design parameters regarding to this equation are shown in table below.

Table 6.4 Design parameters of the slotless radial flux fully HTS motor

Parameter	Symbol	Value	Unit
machine power	P	2.3	MW
pole pair number	p	2	
frequency	F	50	Hz
electrical loading	As	200	kA/m
magnetic loading at mean armature winding radius	Bs	1	T
effective machine length	L	0.5	m
armature winding position mean diameter	D	0.402	m

The machine output power is set to 2.3 MW considering that only two pole pairs are considered in this study for reasons of geometry simplification. It should be noticed that the output power is set to around 2 MW rather than 1 MW here. The reason is that regarding the analysis in Chapter 4, the advantage of high current capacity for HTS armature design is more attractive when the power reaches 2 MW. The magnetic loading refers to the field at the mean mature winding position.

6.3.2 HTS rotor design and optimization

The rotor of this fully HTS motor is designed using HTS tape to create the field winding. The primary goals in rotor design are to maximize the magnetic field strength and especially enhance sufficient magnetic field along the armature winding position for a slotless motor. The chosen configuration for this study includes HTS racetrack coils, which are known for their ability to achieve high magnetic fields and ease of manufacture. The machine structure is shown in cross section scheme below:

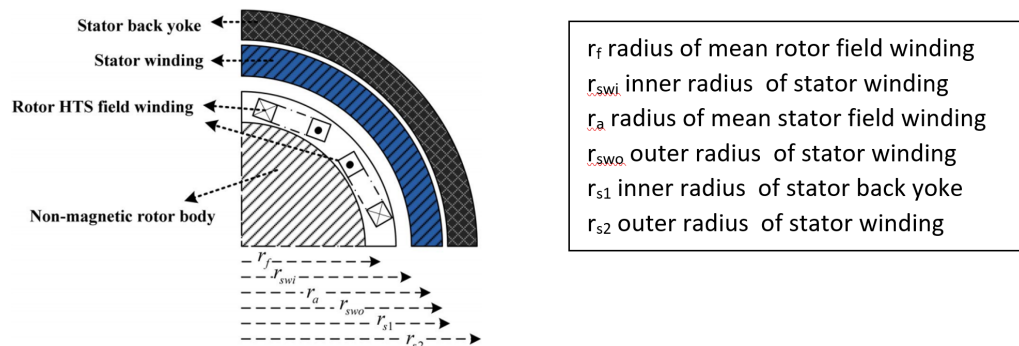


Figure 6.11 Diagram of machine cross section [151]

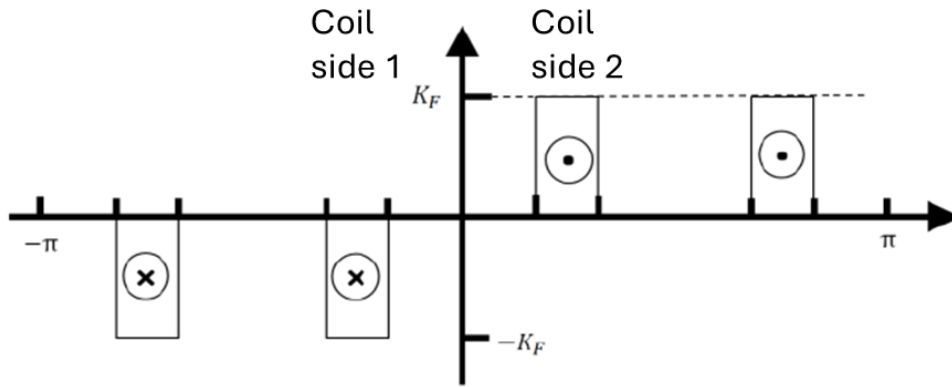


Figure 6.12 Rotor coil distribution along machine electrical angles

An analysis of magnetic field distribution, including Fourier analysis, is employed to study the magnetic field distribution[45]:

$$B_r = \begin{cases} \frac{\mu_0 K_{Fn}}{2} \left(\frac{r}{r_f}\right)^{np-1} \left\{1 + \left(\frac{r_f}{r_x}\right)^{2np}\right\}, & 0 < r < r_f \\ \frac{\mu_0 K_{Fn}}{2} \left(\frac{r_f}{r}\right)^{np+1} \left\{1 + \left(\frac{r}{r_x}\right)^{2np}\right\}, & r_f \leq r \leq r_s \end{cases} \quad (6.9)$$

where r_f is the mean field winding radius, r_x inner radius of shielding, n represents the harmonic number and K_{Fn} indicates the linear current density of the coil.

The field distribution over machine radius is calculated through both analytical and FEM methods. Only the magnetic field radial component is compared because it is the flux density component that is of interest in the radial flux machine design. The field distribution amplitude is plotted over the machine radius with respect to the field winding position. It is obvious that the magnetic flux density from the analytical method is bigger than the result from FEM simulations when the radius is smaller than the mean rotor field winding radius, while the result consistency is consistent when the radius is bigger than the field winding radius. However, the big difference in the beginning will not greatly influence the rotor field distribution analysis since the stator part is placed outside the rotor, which means that the field analysis will only focus on the machine part where the r/r_f ratio is greater than one. In this case, the field result difference should be caused by the ignorance of every tape position in the analytical method.

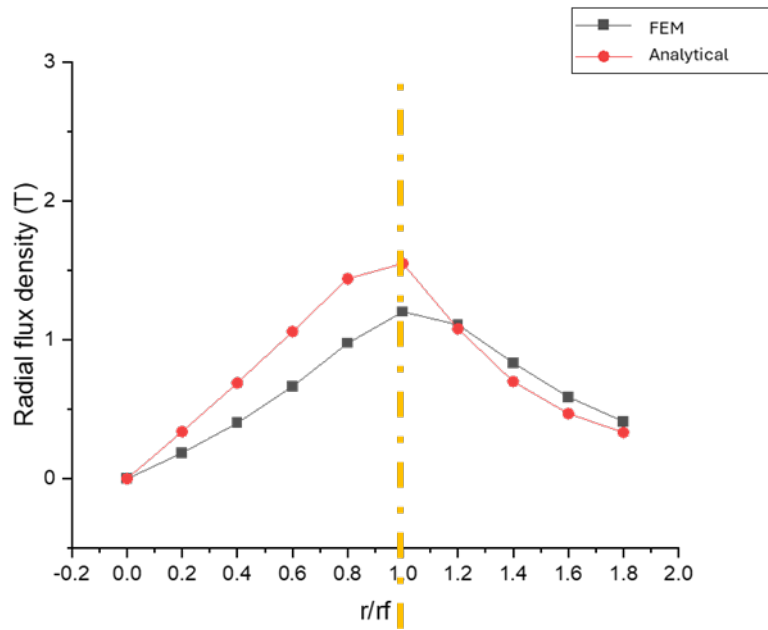


Figure 6.13 Analytical method validation for rotor field flux density

As indicated in Figure 6.14, the red colour part indicates the current penetration to the tapes. For the HTS rotor field winding, the current penetration starts from the outer toward the inner tapes, thus the inner tapes are not sufficiently used. An optimization idea that focuses on enhancing the magnetic field and its uniformity might be to introduce multi-current leads. With the help of multiple excitation currents applies to different parts of the field windings, the use of the central tapes in the coil will increase thus avoiding inner tape material waste and enhance the magnetic flux density waveform.

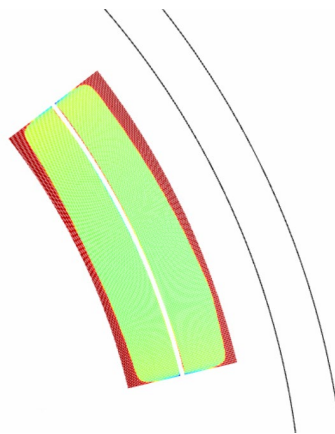


Figure 6.14 Field winding current penetration

A two current leads (CL) system is proposed here. The first CL with 100% of the applied current is given to the external tapes, while the second CL with an extra 20% of the applied current is applied to the inner tapes. The ratio of inner tapes over the whole coil is assumed to be one third in this design. The current waveforms for two CLs as well as the applied current distribution along one side of the coil are illustrated in Figure 6.15 and Figure 6.16 respectively.

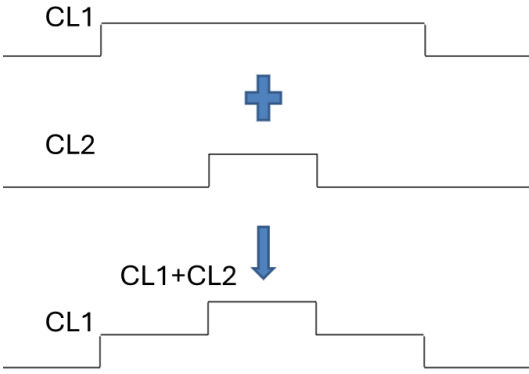


Figure 6.15 Current wave as a result of superposition of multi current leads

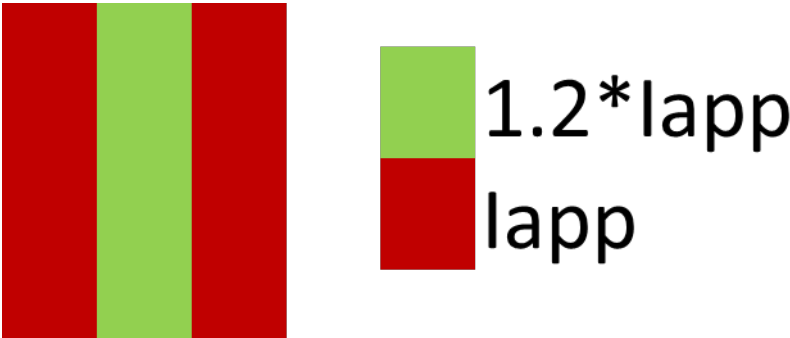


Figure 6.16 Two current leads applied to rotor HTS coil with one third of inner tapes having higher current

The radial flux density enhancement with two CLs is shown in Figure 6.17. The optimization results indicate that using two CLs with the central (1/3 tapes) current increased to 120% of the original applied current can significantly enhance the rotor field by 10%. Meanwhile the arc length of field over the peak value increased which further improves the magnetic loading.

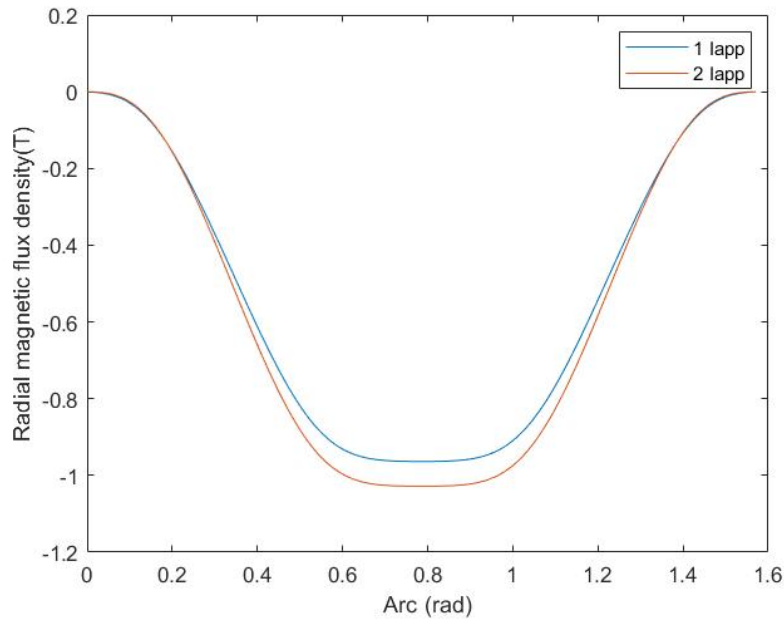


Figure 6.17 Radial flux density comparison between one current lead and two current leads

6.3.3 HTS stator design and optimization

The stator of this design also uses HTS tapes for the armature winding, with a slotless (slotless) design to reduce the machine weight. The design aims to achieve high electrical loading while minimizing AC losses. The stator parameters are listed in Table 6.5. The electric loading is chosen to be 200 kA/m based on some previous research on HTS armature design[29, 30]. The armature working temperature chosen here is 65 K regarding the previous analysis in Chapter 5.

Table 6.5 Stator design parameters

Parameter	Symbol	value	unit
machine power	P	2.3	MW
pole pair number	P	2	
frequency	F	50	Hz
electric loading	As	200	kA/m
magnetic loading	Bs	1	T
stator current	Is	150	A _{rms}
stator voltage	Vs	2.3	kV
stator cable turn	Ns	64	

To reduce AC losses, the stator design is optimized by considering different tape widths here. The T-A formulation in COMSOL is used for AC loss calculations, which involves solving the E-J power law in the superconducting domain. It is assumed here that 1 mm and 0.5 mm tapes can be manufactured in a mature manner in the future. AC loss increases as tape width reduces from 4 mm to 2 mm. However, narrower tape widths are found to reduce AC losses effectively if the tape width further reduces from 2 mm to 0.5 mm, as shown in Table 6.6. It is noticed that the loss increases at first from 4 mm tape to 2 mm tape and then reduces. This could be explained considering the current penetration in the tape. The current distribution for four coils at the peak applied current is displayed in Figure 6.18.

Table 6.6 AC losses for different tape widths

Tape width	4 mm	2 mm	1 mm	0.5 mm
layer	2	4	8	16
J/cycle/m	2670	3210	3170	1300
total AC loss (kW)	534	642	634	260

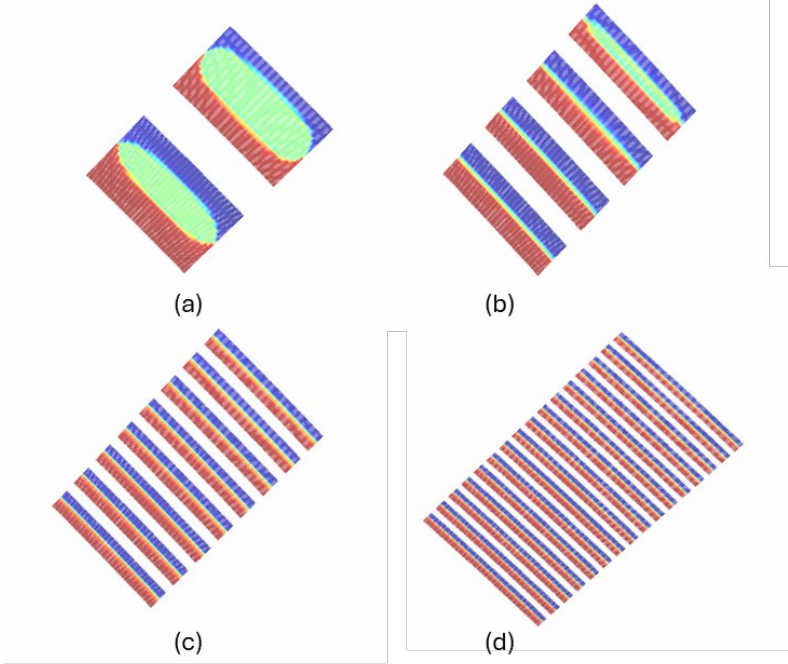


Figure 6.18 The current penetration for different tape widths a) 4 mm; b) 2 mm; c) 1 mm; and d) 0.5 mm

6.3.3.1 Critical current degradation considerations

Considering the current commonly used existing tape dimensions, the AC loss comparison is conducted again with the tape width ranges from 12 mm to 2 mm. In addition, regarding the critical current data available from manufacturers, there will be a critical current degradation

while doing tape width cutting. Here are some assumptions for this critical current degradation analysis. The 12 mm and 8 mm tapes have the same critical current, I_c , level with 4 mm tapes, since the degradation from 12 mm to 4 mm is not that obvious. However, the I_c degradation of 2 mm tape is considered after checking through the critical current measurements from manufacturers[152], since the I_c level for 2 mm tape is assumed to be 80% of that for 4 mm tape.

Table 6.7 AC loss results comparison for different tape widths considering I_c degradation

Tape width [mm]	12	8	4	2	2 (with degradation)
Coil layer	1	1	2	4	4
Loss [J/cycle/m]	3140	2940	2670	3210	3120

As can be seen here, AC loss reduces from 12 mm to 4 mm, but increases when further cutting the tape width to 2 mm. Moreover, when considering the I_c degradation for 2 mm tape, the AC loss is slightly smaller than the case without I_c degradation. As the total AC loss is a sum impact of transport current loss and magnetization loss, and these impacts could not be linearly summed up, AC loss will not purely reduce by narrowing the tape width. Among these analysis, in the range of 2–12 mm tapes, 4 mm tape performs the best.

6.3.4 Shielding considerations: back iron impact

Back iron is usually used to provide magnetic shielding, however the stator back iron accounts significantly for the machine total mass which influences the total machine PTW, hence the stator back iron impact is analysed here. A case study of the impact of a back iron with 4 mm thickness on motor magnetic loading as well as the armature AC loss is given here. With the help of the equivalent magnetic circuit of the machine, the magnetic loading for slotless machine is small since the reluctance in the stator part is very big. The back iron helps to enhance the magnetic loading. At the same time, since the AC loss of a HTS is affected by the flux penetration direction with respect to the tape width surface, the AC loss of the armature is also calculated considering the stator back iron.

The use of thin layer (4 mm) of back iron (shielding) in the stator has no obvious magnetic loading improvement, as the air core is very big as indicated in Figure 6.20. However, the thin shielding can impact the current penetration of the armature tapes, thus the overall stator AC loss. The coil AC loss reduces from 3580 J/cycle/m to 2670 J/cycle/m after adding the extra thin layer of back iron. Therefore, for each specific motor design, back iron could help improve

the overall motor performance, however, decisions regarding its thickness should be a trade-off between magnetic loading, stator AC loss and machine weight.

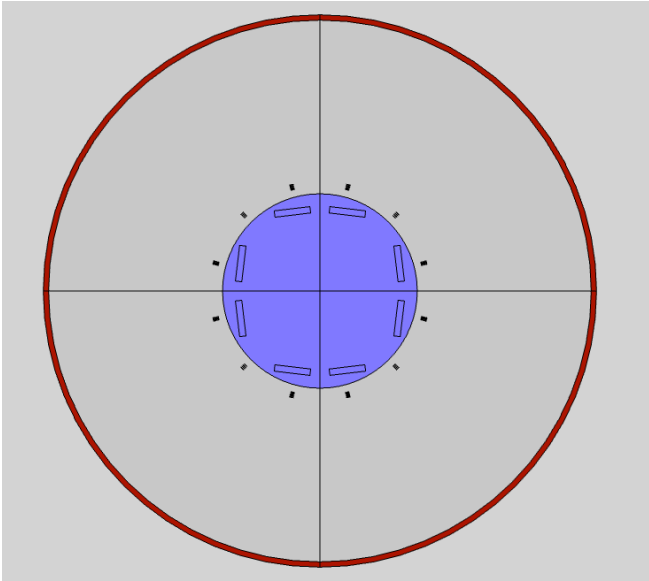


Figure 6.19 The machine structure with 4 mm back iron

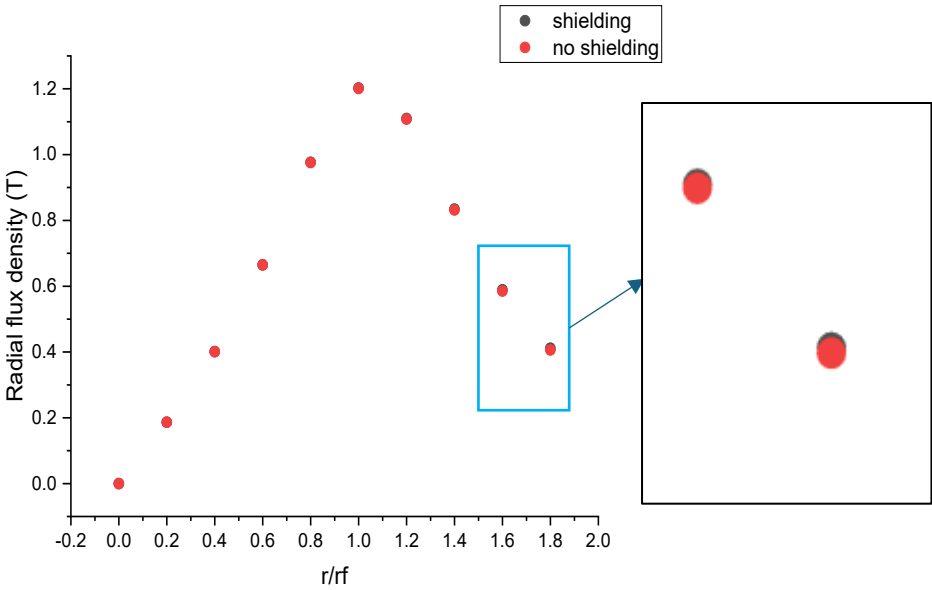


Figure 6.20 Radial flux density with and without shielding

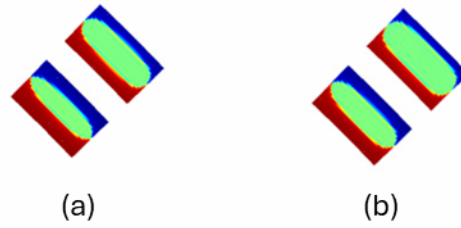


Figure 6.21 Shielding impact on stator winding current penetration a) without shielding; and b) with shielding

6.4 Conclusion

The radial flux synchronous HTS motor is a potential candidate for MEA/AEA propulsion systems. This chapter discussed the design and performance analysis of the HTS motors focusing on HTS armature AC loss evaluation and minimization for both partially HTS motors and fully HTS motors. The two configurations of HTS motors are: a 450 kW partially HTS motor with a PM rotor and an HTS stator, and a fully HTS motor rated at 2.3 MW using HTS coils for both rotor and stator. Both designs were analysed by analytical and FEM methodologies.

For the 450 kW PM-HTS motor, a slotless radial flux topology with a PM rotor and HTS stator was developed. An analytical technique, validated with FE analysis, was proposed to find machine equivalent circuit variables of this slotless partially PM-HTS motor. The main parameters of the equivalent circuit such as induced electromotive force (EMF), armature winding inductance, and HTS armature equivalent AC resistance were calculated. In the end, an equivalent circuit lookup table could be built and embedded into a whole electric propulsion system to figure out the motor impact on the whole system.

As for the study of stator equivalent AC resistance, the calculation was achieved with the help of FEM modelling in COMSOL. It also revealed agreement with previous studies that maintaining the HTS stator's working temperature at around 65 K (below 77 K), a temperature achievable with liquid nitrogen cooling, is essential to managing AC losses effectively. The results showed that increasing the HTS coil temperature above 65 K led to rapid increases of AC loss, indicating that careful thermal management is needed in HTS armature design. Meanwhile, to maximize the benefits of using HTS armature, it is important to maintain the stator electrical loading as close as possible to the HTS critical current capacity.

For the 2.3 MW fully HTS motor, designed with HTS coils in both the rotor and stator, the use of multiple current leads in the rotor could significantly improve the rotor magnetic flux density waveform. For example, by applying 120% of the rated current to the inner HTS tapes, the field component of interest (radial flux density) was enhanced by approximately 10%. However, it also introduced extra complexity to the rotor structure.

An optimization strategy for the HTS stator was also developed, emphasizing the reduction of AC losses by reducing the HTS bandwidth. The results demonstrated that the AC loss will reduce dramatically if the tape width is narrower than 2 mm. The findings showed that the AC loss initially increased when tape width reduced from 4 mm to 2 mm, but decreased significantly for widths below 1 mm. This AC loss comparison for different tape widths indicated that the total AC loss of an HTS armature is a nonlinear sum of transport current loss and magnetization loss. Considering current commonly used tape dimensions, the 4 mm tape performs the best as the stator winding.

Finally, the impact of back iron on magnetic loading enhancing and stator AC losses reduction was evaluated. Although the addition of a thin 4 mm back iron layer showed no obvious improvement in magnetic loading due to the large air-core structure, it effectively reduced the stator AC loss by modulating the direction of magnetic flux penetrating the tapes. This result indicates that the back iron can help improve the overall performance of the motor, but decisions regarding its thickness need further analysis, optimization and will become a trade-off between magnetic loading, stator AC losses, and machine weight.

Table 6.8 2.3 MW motor stator optimization results considering AC loss performance

Stator coil tape width impact				
tape width [mm]	4	2	1	0.5
AC loss/AC loss of original motor design	100.00%	120.22%	118.73%	48.69%
Shielding impact				
Shielding thickness [mm]	0		4	
AC loss/AC loss of original motor design	100.00%		74.86%	

In summary, this study provides a comprehensive analysis of HTS armature design for HTS motors, highlighting the impact of tape width and effective shielding on the HTS stator performance. The results highlight the potential of HTS motors to achieve the high power density and efficiency required for next generation electric aircraft propulsion systems. This

study also gives the direction to quantify the HTS armature design optimization focusing on its AC loss reduction.

Chapter 7 Transport current AC loss analysis of multi-stack HTS coil

7.1 Introduction

To achieve the ambitious zero-emissions aviation goal, electrified aircraft propulsion systems are proposed as a potential solution. Previous studies have proved that a fully HTS motor could be a promising solution. The HTS armature outperforms in the design of multi MW level electrical machines, which require power density no less than 20 kW/kg [17, 42] and high efficiency. Though HTS materials can sustain high current, this current capability reduces dramatically under a background field, especially within the high fields of several Tesla [153, 154] generated by an HTS rotor. Meanwhile, considering the machine voltage regulations, aircraft motors at high altitudes require low voltage and high current to avoid electric discharge [20, 32, 146, 155]. In order to improve the stator electrical loading (i.e. increase the machine current capacity), multiple tapes could be bundled together. Nevertheless, with a large number of insulated tapes bundled together, the winding difficulty increases in terms of thermal and mechanical stability.

Hence, in this chapter, a new stacked coil structure is proposed with multiple tapes stacked and soldered together and then connected in parallel. This soldered structure improves the coil thermal and mechanical stability. Besides, within this low voltage and high current stacked coil structure, the number of coil turns is reduced thus the inductance of the coil is reduced in the end, which is desirable for motor design [74, 119]. The lower coil inductance [156] enables faster current response and reduces reactive impedance, which enhances torque response and increases power density, while also minimizing inverter switching losses, thereby improving overall efficiency and performance. In the meantime, the motor would be smaller, lighter and operate more smoothly.

This study gives a comprehensive transport current AC loss analysis of these HTS YBCO stacked coils for electric propulsion applications targeting the stator armature design. Initially, the novelty of the stack coil structure is introduced by comparison to currently existing multi-filamentary coil studies, and the purpose of using such a structure is also explained. The characteristics that affect the coil transport current loss are analysed afterwards, including

tape/stack current distribution and the stack inductance differences. Both experiments using the electric method and numerical modelling using the 2D axis symmetrical H-formulation are proposed to help understand the coil performance under AC transport current conditions.

7.2 Novelty of the stack coil design

The main purpose of using a parallel-tape configuration is to achieve high current capacity and stability in superconducting coils of superconducting motors for aviation applications. As explained in Section 3.3.2, multi-filamentary coils are divided into two main types regarding their methods of electrical connection: coupled-at-the-end case and fully coupled case, as shown in Figure 3.2. However, the inductance difference between each current path will result in an uneven current distribution. In terms of coil stability, non-uniform currents can cause imbalances in electromagnetic forces, leading to mechanical stresses and vibrations. In addition, coil areas with higher current density are more likely to overheat, result in thermal instability. At the same time, extra losses are also introduced by this uneven current distribution: eddy current loss in the metallic layer, coupling losses due to the transferring current between electrically connected tapes[69], and greater hysteresis loss in areas with higher current. This AC loss increases coil temperature and could result in quenches.

Although there are many studies about the AC loss characteristics of multi-filamentary coils, considering the hysteresis loss and coupling loss[119, 120, 157, 158], and proposed numerical modelling methods, such as T-A coupling with an electrical circuit, Minimum Electro-Magnetic Entropy Production (MEMEP), to simulate the coupling effects among these coils in stacked structure[119, 159, 160], the behaviours of every tape, especially the relationship between current distribution in a stack and the corresponding AC loss properties, are not stated in detail. Meanwhile, there is lack of sufficient result comparison between measurement and simulation. The latter study, which will be conducted in this study, helps to give a better understanding of stack coil behaviour, and figure out the possibility of reducing stack coil AC loss thus better using stack coils in HTS armature windings. In addition, to improve the inductance impact analysis focusing on the coil current distribution and the coil total transport current AC loss, two cases of both big and small inductance differences between stacks are investigated here.

7.3 Stack coil geometry

The stack structure implies two tapes stacked together through a metallic soldering layer. The coil is designed for a specific machine prototype: a double-stator single-rotor axial flux motor with a rated power of 100 kW. The rated current required for one stator is 160 A_{pk}. To further increase the coil current capacity to achieve this electrical loading target, two stacks with four tapes connected in parallel are wound to form a double stack coil. The coil structure is displayed in Figure 7.1 and the coil dimensions are listed in Table 7.1.

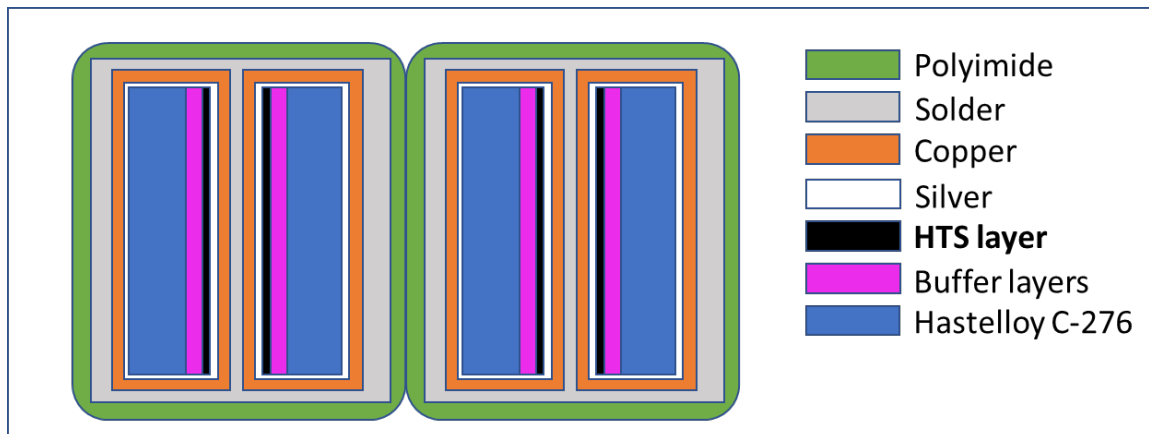


Figure 7.1 The stack coil structure

This coil is wound from SuperOx 2G YBCO tapes. The tape width is 4 mm, and for each coil turn, two tapes are stacked together through a metallic soldering layer, and located face-to-face with each other. The copper stabilizer around each tape is about 20 μm thick and the soldering layer around every coil turn is made by 5 μm PbSN. With the double pancake structure, there are 46 turns in total (23 turns per layer) and every turn has two stacks in parallel. The extra soldering layer is used to maintain the coil mechanical and thermal stability.

The coil structure is labelled in Figure 7.2, in which the grey thin lines indicate the HTS tapes soldered together in a stack, and the surrounding brown block represents all the other metal layers including soldering and stabilizer. For every coil turn, there are two stacks connected in parallel. The yellow solid box describes one of the two stacks in a coil turn that is located closer to the coil centre while the extended blue dashed box describes the stack in a coil turn that is located further from the coil centre. The detailed information of this stacked coil is given in Table 7.1. The measurements and testing are conducted in an environment at 77 K provided by LN₂.

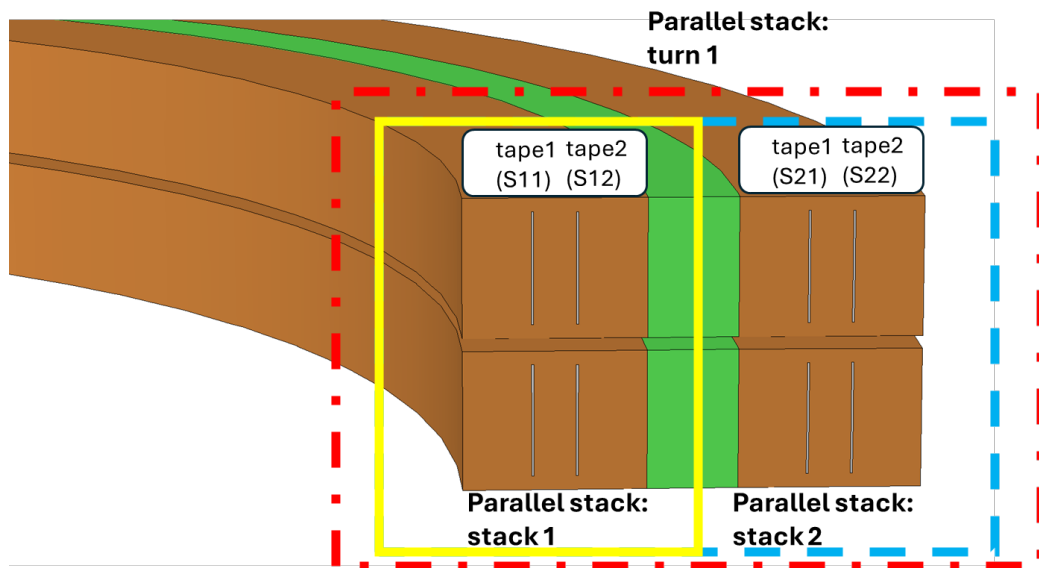


Figure 7.2 Coil structure scheme, with the HTS layer in grey, the metallic soldering in brown, and the insulation in green. The yellow solid box and blue dashed box mark the two stack turn.

Table 7.1 Stack coil parameters

Parameter	Value	Unit
inner diameter	60	mm
outer diameter	80	mm
n° of tapes per stack	2	
n° of stacks per turn	2	
n° of turns	46	
tape width	4	mm
stack tape thickness	0.23	mm
self-field I_c	250	A _{DC}
working temperature	77	K

7.4 Coil measurement setups

7.4.1 Coil critical current, I_c determination

The coil self-field critical current, I_c , measurement result is given in Figure 7.4, measured twice from both stacks to ensure the accuracy. The inner and outer stacks refer to the stacks placed inside and outside, respectively, and the coil self-field, I_c , is around 250 A.

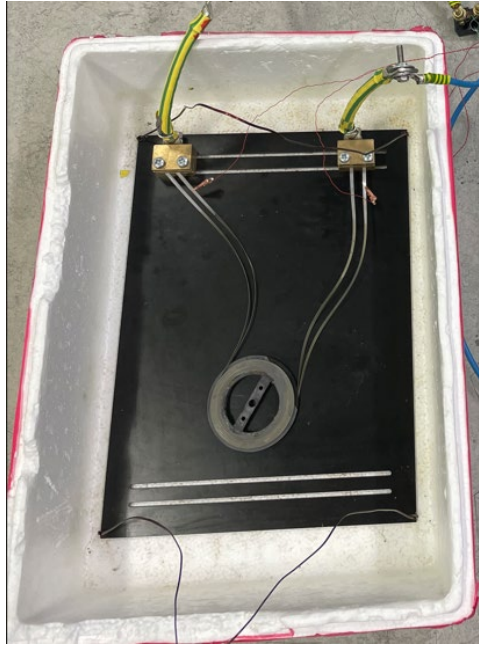


Figure 7.3 Real stack coil for testing

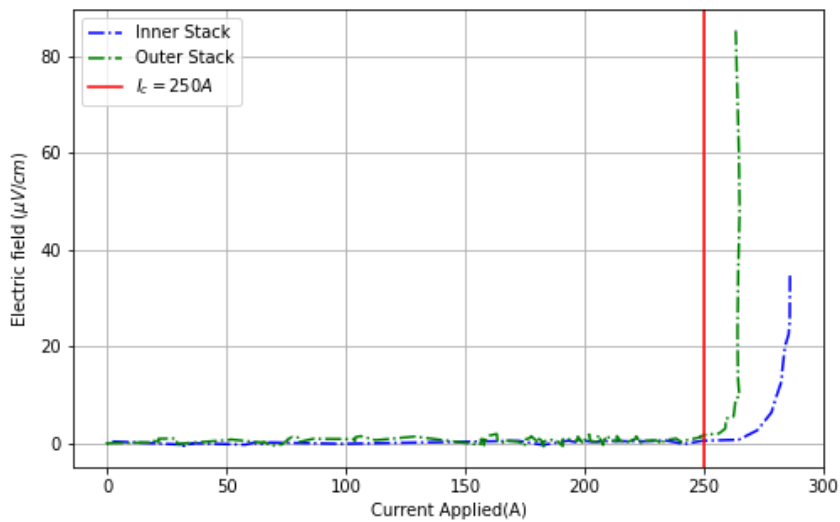


Figure 7.4 Coil critical current, I_c measurement conducted from two stacks, respectively

7.4.2 Current distribution measurement setups

Considering the coupling between tapes in a stack and the current shift for every turn of the coil, the current distribution is measured at both terminals of the coil. The measurement is achieved using four identical current transducers highlighted in the red box in Figure 7.5. The transducer signals are observed and recorded through an oscilloscope. The transducers are always attached to the same tape to avoid extra errors produced during the measurement. First

of all, to check the coil coupling effects, the current distributions in four tapes are measured respectively at the same time. To achieve this, the tapes in each stack are split at the position between current feedthrough and the beginning of the coil winding position. The coil terminals are soldered to a copper plate to ensure the contact area of every tape is identical. The detailed tape current measurement set up is also shown in Figure 7.5. Similarly, the current distribution in each stack is measured. All possible positions of current transducers are implied in Figure 7.6.

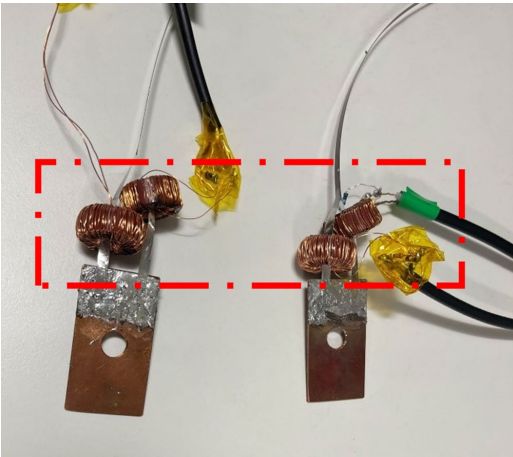


Figure 7.5 Current transducers for coil current distribution measurement

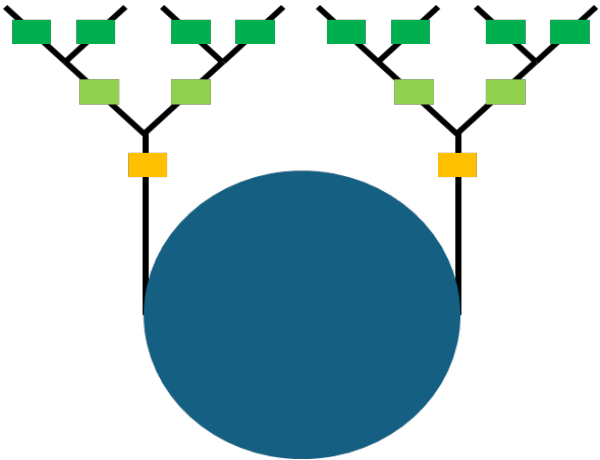


Figure 7.6 The possible positions of current transducers shown in coloured boxes

7.4.3 Inductance difference setups

It is known that in an AC circuit, when two inductors with different inductance values are connected in parallel, the current in each inductor is not the same. This is also true for coils with

two parallel paths having different inductance values. In this double stack structure, the inductance difference between two stacks is mainly caused by the length difference between these stacks.

To analyse this inductance difference impact between stacks on coil current distribution as well as the total transport current AC loss, two values of inductance difference are made. The first one is the original coil, and the second is the case of a bigger inductance difference achieved by increasing a half turn of the inner stack while also changing the length of the outer stack. The second case is shown in Figure 7.7, and the length changing of the outer stack is achieved by adding extra winding which is highlighted in the yellow box. The inductance values for the two cases are given in Table 7.2.

Table 7.2 Two cases of inductance difference between stacks

Coil inductance	Inner Stack S1	Outer Stack S2	Inductance Difference
original stack coil	199.4 μH	200.9 μH	1.5 μH
coil after inductance modification	208.6 μH	202.2 μH	6.4 μH

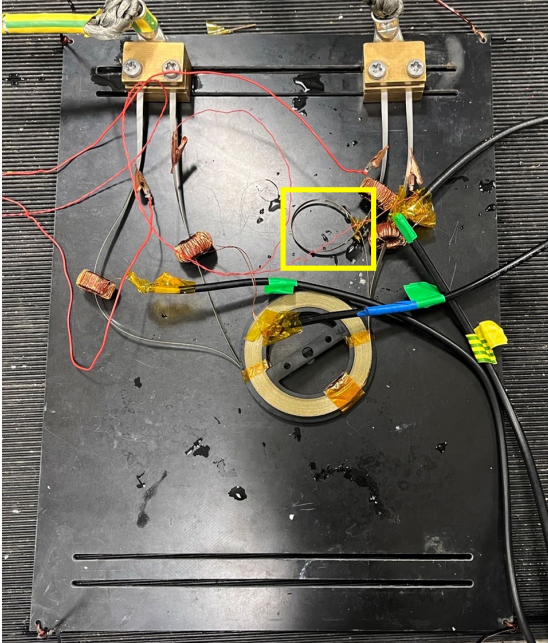


Figure 7.7 Coil with bigger inductance differences between stacks

7.4.4 AC loss measurement setups

The general electrical method [109, 123] as explained in Chapter 3 is used to measure the coil transport current AC loss. With the help of a data acquisition system (DAQ), the transient voltage and current across the coil are recorded for each measurement over several periods. Over n periods of time, the coil AC loss can be calculated by the integration as given in Equation 3.13.

Since the terminals of two stacks are not soldered together, the voltage tab can only measure the voltage across either inner or outer stack at one time. Therefore, the AC losses are measured twice for each case, from the inner and outer sides, respectively. The measurement is conducted at two frequencies, 50 Hz and 100 Hz, in the current range of 30–50 A_{rms} in 10 A_{rms} steps. The current below 30 A_{rms} is not considered as the input current noise component is great, and the current above 50 A_{rms} and the frequency above 100 Hz are not measured because of the power limitation of the amplifier. These two sets of measurements are repeated for the two values of inductance difference between inner and outer stacks to analyse the impact of inductance on the transport current AC loss.

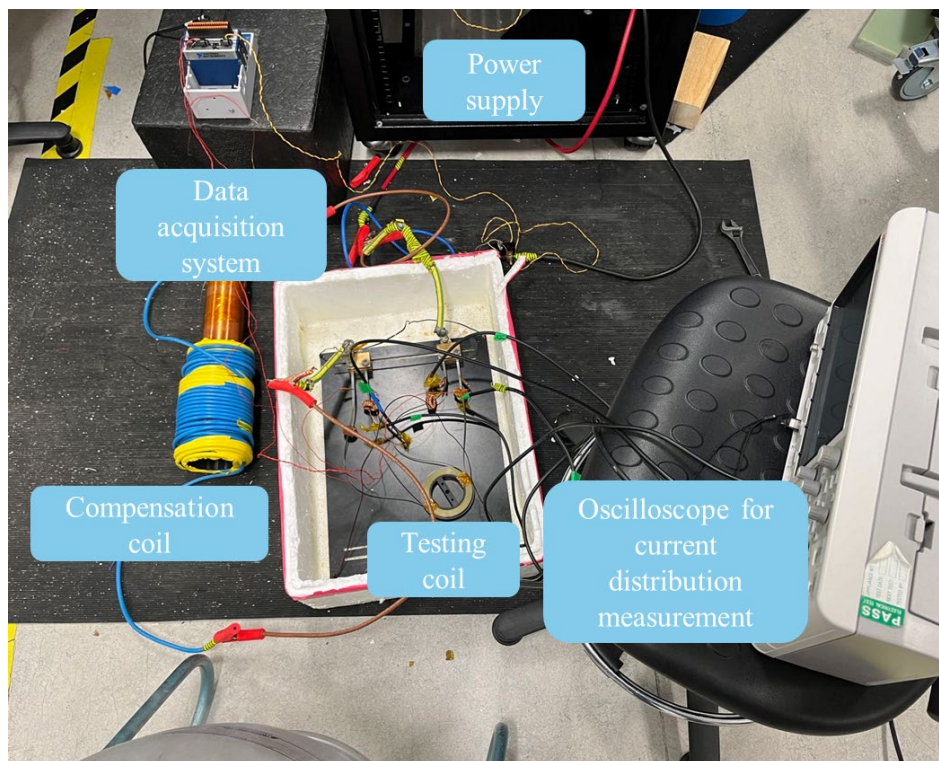


Figure 7.8 AC loss measurement setup

7.5 Measurement results and analysis

7.5.1 Proof of coupling

Initially, the coil coupling effect is investigated by measuring the tape current distribution. To figure out the relationships between the tape current distribution, stack current distribution and the total coil AC loss, and thus reduce the total AC loss, there are four scenarios proposed for double stack coil performance analysis. The scenarios are explained in the figures below followed by their results.

The green box indicates the position of the current transducer, while the white box indicates the circuit disconnection. We denote the tape currents according to their positions. The currents of tapes of the inner stack are named as I_{i1} and I_{i2} , and the currents of tapes of the outer stack are called I_{o1} and I_{o2} . Terminal 1 refers to the left side terminal while the right side terminal is terminal 2. The scenario with all tapes connected into the circuit is set as a reference scenario 0. The scenario 1 with only stack 1 connected into the circuit is set to identify the coupling impact within a stack. The second scenario has only one tape in each stack connected into the circuit, and it helps to analyse the coupling effects between stacks. The last scenario has connections from one tape from each stack on terminal 1 while all tapes are connected on terminal 2. The impacts of different ways of applying current on the coil current distribution are investigated by comparing the results of all three scenarios to the reference scenario 0.

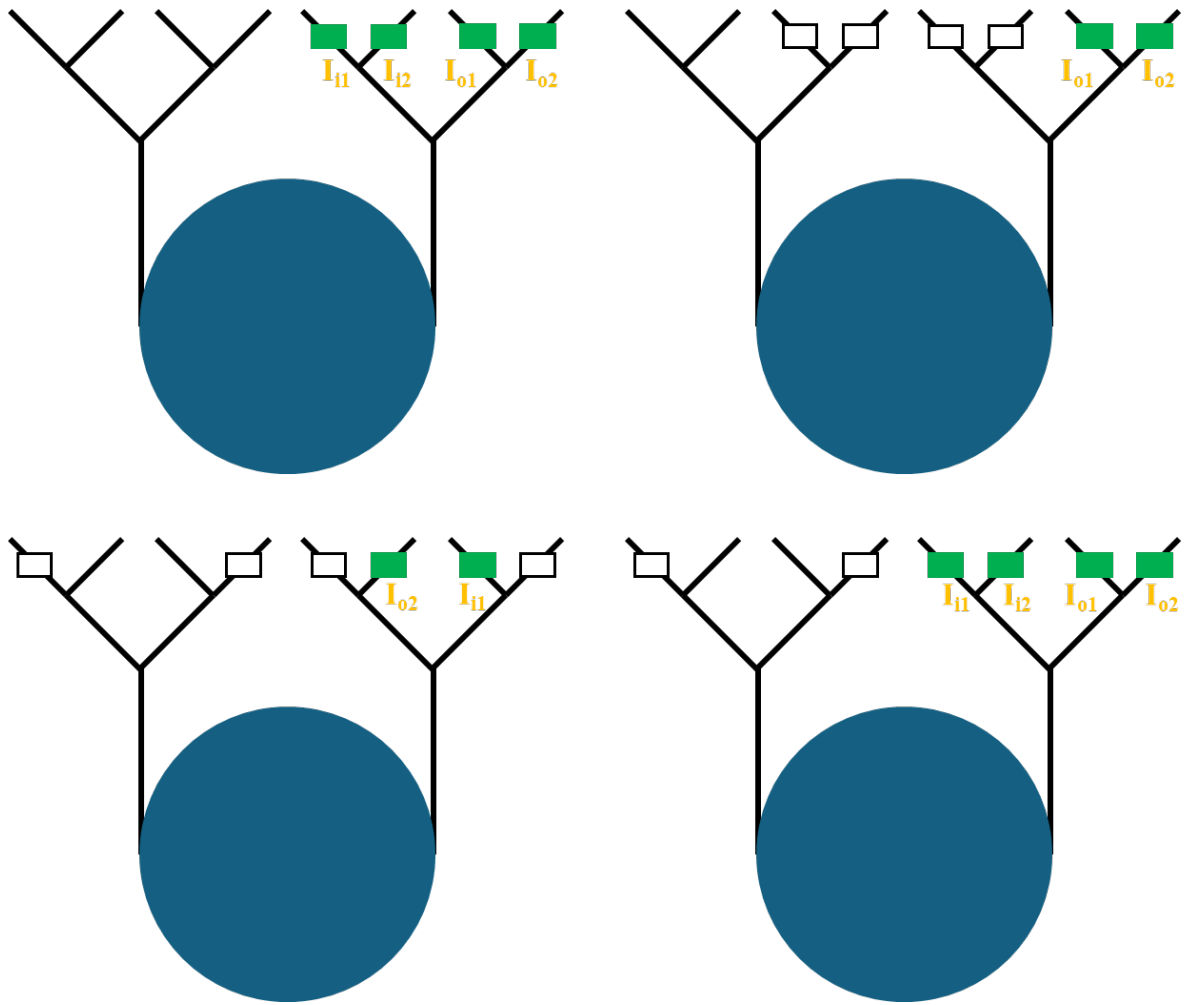
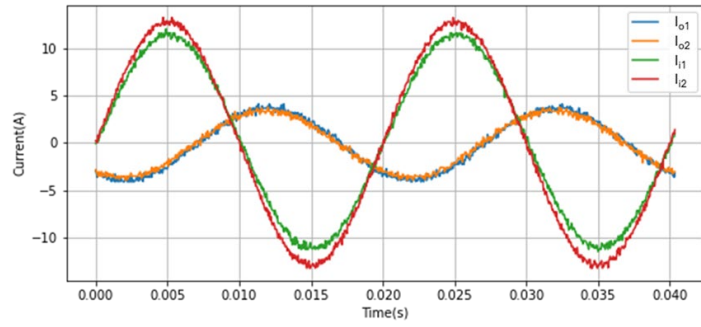
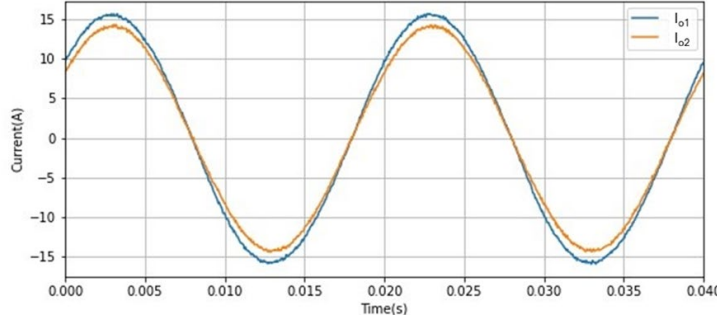


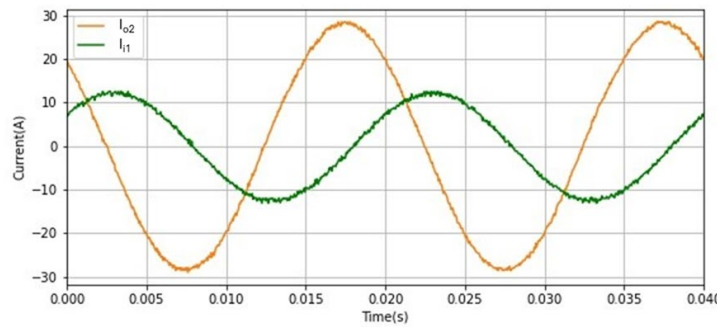
Figure 7.9 Coil coupling investigation tape current distribution circuits a) reference scenario 0: all tapes connected to the circuit; b) scenario 1: one stack connected to the circuit; c) scenario 2: one tape in each stack connected to the circuit 2; and d) scenario 3: one tape in each stack connected to terminal 1 and all stacks connected to terminal 2



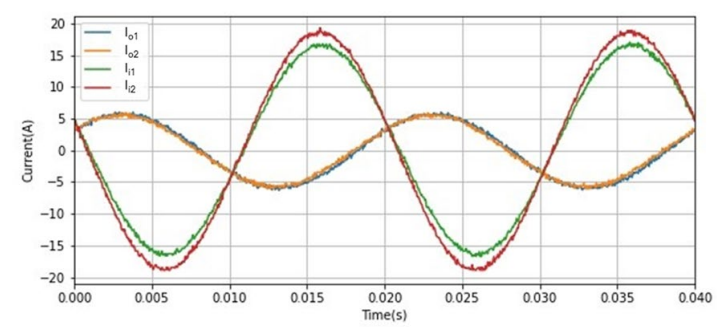
(a)



(b)



(c)



(d)

Figure 7.10 Coil coupling investigation tape current distribution results at 50 Hz with applied current of 30 A_{rms} a) reference scenario 0; b) scenario 1; c) scenario 2; and d) scenario 3

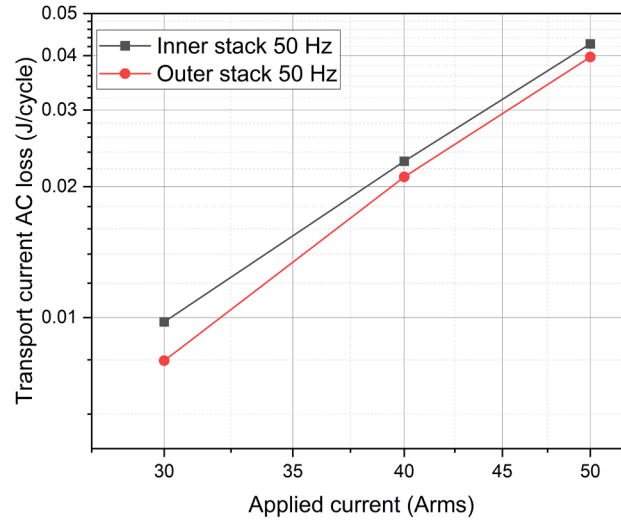
Regarding the results shown in Figure 7.10, all the scenarios show that the current distributions of two tapes in the same stack are the same regardless the method of applying current. However, there is a current phase shift between two stacks, and the current is not evenly distributed within each stack. One stack carries more current than the other which means that there will be extra current loop thus extra loss (mainly eddy current loss) introduced in soldering (metallic) layers. This phenomenon could be explained with the help of inductance difference in a circuit. As noticed in a circuit, the reactance component leads the angle difference between voltage and current. In this structure, the inner stack length is always shorter than that of the external stack, therefore, an inductance difference is introduced between two stacks. The inductance difference between two stacks, and thus the reactance difference, causes the current phase shift of these stacks.

In addition, regarding scenario 3, we found with only one tape in a stack connected to a circuit at terminal 1, both tapes in a stack carried same amount of current measured at terminal 2. The stack structure makes the tapes in a stack fully coupled. It indicates that there will be transverse current flowing between tapes in a stack, which will introduce extra coupling loss.

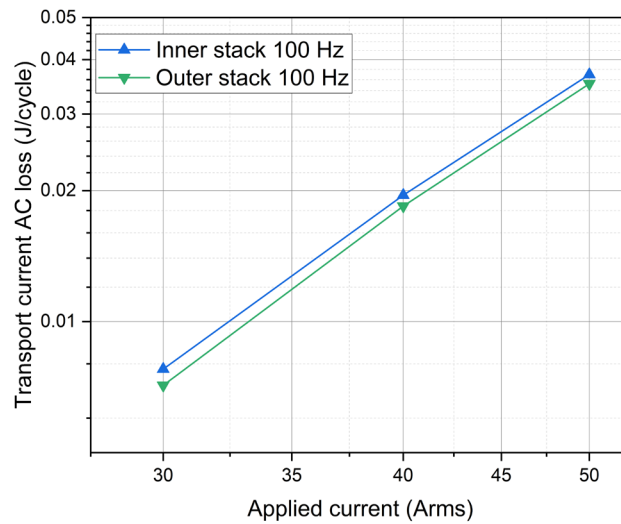
7.5.2 Coil AC loss Analysis

7.5.2.1 Original coil AC loss

Since the two stacks are separated attached to the current lead, the compensation coil used in electric measurement could only be connected to either the inner or outer stack at one time. The transport current AC loss measurement results with the compensation coil connected to the inner and outer stacks, respectively, are given in Figure 7.11. It is shown that the loss measured from the outer stack compensation case is always slightly smaller than that of the inner stack compensation case. Since the two stacks are connected in parallel in the circuit, which indicates the same voltage drop, the loss difference could result in uneven current distribution between the two stacks.



a)



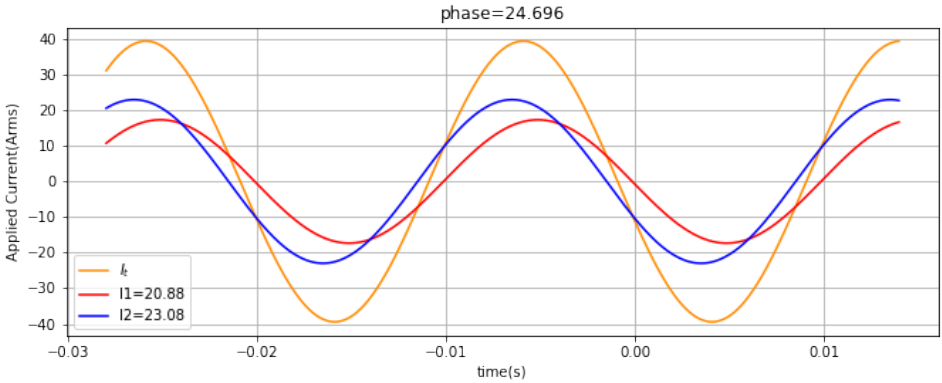
b)

Figure 7.11 Transport current AC loss measurements comparison with compensation coil connected to inner and outer stack respectively at a) 50 Hz; and b) 100 Hz

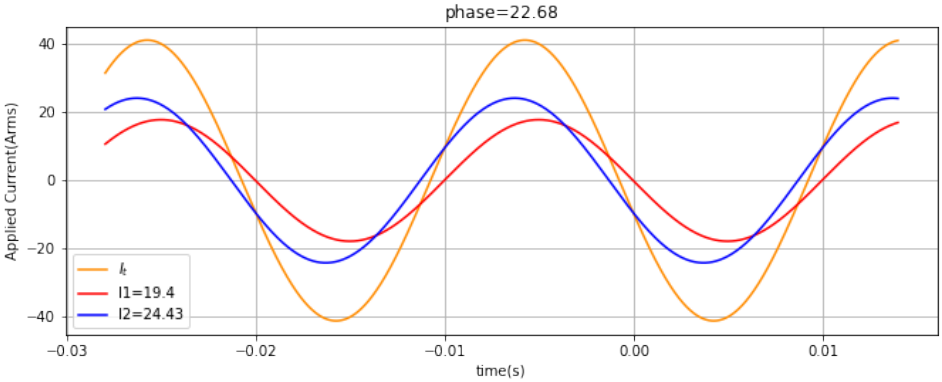
Hence, the current distribution of each stack is measured. The current in the outer stack is assigned as I_1 , the current in the inner stack is assigned as I_2 , and the total current applied to the coil is assigned as I_t . The current amplitude in each stack for an example case of applying 30 A_{rms} at 50 Hz is given in the figure below. The current distribution is measured twice for the two compensation cases.

The results imply that the inner stack carries a higher amount of current. Since the voltage measured after compensation subtraction is proportional to the current, when the current in the

circuit is higher, the voltage measured is higher, thus the loss measured becomes higher. Therefore, the loss measured from the inner stack compensation case is always slightly higher. However, since the current difference between the two stacks is small, the loss difference in the measurement is small enough to be neglected.



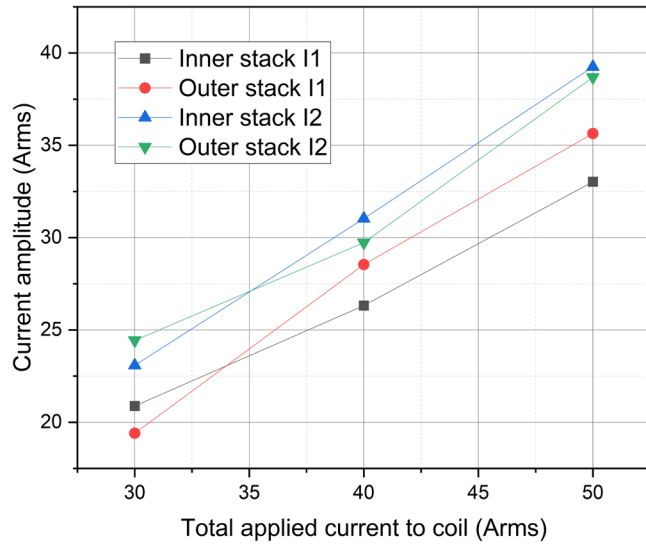
a)



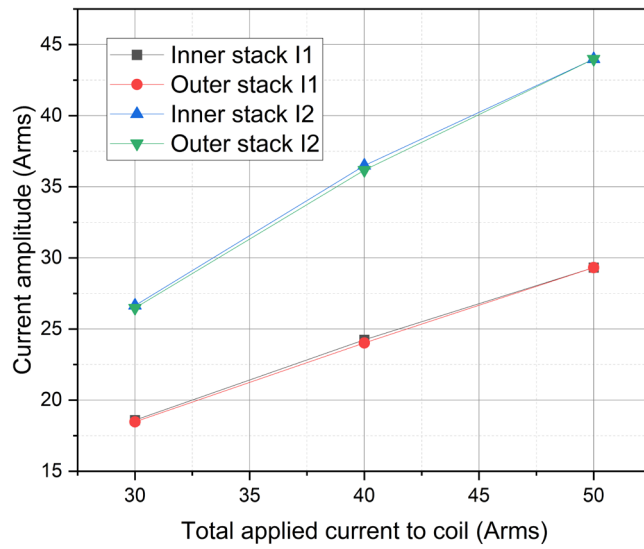
b)

Figure 7.12 Current distribution of two stacks at 50 Hz, 30 A_{rms} a) inner stack compensation case; and b) outer stack compensation case

To further investigate the possible factors that affect the current distribution and thus the coil loss, the currents of two stacks are measured from the inner and outer compensation cases at both 50 Hz and 100 Hz. The current amplitude for each stack and the current phase differences between stacks are given in the following figures.



a)



b)

Figure 7.13 Current amplitude in each stack comparison with compensation coil connected to inner and outer stack respectively a) at 50 Hz; and b) 100 Hz

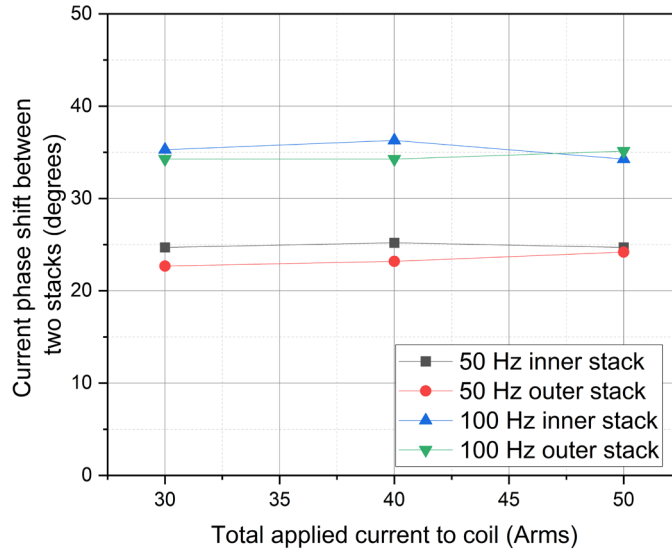


Figure 7.14 Current phase shift measurement comparison between two stacks at 50 Hz and 100 Hz with compensation coil connected to inner and outer stack, respectively

First of all, the connection of the compensation coil to either the inner or outer stack as well as the applied current amplitude has no obvious impact on the stack current performance. Regarding Figure 7.13, it is notable that the current amplitude measurement result is more consistent at 100 Hz. Meanwhile, as shown in Figure 7.14, the current distribution phase shift between two stacks is stable when increasing the applied current, while it increases as the working frequency increases. This is reasonable as the coil impedance is frequency dependent.

If we assigned the current amplitude difference between stacks as:

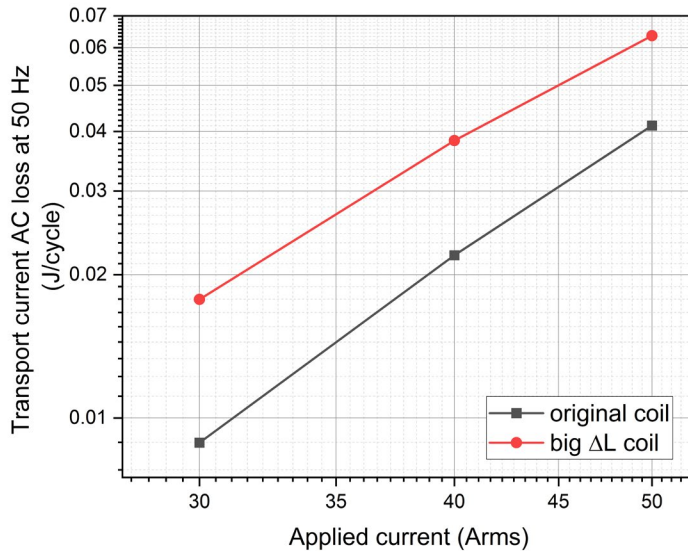
$$\Delta I = I_{inner} - I_{outer} \quad (7.1)$$

it shows that at 100 Hz, ΔI is bigger, and the current phase shift is greater.

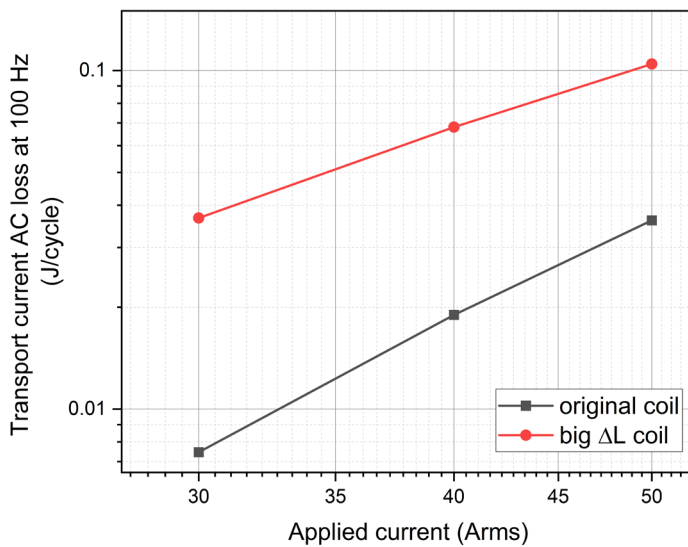
7.5.2.2 Inductance difference impact on AC loss

The same measurement of coil transport current AC loss, as well as current distribution is conducted again after adding more stack inductance differences as described in Section 7.4.3.

The two inductance difference cases are named the original coil and bigger ΔL coil respectively here.



a)



b)

Figure 7.15 Transport current AC loss comparison between original coil and coil with bigger ΔL at a) 50 Hz; and b) 100 Hz

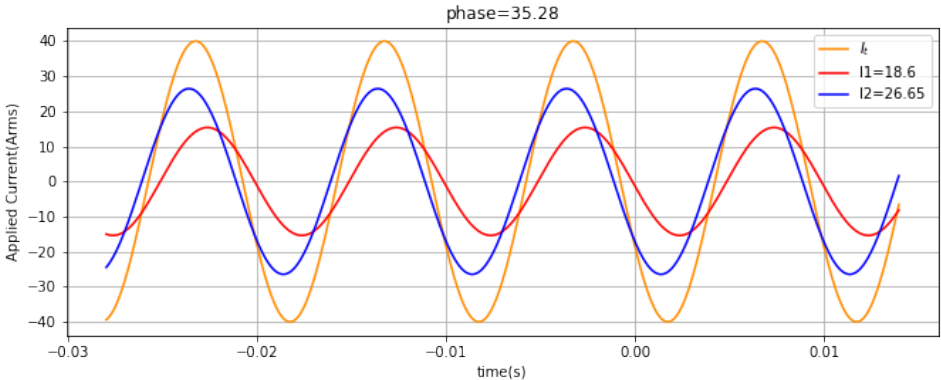
The loss for the coil with bigger ΔL is about twice that of the original small ΔL case for both frequencies. It's obvious that for the bigger ΔL case, the loss is much higher at 100 Hz. This phenomenon could be explained according to the following tape current distribution results. By increasing the inductance difference from 1.5 μH to 6.4 μH , the current phase shift increases dramatically from under 45 degrees to above 140 degrees. The current relation between two stacks varies gradually from the in-phase condition to the out-of-phase condition. Taking the

30 A_{rms} and 100 Hz case as an example, as shown in Figure 7.16 a), the current amplitudes of the two stacks are similar and below the total applied current, I_t when the ΔL is small; while as shown in Figure 7.16 b), the current amplitudes of the two stacks are quite different and much greater than the total applied current, I_t, when ΔL is big.

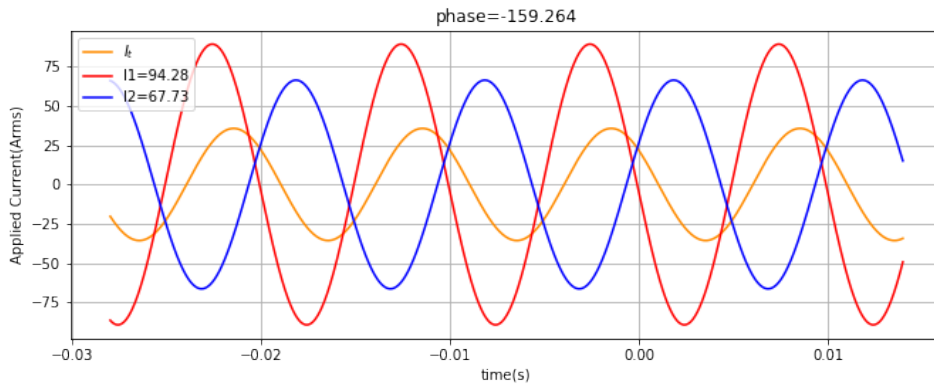
Though the inductance difference modification is achieved by adding an extra length of tape to each stack, the length is small enough to be neglected to contribute to the total amount of AC loss. Considering the tape current is much higher in each stack when ΔL is big, the eddy current introduced in the metallic layer is much higher as well. The eddy current loss is frequency dependent. Hence, for the big ΔL case, eddy current loss is the dominant contribution to the total transport current loss. This is further explained with the help of simulation in Section 7.6.

Table 7.3 Average stack current phase shift

	average phase shift (degrees)	
	original coil	bigger ΔL coil
50 Hz	25	142
100 Hz	35	162



a)

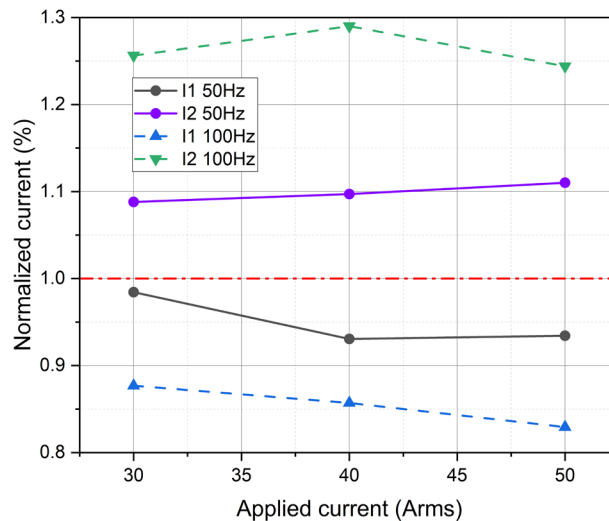


b)

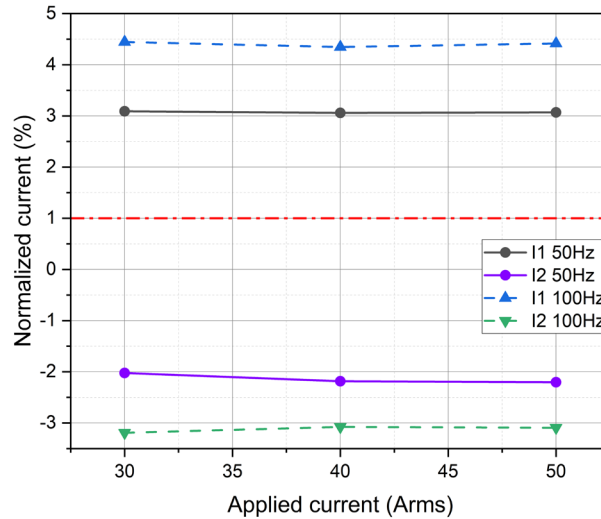
Figure 7.16 Current distribution of two stacks at 100 Hz, 30 A_{rms} a) original coil case; and b) bigger ΔL coil case

The current amplitude trend in each stack is also given in Figure 7.17. The reference line marked in red is set as each stack carries the same amount of current (50% of total I_{app}) to help show the stack current difference. The out-of-phase current impact is also considered in the bigger ΔL case.

The stack current amplitude difference becomes greater when increasing the working frequency. When increasing the stack inductance difference, the stack current phase shift increases thus the amplitude could be 2 to 4.5 times higher than the real applied current. To minimize the coil AC loss, the inductance difference should be kept as small as possible.



a)



b)

Figure 7.17 Normalized stack current with respect to half I_{app} (A_{rms}) a) original coil; and b) bigger ΔL case considering out-of-phase current impact

7.6 Coil AC loss simulations

7.6.1 Simulation methodologies

To describe the electromagnetic properties, simulations were conducted using FEM with the 2D axis-symmetrical H-formulation, which is explained and validated in Section 3.5.5.

The magnetic field dependency of the superconductor critical current density, $J_c(B)$, is taken from interpolation obtained from measurement of same tape samples. As shown in Figure 7.18, the stack consists of two HTS tapes (black) with soldering layer around (orange), and these stacks are insulated from each other (violet). The constraints for the current applied were defined so the total applied current has to be equal to the integral of the current density along the whole turn. The soldering resistivity is set to be $2.33 \cdot 10^{-9} \Omega m$ regarding the copper resistivity at 77 K [130] and the current for each tape is obtained directly from the measurement.

Though the loss (mainly hysteresis loss) in the HTS tapes is calculated with the help of the current constraints, the 2D axis-symmetrical modelling has its limitation: in general, in this 2D axisymmetric model, current transfer along the r-axis is neglected. As a result, there is an ignorance of coupling loss (between tapes) and inaccurate estimation of eddy current loss in the metallic soldering layer. Therefore, there is an AC loss difference between simulation and measurement for this stack structure.

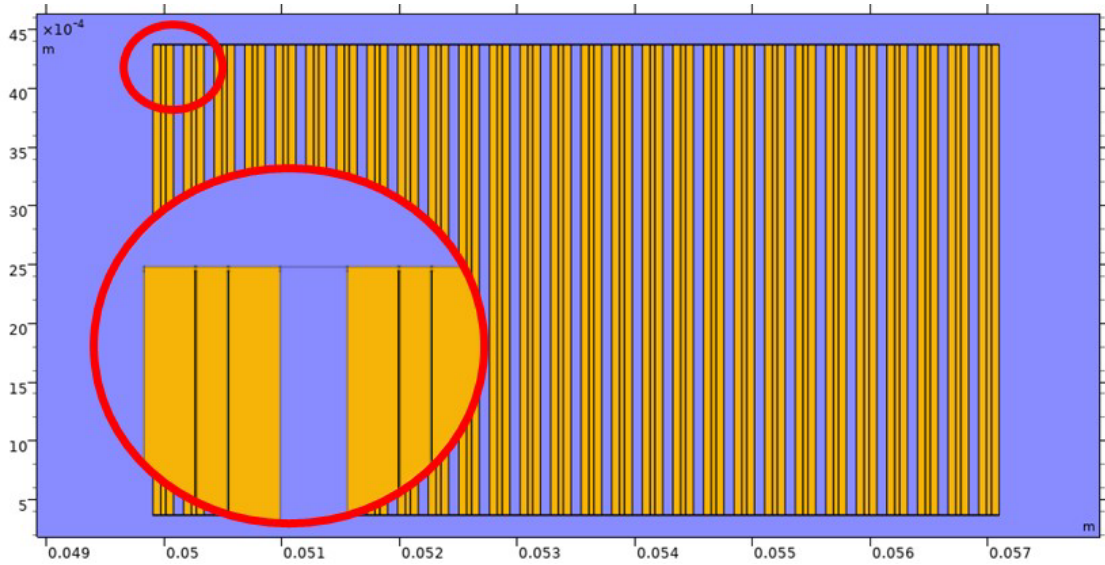


Figure 7.18 Double stack coil geometry in 2d axis-symmetrical model

7.6.2 Coil AC loss results

To figure out the impact of big stack inductance differences on the eddy current loss, the coil transport current AC loss simulation results of the bigger ΔL case are given in the figure below in comparison with the electric measurement results. As the eddy current loss is incorrect in the soldering layer due to the ignorance of the transverse current, only the tape hysteresis loss results are plotted. For the denotations, tape hysteresis loss from the simulation is written as 'simu tape' and the measurement results using the electric method are written as 'electric'.

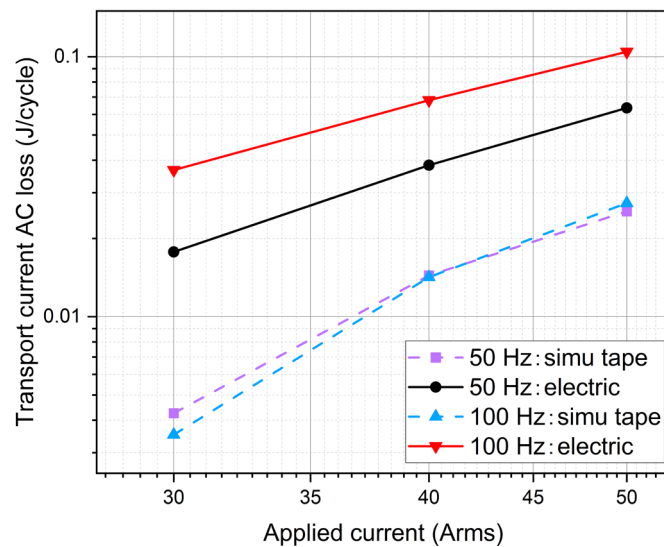
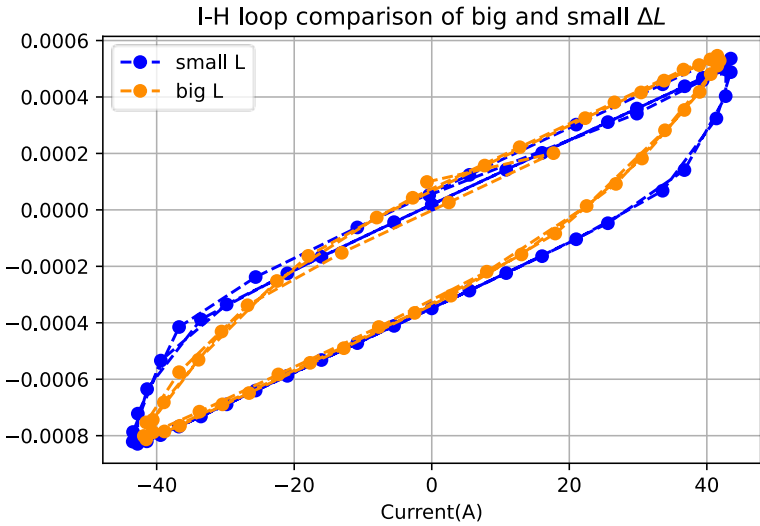


Figure 7.19 AC loss comparison between simulation and electric measurements of bigger ΔL case

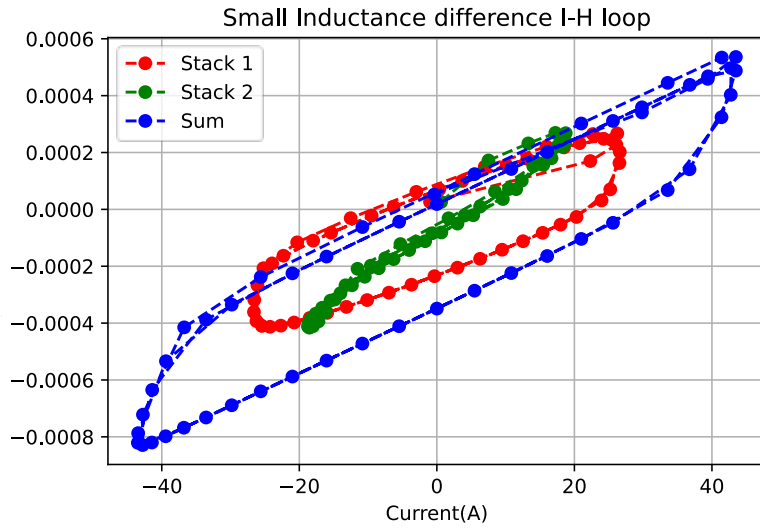
Tape loss, mainly hysteresis, is frequency-independent, hence for the simulation results shown by dashed lines, tape losses are stable at both frequencies. Tape hysteresis loss is lower than the total measured transport current loss. The difference refers to the soldering loss. With bigger inductance difference, the total measured transport current loss shows obvious frequency dependence. It indicates that the induced eddy current loss in the soldering layer overweighs the tape hysteresis loss when the ΔL is big.

7.6.3 Coil magnetic energy analysis

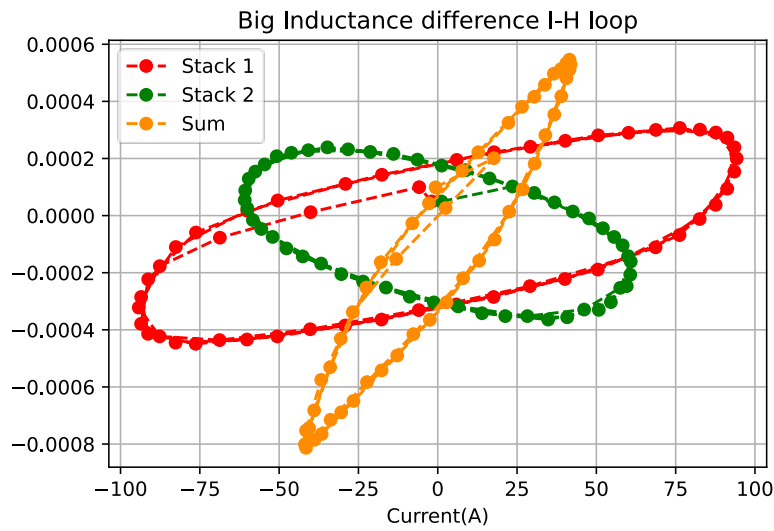
Previously, we noticed that for the bigger ΔL case, the current in each stack is much higher than the real applied current. Since HTS coils perform inductively, it is worth analysing how the transient magnetic energy performs in the coil. In general, a hysteresis loop is used to check the magnetic performance. In this specific case, since the field is generated by the coil applied current, an I-H loop is used to present the hysteresis performance here. The I-H loop results are given in Figure 7.20. The overall hysteresis loop for the two coil cases are similar as shown in Figure 7.20 a), since the total applied current is the same. While due to the difference stack current distribution, the I-H loop for each stack performs quite differently. The higher the stack current, the bigger the I-H loop, meanwhile, the I-H loop shows the same trend when the stack current phase difference is small while it shows the opposite trend when the stack current phase difference is big and close to 180 degrees.



a)



b)



c)

Figure 7.20 Hysteresis I-H loop of a) overall big and small ΔL cases; b) two stacks of small ΔL case; and c) two stacks of big ΔL case

For further analysis, the transient magnetic energy is calculated. The magnetic energy stored in the stack coil could be described as:

$$E_m = \frac{1}{2}L_1I_1^2 + \frac{1}{2}L_2I_2^2 + MI_1I_2 \quad (7.2)$$

where L_1 and L_2 are the inductance of two stacks and M is the mutual inductance, and considering the slotless structure, the mutual inductance impact could be ignored. As illustrated in Figure 7.21, the transient magnetic energy storage in the coil with bigger ΔL is about 10 times higher as the current in each stack is much higher. Therefore, beyond the extra high

transport current loss in tapes, there is also much higher transient magnetic energy stored in the coil when the coil has bigger ΔL between stacks.

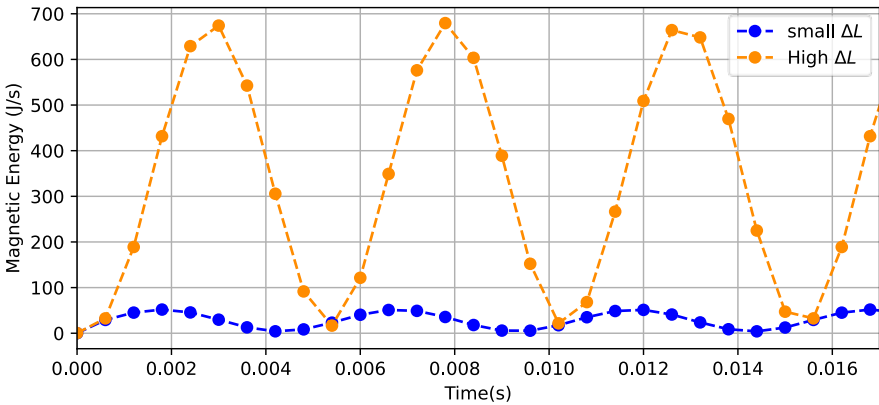


Figure 7.21 Transient magnetic energy comparison between small and big ΔL cases

7.7 Conclusion

In this chapter, the stacked structure HTS armature coil was proposed and developed to increase armature current capacity thus meeting the electrical loading and power density requirements for future electric propulsion systems, particularly in electric aviation.

In this research, a stacked coil structure is proposed to improve the electrical loading capabilities of superconducting machines. By stacking HTS tapes in parallel within the coil structure, the current capacity of the armature is significantly enhanced, while reducing the overall coil inductance. The reduction in inductance not only enables faster current response, but also improves the overall operating efficiency of the machine, making it more suitable for aerospace applications. In addition, the conventional way of putting coil phase groups in parallel is not applicable for HTS stator design. This is because the HTS tape is mechanically fragile and the bending radius is big, and it requires uniformly thermal cooling to avoid local quench. To enhance the mechanical stability and thermal robustness of the stack coils, metallic soldering layers are introduced.

However, one of the key challenges found in this study is the extra AC losses introduced in the coil by the soldering structure. The study accurately measured the current distribution within the stacks, indicating that inductance difference between the inner and outer stacks contributes to uneven current distribution, which further increases the total AC loss of the coil.

This study investigates the effect of inductance differences on the current distribution and transport current AC loss characteristics of stacked coils by combining experimental measurements with numerical simulations. It was found that increasing the inductance difference between the stacks significantly affects the current phase shift and the current amplitude flowing through the stacks, resulting in a dramatic increase in total transport current AC losses. In particular, the inductance difference increase modification resulted in a phase shift of up to 160 degrees between stacks, which in turn caused the current amplitudes of stacks to exceed the total applied current by a factor of 2 to 4.5 times. In addition to extra AC loss generation, this uneven current distribution will also affect the torque produced in a machine. This uneven current distribution can make axisymmetric field, cause local magnetic field distortion thus resulting in a torque ripple. These effects highlight the importance of minimizing inductance differences between stacks within the coil to reduce losses and improve performance.

The findings also demonstrated that the transport current AC losses at higher frequencies (100 Hz) were much bigger than at lower frequencies (50 Hz) for coils with greater inductance differences. This phenomenon might be due to the increased current phase shift and the corresponding rise in soldering losses.

In addition to the experimental measurements, a 2D axis-symmetrical model was developed to simulate and understand the behaviour of the stack coils under an AC transport current. While the simulations provided understanding into the electromagnetic behaviour of the coils, they were found to inaccurately estimate the total AC losses due to the exclusion of transverse current within a stack. Despite this limitation, the model helps to understand the coil behaviour from a magnetic energy perspective.

Overall, this study highlights the need for further optimization of stack coil designs to minimize transport current AC losses and improve the overall efficiency of superconducting machines. This includes reducing inductance differences between stacks and improving the coil design to mitigate coupling effects. In addition, the coil needs to be tested under a background field to show stable performance under a real machine environment. It will be critical to continue developing more accurate simulation models that account for all relevant loss mechanisms, including transverse currents, coupling losses and eddy current loss.

In conclusion, the multi-stack HTS armature design represents a significant step in the development of superconducting machines for electric propulsion. The results of this study help

to gain a deeper understanding of the transport current AC loss characteristics of stacked HTS coils and provide practical recommendations for optimizing their performance, especially reducing transport current AC loss.

Chapter 8 Conclusion

8.1 Thesis summary

This thesis has presented a study of HTS armature coils for superconducting motors used in electric propulsion applications which will provide the high power density requirement for future electric aircraft. There are two main issues discussed in this study: evaluation of the potential of using HTS coils as motor armatures, and HTS coil AC loss estimation and reduction.

Chapter 1 provided a comprehensive overview of electric propulsion systems, underscoring the importance of transitioning from traditional fossil-fuel-based systems to More Electric Aircraft (MEA) and All Electric Aircraft (AEA) solutions. Key developments in superconductivity were introduced, emphasizing their relevance for achieving the power density requirements requirement for MEA/AEA. This chapter also presented the current existing HTS motor topologies for electric aircraft, and their potential design challenges.

Chapter 2 reviewed superconducting motor technologies, outlining the advantages of HTS in achieving higher power densities, which is critical for aerospace applications. This was followed by the AC loss mechanisms necessary for understanding HTS performance in electric motors. The chapter reviewed the AC loss types in type II superconductors: hysteresis, coupling, eddy currents, and ferromagnetic losses. It also discussed the technical importance of AC loss to HTS propulsion motors.

Chapter 3 summarized all the general methodologies used for the AC loss evaluation for HTS materials. They included analytical methods, numerical modelling techniques and experimental methods. A numerical modelling validation was given here.

Chapter 4 evaluated the potentials of using HTS as armature windings compared to different conventional stator windings, especially a Litz wire structure using copper and aluminium according to different power levels, focusing on radial flux motor designs for electric aircraft. Two motor benchmarks of 450 kW and 1 MW were examined, analysing the impact of the iron core and the stator AC losses across various winding materials. Under MW level at cryogenic temperatures below the LN₂ temperature, HTS coils outperformed Litz copper/aluminium windings in reducing AC losses and improving PTW.

Chapter 5 provided an evaluation of transport current AC losses in standard 2G HTS insulated coils. At the beginning, this chapter explained the structure of the tested standard 2G HTS insulated coils, which was used in model validation in Section 3.5.5. Then the coil transport current AC losses were estimated considering a real machine environment: different applied currents and their harmonics, the cryogenic working temperatures and the working frequencies. The findings of transport current AC loss in HTS coils in this chapter helped to assess the performance of HTS armature windings in the following chapters.

Chapter 6 explored the HTS armature coils within radial flux synchronous motors, assessing their performance under different magnetic loadings from partially PM-HTS motors to fully HTS motors. The findings pointed out possible methods for reducing HTS coil AC loss by narrowing the HTS tape width or introducing a thin back iron layer to the stator. The results of these simulations provided a foundation for optimizing HTS coil design in high PTW motors.

Chapter 7 introduced a new HTS coil structure. To address challenges in HTS coil design, a new multi-stack structure was proposed and tested. The chapter explained the coil design, winding layout, and transport current AC loss measurement at 77 K. Experimental testing confirmed that the multi-stack structure could improve current-carrying capacity, as well as maintaining thermal and mechanical stability. The loss components were analysed with the help of a 2D axisymmetric model using the H-formulation. The extra loss introduced by this soldering structure could be minimized by balancing the inductance between stacks connected in parallel.

8.2 Future work

In terms of HTS coil AC loss measurements, most of the experiments conducted in this research were transport current loss measurements using the electrical method. However, in a real world machine condition, HTS stator coils suffer from both high AC current and a rotating magnetic field at the same time. It is necessary to carry out AC loss measurements under both conditions at the same time in the future. In addition, as indicated in Chapter 4, the HTS stator coil outperforms other types of windings when the working temperature is within LH₂ temperatures (30–40 K preferred). It is important to test a coil under such cryogenic conditions. Considering the testing complexity, the calorimetric method could be used. Testing at these temperatures can guide design modifications to achieve a desired balance between cooling requirements and

AC loss reduction. The same studies need to also be conducted for the new multi-stack coil proposed in Chapter 7.

Regarding simulations, the methodology for standard 2G HTS insulated coils is sufficiently mature. However, it requires improvement for a stacked structure coil. For example, rather than measuring the tape current directly, either a 2D T-A formulation considering resistivity for different layers or coupling electrical circuits could be used to predict the tape current distribution.

Reference

- [1] A. Boglietti, A. Cavagnino, A. Tenconi, S. Vaschetto, and P. d. Torino, "The safety critical electric machines and drives in the more electric aircraft: A survey," in *2009 35th Annual Conference of IEEE Industrial Electronics*, 3-5 Nov. 2009 2009, pp. 2587-2594, doi: 10.1109/IECON.2009.5415238.
- [2] E. E. Agency, "Trends and projections in Europe 2023," 24 Oct 2023 2023.
- [3] H. Ritchie, "What share of global CO₂ emissions come from aviation?," *Our World in Data*, 2024. [Online]. Available: <https://ourworldindata.org/global-aviation-emissions>.
- [4] R. M. A. G. P. Peters. *The Global Carbon Project's fossil CO₂ emissions dataset*, doi: 10.5281/zenodo.7215364.
- [5] S. Gössling and A. Humpe, "The global scale, distribution and growth of aviation: Implications for climate change," *Global Environmental Change*, vol. 65, p. 102194, 2020/11/01/ 2020, doi: <https://doi.org/10.1016/j.gloenvcha.2020.102194>.
- [6] D. S. Lee *et al.*, "The contribution of global aviation to anthropogenic climate forcing for 2000 to 2018," *Atmospheric Environment*, Journal Article vol. 244, 2021, doi: <https://doi.org/10.1016/j.atmosenv.2020.117834>.
- [7] Y. Wang, C. Zhang, C. Zhang, and L. Li, "Review of High-Power-Density and Fault-Tolerant Design of Propulsion Motors for Electric Aircraft," *Energies*, vol. 16, no. 19, p. 7015, 2023. [Online]. Available: <https://www.mdpi.com/1996-1073/16/19/7015>.
- [8] A. T. A. Group, "Aviation: Benefits Beyond Borders global report," 2020.09.30 2020. [Online]. Available: <https://aviationbenefits.org/downloads/aviation-benefits-beyond-borders-2020/>
- [9] B. Srimoolanathan, "Aircraft electrical power systems—Charged with opportunities," *Aerospace and Defense Executive Briefing of Frost & Sullivan*, 2008.
- [10] E. J. Adler and J. R. R. A. Martins, "Hydrogen-powered aircraft: Fundamental concepts, key technologies, and environmental impacts," *Progress in Aerospace Sciences*, vol. 141, p. 100922, 2023/08/01/ 2023, doi: <https://doi.org/10.1016/j.paerosci.2023.100922>.
- [11] A. T. Institute, "Insight electrical power systems," ed, 2018.
- [12] G. J. Atkinson, B. C. Mecrow, A. G. Jack, D. J. Atkinson, P. Sangha, and M. Benarous, "The Analysis of Losses in High-Power Fault-Tolerant Machines for Aerospace Applications," *IEEE Transactions on Industry Applications*, vol. 42, no. 5, pp. 1162-1170, 2006, doi: 10.1109/TIA.2006.880869.
- [13] W. Cao, B. C. Mecrow, G. J. Atkinson, J. W. Bennett, and D. J. Atkinson, "Overview of Electric Motor Technologies Used for More Electric Aircraft (MEA)," *IEEE Transactions on Industrial Electronics*, vol. 59, no. 9, pp. 3523-3531, 2012, doi: 10.1109/TIE.2011.2165453.
- [14] J. A. Rosero, J. A. Ortega, E. Aldabas, and L. Romeral, "Moving towards a more electric aircraft," *IEEE Aerospace and Electronic Systems Magazine*, vol. 22, no. 3, pp. 3-9, 2007, doi: 10.1109/MAES.2007.340500.
- [15] E. National Academies of Sciences and Medicine, *Commercial Aircraft Propulsion and Energy Systems Research: Reducing Global Carbon Emissions*. Washington, DC: The National Academies Press (in English), 2016, p. 122.
- [16] C. Degoutte, O. Sanchez, J. Renaudin, N. Boukari, P. Decroux, and J. D. Salvany, "Aircraft 270VDC power distribution improvements using wide band gap semi-conductors," in *2016 International Conference on Electrical Systems for Aircraft*,

- Railway, Ship Propulsion and Road Vehicles & International Transportation Electrification Conference (ESARS-ITEC)*, 2-4 Nov. 2016 2016, pp. 1-6, doi: 10.1109/ESARS-ITEC.2016.7841357.
- [17] C. A. a. M. P. J. a. N. T. a. M. D. a. K. H. D. a. B. G. V. a. W. M. a. H. D. Luongo, "Next Generation More-Electric Aircraft: A Potential Application for HTS Superconductors," *IEEE Transactions on Applied Superconductivity*, vol. 19, no. 3, pp. 1055-1068, 2009, doi: 10.1109/TASC.2009.2019021.
- [18] P. Wheeler and S. Bozhko, "The more electric aircraft: Technology and challenges," *IEEE Electrification Magazine*, Article vol. 2, no. 4, pp. 6-12, 2014, Art no. 7008830, doi: 10.1109/MELE.2014.2360720.
- [19] M. Filipenko *et al.*, "Concept design of a high power superconducting generator for future hybrid-electric aircraft," *Superconductor Science and Technology*, vol. 33, no. 5, p. 054002, 2020/03/16 2020, doi: 10.1088/1361-6668/ab695a.
- [20] Y. Terao, W. Kong, H. Ohsaki, H. Oyori, and N. Morioka, "Electromagnetic Design of Superconducting Synchronous Motors for Electric Aircraft Propulsion," *IEEE Transactions on Applied Superconductivity*, vol. 28, no. 4, pp. 1-5, 2018, doi: 10.1109/TASC.2018.2823503.
- [21] T. Yang, F. Gao, S. Bozhko, and P. Wheeler, "Chapter 24 - Power Electronic Systems for Aircraft," in *Control of Power Electronic Converters and Systems*, F. Blaabjerg Ed.: Academic Press, 2018, pp. 333-368.
- [22] H. Lin, H. Guo, and H. Qian, "Design of High-Performance Permanent Magnet Synchronous Motor for Electric Aircraft Propulsion," in *2018 21st International Conference on Electrical Machines and Systems (ICEMS)*, 7-10 Oct. 2018 2018, pp. 174-179, doi: 10.23919/ICEMS.2018.8549030.
- [23] S. Fang, Y. Wang, and H. Liu, "Design study of an aerospace motor for more electric aircraft," *IET Electric Power Applications*, vol. 14, no. 14, pp. 2881-2890, 2020/12/23 2020, doi: 10.1049/iet-epa.2020.0507.
- [24] T. F. T. A. D. A. M. G. G. J. M. Gutknecht, "Analytical Design and Performance Estimation Methods for Aircraft Permanent Magnet Synchronous Machines," Technical Memorandum (TM) E-20151, September 1, 2023 2023. [Online]. Available: <https://www.sti.nasa.gov/>
- [25] M. Corduan, M. Boll, R. Bause, M. P. Oomen, M. Filipenko, and M. Noe, "Topology Comparison of Superconducting AC Machines for Hybrid Electric Aircraft," *IEEE Transactions on Applied Superconductivity*, vol. 30, no. 2, pp. 1-10, 2020, doi: 10.1109/TASC.2019.2963396.
- [26] P. J. Masson and C. A. Luongo, "High power density superconducting motor for all-electric aircraft propulsion," *IEEE Transactions on Applied Superconductivity*, vol. 15, no. 2, pp. 2226-2229, 2005, doi: 10.1109/TASC.2005.849618.
- [27] M. I. Sandy Smith, C. Manolopoulos, S.M. Husband, P.R. Miller, & P. Tuohy, "Design Of Superconducting AC Propulsion Motors For Hybrid Electric Aerospace," ed, 2018.
- [28] C. D. Manolopoulos, M. F. Iacchetti, A. C. Smith, K. Berger, M. Husband, and P. Miller, "Stator Design and Performance of Superconducting Motors for Aerospace Electric Propulsion Systems," *IEEE Transactions on Applied Superconductivity*, vol. 28, no. 4, pp. 1-5, 2018, doi: 10.1109/TASC.2018.2814742.
- [29] P. Tixador and H. Daffix, "Conceptual design of an electrical machine with both low and high T/sub c/ superconductors," *IEEE Transactions on Applied Superconductivity*, vol. 7, no. 4, pp. 3858-3865, 1997, doi: 10.1109/77.659439.

- [30] Y. Terao, S. Okumura, and H. Ohsaki, "Study on Electric and Magnetic Loadings in Fully Superconducting Motor Design," *Physica C: Superconductivity and its Applications*, vol. 617, p. 1354399, 2024/02/15/ 2024, doi: <https://doi.org/10.1016/j.physc.2023.1354399>.
- [31] "Electric propulsion components with high power densities for aviation," in *Transformative Vertical Flight Workshop*, 2015. [Online]. Available: <https://nari.arc.nasa.gov/sites/default/files/attachments/Korbinian-TVFW-Aug2015.pdf>. [Online]. Available: <https://nari.arc.nasa.gov/sites/default/files/attachments/Korbinian-TVFW-Aug2015.pdf>
- [32] A. El-Refaie and M. Osama, "High specific power electrical machines: A system perspective," *CES Transactions on Electrical Machines and Systems*, vol. 3, no. 1, pp. 88-93, 2019, doi: 10.30941/CESTEMS.2019.00012.
- [33] R. H. Jansen *et al.*, "High Efficiency Megawatt Motor Preliminary Design," in *2019 AIAA/IEEE Electric Aircraft Technologies Symposium (EATS)*, 22-24 Aug. 2019 2019, pp. 1-13, doi: 10.2514/6.2019-4513.
- [34] A. R. P. A.-E. (ARPA-E). "ASCEND Project Descriptions." https://arpa-e.energy.gov/sites/default/files/2025-01/Project%20Descriptions_ASCEND.pdf (accessed 2025).
- [35] F. Grilli *et al.*, "Superconducting motors for aircraft propulsion: the Advanced Superconducting Motor Experimental Demonstrator project," *Journal of Physics: Conference Series*, vol. 1590, no. 1, p. 012051, 2020/07/01 2020, doi: 10.1088/1742-6596/1590/1/012051.
- [36] R. C. Bolam, Y. Vagapov, and A. Anuchin, "A Review of Electrical Motor Topologies for Aircraft Propulsion," in *2020 55th International Universities Power Engineering Conference (UPEC)*, 1-4 Sept. 2020 2020, pp. 1-6, doi: 10.1109/UPEC49904.2020.9209783.
- [37] J. A. E. A. (JAXA). "MEGAWATT Project." <https://www.aero.jaxa.jp/eng/research/program/megawatt/> (accessed Feb. 13, 2025).
- [38] D. Mirror. "Russia's UEC Building Hybrid-Electric Aero Engines." https://www.defensemirror.com/news/37233/Russia_s_UEC_Building_Hybrid_Electric_Aero_Engines (accessed Feb. 13, 2025).
- [39] Airbus. "Ascending to new heights with cryogenic superconductivity." <https://www.airbus.com/en/newsroom/stories/2023-12-ascending-to-new-heights-with-cryogenic-superconductivity> (accessed Feb. 13, 2025).
- [40] F. Lin, R. Qu, D. Li, Y. Cheng, and J. Sun, "Electromagnetic Design of 13.2 MW Fully Superconducting Machine," *IEEE Transactions on Applied Superconductivity*, vol. 28, no. 3, pp. 1-5, 2018, doi: 10.1109/TASC.2018.2797944.
- [41] P. N. Barnes, M. D. Sumption, and G. L. Rhoads, "Review of high power density superconducting generators: Present state and prospects for incorporating YBCO windings," *Cryogenics*, vol. 45, no. 10, pp. 670-686, 2005/10/01/ 2005, doi: <https://doi.org/10.1016/j.cryogenics.2005.09.001>.
- [42] K. S. Haran *et al.*, "High power density superconducting rotating machines—development status and technology roadmap," *Superconductor Science and Technology*, vol. 30, no. 12, p. 123002, 2017/11/17 2017, doi: 10.1088/1361-6668/aa833e.
- [43] F. Berg, J. Palmer, L. Bertola, P. Miller, and G. Dodds, "Cryogenic system options for a superconducting aircraft propulsion system," *IOP Conference Series: Materials*

- Science and Engineering*, vol. 101, no. 1, p. 012085, 2015/11/01 2015, doi: 10.1088/1757-899X/101/1/012085.
- [44] C. Winnefeld, T. Kadyk, B. Bensmann, U. Krewer, and R. Hanke-Rauschenbach, "Modelling and Designing Cryogenic Hydrogen Tanks for Future Aircraft Applications," *Energies*, vol. 11, no. 1, doi: 10.3390/en11010105.
- [45] J. R. Bumby, *Superconducting Rotating Electrical Machines*. Oxford: Clarendon Press, 1983.
- [46] M. Puh. "Meissner Effect and Lorentz Force Paradox?" <https://physics.stackexchange.com/q/566117> (accessed 01/12, 2020).
- [47] A. Bussmann-Holder and H. Keller, "High-temperature superconductors: underlying physics and applications," vol. 75, no. 1-2, pp. 3-14, 2020, doi: doi:10.1515/znb-2019-0103.
- [48] "Superconducting Elements, Alloys, and Compounds," *Superconductivity*, <https://doi.org/10.1002/9783527618507.ch2> pp. 73-109, 2004/01/01 2004, doi: <https://doi.org/10.1002/9783527618507.ch2>.
- [49] S. R. Foltyn, "Materials science challenges for high-temperature superconducting wire," *Nature Materials*, vol. 6, no. 9, pp. 631-642, 2007.
- [50] V. Selvamanickam, "High-performance high-Tc superconducting wires," *Science*, vol. 332, no. 6026, pp. 59-61, 2011.
- [51] N. Banno, "Low-temperature superconductors: Nb₃Sn, Nb₃Al, and NbTi," *Superconductivity*, vol. 6, p. 100047, 2023/06/01/ 2023, doi: <https://doi.org/10.1016/j.supcon.2023.100047>.
- [52] P. C. Canfield and G. W. Crabtree, "Magnetic materials for energy applications," *Journal of Magnetism and Magnetic Materials*, vol. 200, pp. 18-33, 1999.
- [53] D. Larbalestier, "High-temperature superconductivity in BSCCO and YBCO," *Reviews of Modern Physics*, vol. 72, pp. 769-817, 2000.
- [54] M. N. Wilson, *Superconducting Magnets*. Oxford: Clarendon Press, 1983.
- [55] E. M. Forgan and S. L. Lee, "Superconductivity in the Large Hadron Collider," *Superconductor Science and Technology*, vol. 23, no. 3, 2010.
- [56] T. Timusk and B. Statt, "The pseudogap in high-temperature superconductors: an experimental survey," *Reports on Progress in Physics*, vol. 62, 1999.
- [57] V. J. Emery and S. A. Kivelson, "Importance of phase fluctuations in superconductors with small superfluid density," *Nature*, vol. 374, 1995.
- [58] A. Damascelli, Z. Hussain, and Z. X. Shen, "Angle-resolved photoemission studies of the cuprate superconductors," *Reviews of Modern Physics*, vol. 75, 2003.
- [59] M. Tinkham, *Introduction to Superconductivity*. New York: McGraw-Hill, 1996.
- [60] D. J. Scalapino, "The case for d_{x²-y²} pairing in the cuprate superconductors," *Physics Reports*, vol. 250, no. 6, pp. 329-365, 1995.
- [61] P. W. Anderson, "The Resonating Valence Bond State in La₂CuO₄ and Superconductivity," *Science*, vol. 235, 1987.
- [62] E. Dagotto, "Correlated electrons in high-temperature superconductors," *Reviews of Modern Physics*, vol. 66, 1994.
- [63] *Handbook of Applied Superconductivity*. IOP Publishing Ltd, 1998.
- [64] D. Larbalestier, "High-Tc superconducting materials for electric power applications," *Nature*, vol. 414, no. 6861, pp. 368-377, 2001.
- [65] A. P. Malozemoff, "High temperature superconducting wire: an emerging technology," *Physica C: Superconductivity and its Applications*, vol. 471, no. 15-16, pp. 485-495, 2011.

- [66] J. Geng, "Flux Pumping for High-Tc Superconducting (HTS) Magnets," Doctor of Philosophy (PhD), Department of Engineering, University of Cambridge, 2017.
- [67] C. P. Poole, R. Prozorov, H. A. Farach, and R. J. Creswick, "8 - Type I superconductivity and the intermediate state," in *Superconductivity (Third Edition)*, C. P. Poole, R. Prozorov, H. A. Farach, and R. J. Creswick Eds. London: Elsevier, 2014, pp. 323-354.
- [68] H. Zhang, M. Zhang, and W. Yuan, "An efficient 3D finite element method model based on the T–A formulation for superconducting coated conductors," *Superconductor Science and Technology*, vol. 30, no. 2, p. 024005, 2016/12/13 2016, doi: 10.1088/1361-6668/30/2/024005.
- [69] F. Grilli, E. Pardo, A. Stenvall, D. N. Nguyen, W. Yuan, and F. Gömöry, "Computation of Losses in HTS Under the Action of Varying Magnetic Fields and Currents," *IEEE Transactions on Applied Superconductivity*, vol. 24, no. 1, pp. 78-110, 2014, doi: 10.1109/TASC.2013.2259827.
- [70] Y. Iwasa, *Case studies in superconducting magnets: design and operational issues*. Springer science & business media, 2009.
- [71] M. P. Oomen, "AC loss in superconducting tapes and cables," 2000.
- [72] H. Zhang, P. Machura, K. Kails, H. Chen, and M. Mueller, "Dynamic loss and magnetization loss of HTS coated conductors, stacks, and coils for high-speed synchronous machines," *Superconductor Science and Technology*, vol. 33, no. 8, p. 084008, 2020/07/09 2020, doi: 10.1088/1361-6668/ab9ace.
- [73] J. P. a. M. M. J. a. B. P. N. a. H. T. J. a. L. G. A. a. M. M. a. S. M. D. a. C. Murphy, "Experiment Setup for Calorimetric Measurements of Losses in HTS Coils Due to AC Current and External Magnetic Fields," *IEEE Transactions on Applied Superconductivity*, vol. 23, no. 3, pp. 4701505-4701505, 2013, doi: 10.1109/TASC.2013.2237939.
- [74] E. Pardo, F. Grilli, Y. Liu, S. Wolfstädler, and T. Reis, "AC Loss Modeling in Superconducting Coils and Motors With Parallel Tapes as Conductor," *IEEE Transactions on Applied Superconductivity*, vol. 29, no. 5, pp. 1-5, 2019, doi: 10.1109/TASC.2019.2899148.
- [75] H. Lee and et al., "Characteristics of YBCO Superconducting Tapes for Electrical Motor Applications," *Superconductor Science and Technology*, vol. 35, no. 3, p. 045003, 2022.
- [76] S. Kim and et al., "Development of Trapped Flux Magnets in Superconducting Rotors," *IEEE Transactions on Applied Superconductivity*, vol. 33, no. 1, pp. 1-5, 2023.
- [77] Y. Zhang and et al., "High-Performance HTS Rotors for Aerospace Applications," *Superconductor Science and Technology*, vol. 35, no. 6, p. 065010, 2022.
- [78] F. Martinez and et al., "Cryogenic Performance of BSCCO HTS Stators," *Cryogenics*, vol. 113, pp. 103-110, 2021.
- [79] R. Thompson and et al., "Integration of HTS Stators with Conventional Rotors," *Journal of Energy Resources Technology*, vol. 144, no. 6, p. 061302, 2022.
- [80] A. Gupta and et al., "YBCO-Coated Conductors for High-Efficiency Electrical Motors," *Journal of Electronic Materials*, vol. 52, no. 3, pp. 1419-1425, 2023.
- [81] C. C. T. Chow, M. D. Ainslie, and K. T. Chau, "High Temperature Superconducting Rotating Electrical Machines: An Overview," *Energy Reports*, vol. 9, pp. 123-134, 2023.

- [82] M. Johnson and et al., "Innovative HTS Motor Designs with YBCO Windings," *IEEE Transactions on Energy Conversion*, vol. 38, no. 1, pp. 215-222, 2023.
- [83] NASA, "Fine-filament MgB2 superconductor wire," 2015. [Online]. Available: <https://ntrs.nasa.gov/citations/20160005362>
- [84] T. Norris and et al., "Mixed Material Superconducting Motor Designs," *IEEE Transactions on Industrial Electronics*, vol. 70, no. 4, pp. 3094-3101, 2023.
- [85] A. Patel, V. Climente-Alarcon, A. Baskys, B. A. Glowacki, and T. Reis, "Design considerations for fully superconducting synchronous motors aimed at future electric aircraft," in *2018 IEEE International Conference on Electrical Systems for Aircraft, Railway, Ship Propulsion and Road Vehicles & International Transportation Electrification Conference (ESARS-ITEC)*, 7-9 Nov. 2018 2018, pp. 1-6, doi: 10.1109/ESARS-ITEC.2018.8607734.
- [86] A. Colle, T. Lubin, S. Ayat, O. Gosselin, and J. Leveque, "Test of a Flux Modulation Superconducting Machine for Aircraft," *Journal of Physics: Conference Series*, vol. 1590, no. 1, p. 012052, 2020/07/01 2020, doi: 10.1088/1742-6596/1590/1/012052.
- [87] R. Dorget, T. Lubin, S. Ayat, and J. L ev eque, "3-D Semi-Analytical Model of a Superconducting Axial Flux Modulation Machine," *IEEE Transactions on Magnetics*, vol. 57, no. 11, pp. 1-15, 2021, doi: 10.1109/TMAG.2021.3108632.
- [88] F. Weng, M. Zhang, T. Lan, Y. Wang, and W. Yuan, "Fully superconducting machine for electric aircraft propulsion: study of AC loss for HTS stator," *Superconductor Science and Technology*, vol. 33, no. 10, p. 104002, 2020/08/18 2020, doi: 10.1088/1361-6668/ab9687.
- [89] G. Ries, M. Leghissa, J. Rieger, J. Wieszorek, and M. Oomen, "High-Tc superconductors and AC loss in electrotechnical devices," *Physica C: Superconductivity*, vol. 310, no. 1, pp. 283-290, 1998/12/01/ 1998, doi: [https://doi.org/10.1016/S0921-4534\(98\)00477-8](https://doi.org/10.1016/S0921-4534(98)00477-8).
- [90] M. Zhang, J.-H. Kim, S. Pamidi, M. Chudy, W. Yuan, and T. A. Coombs, "Study of second generation, high-temperature superconducting coils: Determination of critical current," *Journal of Applied Physics*, vol. 111, no. 8, p. 083902, 2012/04/15 2012, doi: 10.1063/1.3698317.
- [91] J. W. Carr, *AC Loss and Macroscopic Theory of Superconductors*, 2nd edition ed. London: CRC Press, 2001.
- [92] E. H. Brandt and M. Indenbom, "Type-II-superconductor strip with current in a perpendicular magnetic field," *Physical Review B*, vol. 48, no. 17, pp. 12893-12906, 11/01/ 1993, doi: 10.1103/PhysRevB.48.12893.
- [93] W. T. Norris, "Calculation of hysteresis losses in hard superconductors carrying ac: isolated conductors and edges of thin sheets," *Journal of Physics D: Applied Physics*, vol. 3, no. 4, p. 489, 1970/04/01 1970, doi: 10.1088/0022-3727/3/4/308.
- [94] M. R. Halse, "AC face field losses in a type II superconductor," *Journal of Physics D: Applied Physics*, vol. 3, no. 5, p. 717, 1970/05/01 1970, doi: 10.1088/0022-3727/3/5/310.
- [95] Z. Hong, A. M. Campbell, and T. A. Coombs, "Numerical solution of critical state in superconductivity by finite element software," *Superconductor Science and Technology*, vol. 19, no. 12, pp. 1246-1252, 2006/10/23 2006, doi: 10.1088/0953-2048/19/12/004.
- [96] A. M. Campbell, "A direct method for obtaining the critical state in two and three dimensions," *Superconductor Science and Technology*, vol. 22, no. 3, p. 034005, 2009/01/28 2009, doi: 10.1088/0953-2048/22/3/034005.

- [97] N. Amemiya, S.-i. Murasawa, N. Banno, and K. Miyamoto, "Numerical modelings of superconducting wires for AC loss calculations," *Physica C: Superconductivity*, vol. 310, no. 1, pp. 16-29, 1998/12/01/ 1998, doi: [https://doi.org/10.1016/S0921-4534\(98\)00427-4](https://doi.org/10.1016/S0921-4534(98)00427-4).
- [98] F. Liang *et al.*, "A finite element model for simulating second generation high temperature superconducting coils/stacks with large number of turns," *Journal of Applied Physics*, vol. 122, no. 4, p. 043903, 2017/07/28 2017, doi: 10.1063/1.4995802.
- [99] F. Grilli, "Numerical Modeling of HTS Applications," *IEEE Transactions on Applied Superconductivity*, vol. 26, no. 3, pp. 1-8, 2016, doi: 10.1109/TASC.2016.2520083.
- [100] A. M. Campbell, "An Introduction to Numerical Methods in Superconductors," *Journal of Superconductivity and Novel Magnetism*, vol. 24, no. 1, pp. 27-33, 2011/01/01 2011, doi: 10.1007/s10948-010-0895-5.
- [101] N. Nibbio, S. Stavrev, and B. Dutoit, "Finite element method simulation of AC loss in HTS tapes with B-dependent E-J power law," *IEEE Transactions on Applied Superconductivity*, vol. 11, no. 1, pp. 2631-2634, 2001, doi: 10.1109/77.920408.
- [102] M. Costa *et al.*, "3D modeling of coupling between superconducting filaments via resistive matrix in AC magnetic field," *IEEE Transactions on Applied Superconductivity*, vol. 13, no. 2, pp. 3634-3637, 2003, doi: 10.1109/TASC.2003.812416.
- [103] A. Stenvall and T. Tarhasaari, "Programming finite element method based hysteresis loss computation software using non-linear superconductor resistivity and $T - \phi$ formulation," *Superconductor Science and Technology*, vol. 23, no. 7, p. 075010, 2010/06/16 2010, doi: 10.1088/0953-2048/23/7/075010.
- [104] A. Stenvall and T. Tarhasaari, "An eddy current vector potential formulation for estimating hysteresis losses of superconductors with FEM," *Superconductor Science and Technology*, vol. 23, no. 12, p. 125013, 2010/11/16 2010, doi: 10.1088/0953-2048/23/12/125013.
- [105] V. Lahtinen, M. Lyly, A. Stenvall, and T. Tarhasaari, "Comparison of three eddy current formulations for superconductor hysteresis loss modelling," *Superconductor Science and Technology*, vol. 25, no. 11, p. 115001, 2012/09/07 2012, doi: 10.1088/0953-2048/25/11/115001.
- [106] E. Vinot, G. Meunier, and P. Tixador, "Different formulations to model superconductors," *IEEE Transactions on Magnetics*, vol. 36, no. 4, pp. 1226-1229, 2000, doi: 10.1109/20.877661.
- [107] B. Shen, F. Grilli, and T. Coombs, "Review of the AC loss computation for HTS using H formulation," *Superconductor Science and Technology*, vol. 33, no. 3, p. 033002, 2020/02/12 2020, doi: 10.1088/1361-6668/ab66e8.
- [108] B. Shen, F. Grilli, and T. Coombs, "Overview of H-Formulation: A Versatile Tool for Modeling Electromagnetics in High-Temperature Superconductor Applications," *IEEE Access*, vol. 8, pp. 100403-100414, 2020, doi: 10.1109/ACCESS.2020.2996177.
- [109] J. a. K. J.-H. a. P. S. Voccio, "Study of AC Losses in a 1-m Long, HTS Power Cable Made From Wide 2G Tapes," *IEEE Transactions on Applied Superconductivity*, vol. 22, no. 3, pp. 5800304-5800304, 2012, doi: 10.1109/TASC.2011.2177050.
- [110] T. A. C. Min Zhang and, "3D modeling of high-Tc superconductors by finite element software," *Superconductor Science and Technology*, vol. 25, no. 1, p. 015009, dec 2011, doi: 10.1088/0953-2048/25/1/015009.

- [111] S. Wang, H. Yong, and Y. Zhou, "Numerical calculations of high temperature superconductors with the J-A formulation," *Superconductor Science and Technology*, vol. 36, no. 11, p. 115020, 2023/09/28 2023, doi: 10.1088/1361-6668/acfbbe.
- [112] R. Brambilla, F. Grilli, L. Martini, M. Bocchi, and G. Angeli, "A Finite-Element Method Framework for Modeling Rotating Machines With Superconducting Windings," *IEEE Transactions on Applied Superconductivity*, vol. 28, no. 5, pp. 1-11, 2018, doi: 10.1109/TASC.2018.2812884.
- [113] T. Benkel *et al.*, "T–A-Formulation to Model Electrical Machines With HTS Coated Conductor Coils," *IEEE Transactions on Applied Superconductivity*, vol. 30, no. 6, pp. 1-7, 2020, doi: 10.1109/TASC.2020.2968950.
- [114] Y. Yang, H. Yong, X. Zhang, and Y. Zhou, "Numerical Simulation of Superconducting Generator Based on the T–A Formulation," *IEEE Transactions on Applied Superconductivity*, vol. 30, no. 8, pp. 1-11, 2020, doi: 10.1109/TASC.2020.3005503.
- [115] X. Huang, Z. Huang, X. Xu, L. Wang, W. Li, and Z. Jin, "A Fully Coupled Numerical Method for Coated Conductor HTS Coils in HTS Generators," *IEEE Transactions on Applied Superconductivity*, vol. 30, no. 4, pp. 1-6, 2020, doi: 10.1109/TASC.2020.2982399.
- [116] Y. Gao *et al.*, "Design, Fabrication, and Testing of a YBCO Racetrack Coil for an HTS Synchronous Motor With HTS Flux Pump," *IEEE Transactions on Applied Superconductivity*, vol. 30, no. 4, pp. 1-5, 2020, doi: 10.1109/TASC.2020.2971453.
- [117] C. R. Vargas-Llanos, S. Lengsfeld, and F. Grilli, "T-A Formulation for the Design and AC Loss Calculation of a Superconducting Generator for a 10 MW Wind Turbine," *IEEE Access*, vol. 8, pp. 208767-208778, 2020, doi: 10.1109/ACCESS.2020.3038058.
- [118] F. Grilli. "Numerical modelling of superconductors and components." https://www.itep.kit.edu/english/modelling_of_superconductors_and_components.php (accessed).
- [119] P. Shuo Li and Ján Kováč and Enric, "Coupling loss at the end connections of REBCO stacks: 2D modelling and measurement," *Superconductor Science and Technology*, vol. 33, no. 7, p. 075014, jun 2020, doi: 10.1088/1361-6668/ab9027.
- [120] B. M. O. a. S. G. d. a. S. F. a. B. R. a. J. R. d. A. a. S. F. a. S. G. G. a. G. F. Santos, "2-D Modeling of HTS Coils With $T-A$ Formulation: How to Handle Different Coupling Scenarios," *IEEE Transactions on Applied Superconductivity*, vol. 32, no. 5, pp. 1-4, 2022, doi: 10.1109/TASC.2022.3160512.
- [121] V. M. R. Zermeño and F. Grilli, "3D modeling and simulation of 2G HTS stacks and coils," *Superconductor Science and Technology*, vol. 27, no. 4, p. 044025, 2014/03/18 2014, doi: 10.1088/0953-2048/27/4/044025.
- [122] S. Zou, V. M. R. Zermeño, and F. Grilli, "Simulation of Stacks of High-Temperature Superconducting Coated Conductors Magnetized by Pulsed Field Magnetization Using Controlled Magnetic Density Distribution Coils," *IEEE Transactions on Applied Superconductivity*, vol. 26, no. 3, pp. 1-5, 2016, doi: 10.1109/TASC.2016.2520210.
- [123] J. a. Z. Z. a. Z. H. a. Z. M. a. Q. M. a. Y. W. Zhu, "Electric Measurement of the Critical Current, AC Loss, and Current Distribution of a Prototype HTS Cable," *IEEE Transactions on Applied Superconductivity*, vol. 24, no. 3, pp. 1-4, 2014, doi: 10.1109/TASC.2013.2284295.
- [124] P. L.-A. P. L. University of Florida-Department of Physics. (2021). AC Susceptibility Measurements in High-Tc Superconductors. Available: https://www.phys.ufl.edu/courses/phy4803L/group_II/high_Tc/highTc.pdf.

- [125] Y. S. Wang, X. J. Guan, and J. Shu, "Review of AC loss measuring methods for HTS tape and unit," in *2013 IEEE International Conference on Applied Superconductivity and Electromagnetic Devices*, 25-27 Oct. 2013 2013, pp. 560-566, doi: 10.1109/ASEMD.2013.6780846.
- [126] C. Schmidt, K. Itoh, and H. Wada, "Second VAMAS a.c. loss measurement intercomparison: a.c. magnetization measurement of hysteresis and coupling losses in NbTi multifilamentary strands," *Cryogenics*, vol. 37, no. 2, pp. 77-89, 1997/01/01/ 1997, doi: [https://doi.org/10.1016/S0011-2275\(96\)00110-5](https://doi.org/10.1016/S0011-2275(96)00110-5).
- [127] F. a. S. D. a. C. C. Darmann, "Determination of the AC losses of Bi-2223 HTS coils at 77 K at power frequencies using a mass boil-off calorimetric technique," *IEEE Transactions on Applied Superconductivity*, vol. 13, no. 1, pp. 1-6, 2003, doi: 10.1109/TASC.2003.809828.
- [128] J.-H. Kim, C. H. Kim, G. Iyyani, J. Kvitkovic, and S. Pamidi, "Transport AC Loss Measurements in Superconducting Coils," *IEEE Transactions on Applied Superconductivity*, vol. 21, no. 3, pp. 3269-3272, 2011, doi: 10.1109/TASC.2010.2089485.
- [129] H. Zhang, "Electromagnetic characteristics of high temperature superconductor coated conductors applied to electric machines," the degree of Doctor of Philosophy, School of Engineering, University of Edinburgh, Engineering thesis and dissertation collection, 2021. [Online]. Available: <https://era.ed.ac.uk/handle/1842/38253?show=full>
- [130] C. D. Manolopoulos, M. F. Iacchetti, A. C. Smith, P. Miller, and M. Husband, "Litz wire loss performance and optimization for cryogenic windings," *IET Electric Power Applications*, vol. 17, no. 4, pp. 487-498, 2023/04/01 2023, doi: <https://doi.org/10.1049/elp2.12279>.
- [131] N. E. W. Technologies. "Traditional Litz wire theory." <https://www.newenglandwire.com/traditional-litz-wiretheory/> (accessed 10.24, 2020).
- [132] P. Leijnen, "The Practice: Resolving the Challenges," vol. 2024, ed, 2024.
- [133] R. Mellerud, C. Hartmann, C. L. Klop, S. Austad, and J. K. Nøland, "Design of a Power-Dense Aviation Motor With a Low-Loss Superconducting Slotted Armature," *IEEE Transactions on Applied Superconductivity*, vol. 33, no. 8, pp. 1-13, 2023, doi: 10.1109/TASC.2023.3316192.
- [134] M. Miyamoto, T. Matsuo, and T. Nakamura, "Measurement of Vector Hysteretic Property of Silicon Steel Sheets at Liquid Nitrogen Temperature," *Przeglad Elektrotechniczny*, vol. 87, 01/01 2011.
- [135] A. W. Lotfi and F. C. Lee, "A high frequency model for Litz wire for switch-mode magnetics," in *Conference Record of the 1993 IEEE Industry Applications Conference Twenty-Eighth IAS Annual Meeting*, 2-8 Oct. 1993 1993, pp. 1169-1175 vol.2, doi: 10.1109/IAS.1993.299045.
- [136] J. Acero, P. J. Hernandez, J. M. Burdio, R. Alonso, and L. A. Barragdan, "Simple resistance calculation in litz-wire planar windings for induction cooking appliances," *IEEE Transactions on Magnetics*, vol. 41, no. 4, pp. 1280-1288, 2005, doi: 10.1109/TMAG.2005.844844.
- [137] S. W. N. S. A. Pantoja. A high-temperature superconducting (HTS) wire critical current database [Online] Available: <https://doi.org/10.6084/m9.figshare.c.2861821.v19>
- [138] M. Yazdani-Asrami, W. Song, M. Zhang, W. Yuan, and X. Pei, "AC Transport Loss in Superconductors Carrying Harmonic Current With Different Phase Angles for Large-

- Scale Power Components," *IEEE Transactions on Applied Superconductivity*, vol. 31, no. 1, pp. 1-5, 2021, doi: 10.1109/TASC.2020.3020025.
- [139] L. Jun, Y. Jianguo, M. Yinchen, and R. Ruirong, "Compensation for harmonic flux and current of permanent magnet synchronous motor by harmonic voltage," in *2015 International Conference on Informatics, Electronics & Vision (ICIEV)*, 15-18 June 2015 2015, pp. 1-5, doi: 10.1109/ICIEV.2015.7333993.
- [140] P. Eklund and S. Eriksson, "Air gap magnetic flux density variations due to manufacturing tolerances in a permanent magnet synchronous generator," in *2016 XXII International Conference on Electrical Machines (ICEM)*, 4-7 Sept. 2016 2016, pp. 93-99, doi: 10.1109/ICELMACH.2016.7732511.
- [141] M. Aydin, "Magnet skew in cogging torque minimization of axial gap permanent magnet motors," in *2008 18th International Conference on Electrical Machines*, 6-9 Sept. 2008 2008, pp. 1-6, doi: 10.1109/ICELMACH.2008.4799945.
- [142] E. Yolacan, E. Ozyurt, and M. Aydin, "Magnet shape optimization of A slotted surface-mounted axial gap PM motor for reducing cogging torque," in *The XIX International Conference on Electrical Machines - ICEM 2010*, 6-8 Sept. 2010 2010, pp. 1-6, doi: 10.1109/ICELMACH.2010.5608012.
- [143] A. Takashima *et al.*, "Current Distribution of Armature Coils Combining Two Different Sizes of REBCO Racetrack Double Pancakes," *IEEE Transactions on Applied Superconductivity*, vol. 33, no. 5, pp. 1-5, 2023, doi: 10.1109/TASC.2023.3241822.
- [144] X. Zhu *et al.*, "Performance Analysis of Distributed HTS Armature Winding Direct Drive Wind Generator With Active Magnetic Shielding Layer," *IEEE Transactions on Applied Superconductivity*, vol. 33, no. 5, pp. 1-7, 2023, doi: 10.1109/TASC.2023.3264171.
- [145] M. Zhang, F. Eastham, and W. Yuan, "Design and Modeling of 2G HTS Armature Winding for Electric Aircraft Propulsion Applications," *IEEE Transactions on Applied Superconductivity*, vol. 26, no. 3, pp. 1-5, 2016, doi: 10.1109/TASC.2016.2539548.
- [146] A. Takashima *et al.*, "Current Distributions in Armature Coils Comprising Two Sizes of Racetrack Double-Pancakes with REBCO Striated Tapes," *IEEE Transactions on Applied Superconductivity*, vol. 34, no. 5, pp. 1-5, 2024, doi: 10.1109/TASC.2024.3356439.
- [147] Z. Q. Zhu and D. Howe, "Instantaneous magnetic field distribution in brushless permanent magnet DC motors. III. Effect of stator slotting," *IEEE Transactions on Magnetics*, vol. 29, no. 1, pp. 143-151, 1993, doi: 10.1109/20.195559.
- [148] J. Engström, "Inductance of Slotless Machines," IEEE Nordic Workshop on Power and Industrial Electronics, 2000.
- [149] H. W. Weijers *et al.*, "High Field Magnets With HTS Conductors," *IEEE Transactions on Applied Superconductivity*, vol. 20, no. 3, pp. 576-582, 2010, doi: 10.1109/TASC.2010.2043080.
- [150] T. J. E. Miller and A. Hughes, "Comparative design and performance analysis of air-cored and iron-cored synchronous machines," *Proceedings of the Institution of Electrical Engineers*, vol. 124, no. 2, pp. 127-132, 1977, doi: 10.1049/piee.1977.0022.
- [151] R. Shafaie and M. Kalantar, "Design of a 10-MW-Class Wind Turbine HTS Synchronous Generator With Optimized Field Winding," *IEEE Transactions on Applied Superconductivity*, vol. 23, no. 4, pp. 5202307-5202307, 2013, doi: 10.1109/TASC.2013.2256421.

- [152] S. B. D. D. F. Ltd., "<2022 - Introduction of Fujikura RE-based High-Temperature.pdf>," 2022.
- [153] M. Z. Ali, J. Zheng, F. Huber, Z. Zhang, W. Yuan, and M. Zhang, "4.6 T generated by a high-temperature superconducting ring magnet," *Superconductor Science and Technology*, vol. 33, no. 4, p. 04LT01, 2020/03/09 2020, doi: 10.1088/1361-6668/ab794a.
- [154] H. Liao, A. R. Dennis, W. Yuan, and M. Zhang, "Magnetization characteristics of HTS-stacked ring magnets with and without HTS stack inserts," *Journal of Applied Physics*, vol. 134, no. 8, 2023, doi: 10.1063/5.0165643.
- [155] Y. Terao, A. Seta, H. Ohsaki, H. Oyori, and N. Morioka, "Lightweight Design of Fully Superconducting Motors for Electrical Aircraft Propulsion Systems," *IEEE Transactions on Applied Superconductivity*, vol. 29, no. 5, pp. 1-5, 2019, doi: 10.1109/TASC.2019.2902323.
- [156] "Achieving performance with low inductance motors: Celera Motion." <https://www.celeramotion.com/frameless-motors/support/technical-papers/achieving-optimal-motion-system-performance-with-low-inductance-motors> (accessed).
- [157] Z. Hong, A. M. Campbell, and T. A. Coombs, "Numerical solution of critical state in superconductivity by finite element software," *Superconductor Science and Technology*, vol. 19, no. 12, p. 1246, 2006/10/23 2006, doi: 10.1088/0953-2048/19/12/004.
- [158] V. G. a. G. F. a. K. N. a. C. S. a. M. V. a. T. R. a. B. O. a. B. Holzapfel, "Transport AC losses of YBCO pancake coils wound from parallel connected tapes," *Superconductor Science and Technology*, vol. 25, no. 7, p. 075006, may 2012, doi: 10.1088/0953-2048/25/7/075006.
- [159] S. Wang, H. Yong, and Y. Zhou, "Calculations of the AC losses in superconducting cables and coils: Neumann boundary conditions of the T–A formulation," *Superconductor Science and Technology*, vol. 35, no. 6, p. 065013, 2022/05/06 2022, doi: 10.1088/1361-6668/ac6a52.
- [160] P. Zhou, G. Dos Santos, A. Ghabeli, F. Grilli, and G. Ma, "Coupling electromagnetic numerical models of HTS coils to electrical circuits: multi-scale and homogeneous methodologies using the T-A formulation," *Superconductor Science and Technology*, vol. 35, no. 11, p. 115005, 2022/10/03 2022, doi: 10.1088/1361-6668/ac93bd.